GRAPHITE SURFACE EROSION BY ION IRRADIATION AND RELEASING BEHAVIOR OF DEUTERIUM AND HELIUM FROM GRAPHITE

1988

HISAO ATSUMI

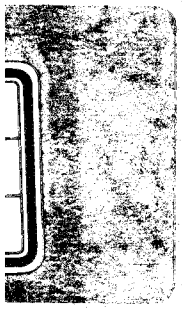

GRAPHITE SURFACE EROSION BY ION IRRADIATION AND RELEASING BEHAVIOR OF DEUTERIUM AND HELIUM FROM GRAPHITE

（グラファイトのイオン照射による表面損傷及び重水素・ヘリウム放出挙動に関する研究）

1988

HISAO ATSUMI

CONTENTS

I General Introduction

The recent advance of the study on thermonuclear fusion presents the large scale facilities of fusion experimental reactor (TFTR, JET, JT-60, T-15, Doublet-III , etc.) and the inevitably severe conditions for materials. Especially, first walls facing the plasma is often subjected to various types of surface damage and surface erosion through the plasma-wall interaction (PWI) processes. In the early days the common choice of first walls was refractory metals since these materials were durable to high temperature operation. On the occasion of the PWI, impurity atoms for the plasma are emitted from the wall into the plasma and reduce the plasma temperature due to electromagnetic radiation losses. The radiation loss from a plasma, mainly by Bremsstrahlung, is proportionally increased with Z^2, where Z is the atomic number of the impurity ions in a plasma. Extensive efforts have been made in recent years to improve the data base for materials selection [1-14]. In this area, it is now recognized that the low atomic number ceramic materials (graphite, carbides, carbon related materials, etc.) should be suitable for first walls including limiters in a fusion reactor.

The main criteria for selecting first wall materials in fusion reactors are given in Table 1-1 [1,4,10,12]. The peculiar demands for fusion materials are the durability against the high wall loading by energetic particles (n^0, e^-, D^+, T^+, He^+, etc.) and a high heat flux. First walls must maintain the structural integrity under such severe environment for a long period during the fusion reactor operation. Several candidate materials for first walls are listed with their fundamental properties in Table 1-2 [17-22]. In these materials, especially, graphite is considered as the most highly suitable candidate and employed as the limiters in JET,

Table 1-1 Main criteria for selecting first wall materials in fusion reactors.

ref. [1,4,10,12]

1.Mechanical Properties		5.Impurity Control	
• Yield strength	High	• Atomic number	Low
• Fracture toughness	High	• Melting point	High
• Creep strength	High	• Vapor pressure	Low
• Density	Mid or Low	• Sputtering yield(physical,chemical)	Low
2.Thermal Properties		• Blistering	Low
• Melting point	High	• Flaking	Low
• Thermal conductivity	High	6.Hydrogen Recycling, Vacuum Properties	
• Thermal shock resistivity	High	• Diffusion coefficient (D_2, T_2)	Low
• Thermal fatigue durability	High	• Solubility (D_2, T_2)	Low
• Thermal expansion	Low	• Permeability (D_2, T_2)	Low
3.Electric Properties		• Outgassing rate	Low
• Electrical conductivity	Mid or Low	7.Induced Radioactivity	
4.Radiation Damage		• Absorption cross section	Low
• Swelling	Low	8.Compatibility with D_2, T_2 and Coolants	
• Radiation induced creep	Low	9.Fabricability and Joining	
• Crack growth (Fatigue)	Low	10.Cost and Resource Availability	
• Embrittlement	Low	11.Industrial Capability and Data Base	

Table 1-2 Candidate materials for first walls (limiters, armors) and their fundamental properties.

ref. [17-22]

	Z(eff)	Melting Point (℃)	Density (g/cm³)	Elect. Conduct. (μΩ cm)	Specific Heat (cal/g℃)	Thermal Conduct. (W/m℃)	Tensile Strength (kgf/mm²)	Young's Modulus (kgf/mm²)	Thermal Expans. (× 10^{-6}/℃)	Thermal Shock Res.* (W/cm)
B_4C	5.2	2350	2.52	4.5× 10^{11}	0.23	27.6	30	46000	6.0	30
C(iso)	6	3600	1.5-2.0	900-4000	0.17	50-180	2.5-7	900-1500	2-8	100-7000
C(C-C)	6	3600	1.6-1.9	400-2000	0.17	100-400	10-100	4500-20000	1-6	100-80000
BN	6.1	3000	2.25	10^{11}	0.19	29	5-11	8000	7.7-75	3-50
BeO	6.3	2530	3.03	4× 10^{14}	0.24	220	21	32000	8.9	160
SiC	9.5	2700	3.22	107	0.16	40	35	48000	4.0	73
Al_2O_3	10.3	2054	3.9	1× 10^{22}	0.19	30	25	37000	8.1	25
Si_3N_4	10.6	1900	3.2	>10^{20}	0.18	11	11	8000-31000	3.1	15-40
TiC	10.8	3157	4.25	180	0.13	25	18	32000	7.4	19
Be	4	1280	1.848	4.0	0.38	200	42	30000	15	190
V	23	1890	6.11	25	0.12	31.5	19	13000-14000	7.8	55-59
SUS 316L	26.4	1371-1399	7.90	73	0.11	16	49	20300	16.0	24
Inconel 600	27.3	1354-1413	8.51	98.1	0.11	12.6	63	21800	13.3	27
Ni	28	1450	8.902	6.84	0.11	90.5	32.2	21000	12.5	110
Cu	29	1083	8.96	1.67	0.092	398	21.7	11900	16.8	430
Mo	42	2620	10.22	5.2	0.059	138	49	34800	5.1	380
W	74	3400	19.3	5.65	0.031	178	60	39600	4.5	600

* Thermal Shock Resistivity = $\frac{\text{Thermal Conductivity} \times \text{Tensile Strength}}{\text{Thermal Expansion} \times \text{Young's Modulus}}$

TFTR and Doublet III, because of its low-Z atomic number, low induced radioactivity, high sublimation or melting point, high thermal shock resistivity, etc. Lomer [15] has reported that graphite limiters, which are employed in JET, perform excellently with regard to durability against the macroscopic surface damage. Noda et al. [16] have reported that the graphite limiters employed in JIPP T-II U resulted in an improvement of the plasma parameters ; e.g. radiation losses mainly caused by metal impurities, loop voltage, electron density and electron temperature, as compared with those values obtained with stainless steel limiters. For this reason, graphite is widely used as the first wall material at present. In Table 1-2, C-C composite materials have excellent mechanical and thermal properties, however some problems concerning the fabrication technique and the cost of production are still unsettled.

Graphite has a tendency to interact easily with hydrogen isotopes. Accordingly, it may cause trouble of increasing a tritium inventory and producing volatile hydrocarbon species. From this point of view, several studies have dealt with the interactions (e.g. surface erosion, chemical sputtering and thermal desorption of hydrogen) between graphite and irradiated ions of hydrogen isotopes. However, there are various types of graphite and carbon such as isotropic graphite and anisotropic graphite, pyrolytic graphite and glassy carbon, classified by the structure, raw materials and means of production. For this reason, the surface erosion caused by D_2^+ ion irradiation and thermal desorption of hydrogen isotopes may be different among the types of graphite.

The first walls will be also bombarded by helium ions which are emitted from a plasma at the D-T fusion reaction or the discharge cleaning (e.g. super-shot in TFTR [23,24]). In the case of graphite, the sputtering yield for helium is approximately five times as much as that for deuterium at the

same energy [25], hence the surface damage will be heavier for helium ion irradiation. Furthermore, few studies have been performed on the thermal desorption behavior of helium from graphite implanted with He^+ ions, as compared with those of hydrogen isotopes. For the above reasons, it is important to study the surface erosion and thermal desorption of implanted helium in various types of graphite with attention to their structure.

In Chapter Ⅱ, as the preliminary analysis, fundamental properties of four graphite samples studied in this thesis are described. Some scanning electron micrographs and polarization photographs are shown and crystallographic characters (degree of crystallinity, size of crystallite and orientation of each grain) are given in this chapter.

In Chapter Ⅲ, the surface erosion of different types of graphite by 20 keV D_2^+ ion irradiation has been studied with attention to the change in surface features as the result of irradiation. In Chapter Ⅳ, the surface erosion and surface deformation have been studied on various types of graphite irradiated with 20 keV He^+ ions. Concerning the He^+ ion irradiation, the correlation of sputtering erosion and surface volume expansion has been discussed.

In Chapter Ⅴ, thermal desorption measurements of deuterium and deutero-methane have been made on graphite irradiated by D_2^+ ions. Similarly, thermal desorption behavior of helium from graphite and releasing mechanism have been described in Chapter Ⅵ.

Recently, extensive studies have been performed on the interaction between energetic particles and first walls. Only a little information on the static interaction (hydrogen uptake on graphite, hydrogen permeation and diffusion in graphite, etc.) is available, although these data are important to estimate the hydrogen recycling and tritium inventory in graphite. In Chapter Ⅶ, therefore, thermal desorption measurements have

been made on graphite exposed thermally to deuterium gas atmosphere at elevated temperatures. The solubility and diffusivity of deuterium in graphite were determined.

The conclusions of this thesis are summarized in Chapter Ⅶ.

References

[1] L.H.Lovner and G.R.Hopkins, Nucl.Technol. 29 (1976) 274.

[2] R.F.Bourque, in: "Proc. 2nd Topical Meeting on the Technology of Controlled Nuclear Fusion, Vol.Ⅳ", Richland, 1976, p.1525.

[3] Y.Gomay, S.Nomura, K.Fukuda, S.Muraoka and H.Nakamura, JAERI-M 6432 (1976) (in Japanese).

[4] R.W.Conn, J.Nucl.Mater. 76/77 (1978) 103.

[5] H.I.Avci, Y.Gohar, T.Y.Sung, G.L.Kulcinski and C.W.Maynard, Nucl.Eng.Design 45 (1978) 285.

[6] D.L.Smith and J.A.Krazinski, Trans.ANS 30 (1978) 65.

[7] R.A.Matheny, J.C.Corelli and G.G.Trantina, Trans.ANS 30 (1978) 161.

[8] M.Ulrickson, J.Nucl.Mater. 85/86 (1979) 231.

[9] Y.Gomay, S.Konoshima, N.Fujisawa, S.Kasai, M.Maeno, N.Suzuki, T.Hirayama and M.Shimada, Jpn.J.Appl.Phys. 18 (1979) 1317.

[10] M.Ulrickson, J.Vac.Sci.Technol. 18 (1981) 1037.

[11] G.P.Yu and J.E.Meyer, Trans.ANS 39 (1981) 259.

[12] T.Shikama and M.Okada, Bull.Jpn.Inst.Metals 23 (1984) 1014 (in Japanese).

[13] W.B.Gauster, J.A.Koski and R.D.Watson, J.Vac.Sci.Technol. A2 (1984) 634.

[14] Y.Gotoh, H.Hoven, K.Koizlik, J.Linke, U.Samm, B.Thiele and E.Wallura, J.Nucl.Mater. 133/134 (1985) 257.

[15] W.M.Lomer, J.Nucl.Mater. 133/134 (1985) 18.

[16] N.Noda, T.Watari, K.Toi, E.Kako, K.Sato, K.Ohkubo, K.Kawahata, I.Ogawa, T.Tetsuka, S.Tanahashi, S.Hirokura, Y.Taniguchi, Y.Kawasumi, R.Ando and J.Fujita, J.Nucl.Mater. 128/129 (1984) 304.

[17] Chemical Society of Japan ed., "Kagaku Binran Kisohen" (Maruzen, Tokyo, 1984) (in Japanese).

[18] S.Hatano ed., "Kougyo Zairyo Binran" (Nikkan Kogyo Shinbun, Tokyo, 1981) (in Japanese).

[19] M.Hasegawa ed., "Stainless-Kou Binran" (Nikkan Kogyo Shinbun, Tokyo, 1973) (in Japanese).

[20] Tanso Zairyo Gakkai ed., "Tansozairyo Nyuumon" (Tanso Zairyo Gakkai, Tokyo, 1984) (in Japanese).

[21] K.Hamano ed., "Fine Ceramics Handbook" (Asakura Shoten, Tokyo, 1984) (in Japanese).

[22] T.Oku, IPPJ-AM-50 (1987) 229.

[23] K.L.Wilson, IPPJ-AM-50 (1987) 238.

[24] M.A.Ulrickson, IPPJ-AM-50 (1987) 475.

[25] J.Bohdansky, H.L.Bay and W.Ottenberger, J.Nucl.Mater. 76/77 (1978) 163.

Ⅱ Characterization of Graphite Samples

1. Introduction

Graphite is the appropriate candidate for the first walls in a fusion reactor as mentioned in Chapter Ⅰ. There are many types of graphite having various microstructure (e.g. grain size and degree of graphitization) and properties (e.g. thermal conductivity, mechanical strength and ash content). Samples used in this study were two types of isotropic graphite (ISOGRAPH-88, Toyo Tanso Co.Ltd., and POCO DFP-3-2, POCO Graphite Co.Ltd.), graphitized paper (PAPYEX, Le Carbone Lorraine Co.Ltd.) and glassy carbon (GC-30, Tokai Carbon Co.Ltd.). Their fundamental properties are listed in Table 1. In this chapter, prior to the study on the graphite surface erosion and thermal desorption behavior, crystallographic characters and

Table 2-1 Fundamental properties of graphite samples (data presented from manufacturer).

	ISOGRAPH-88	POCO DFP-3-2	PAPYEX	GC-30
Density (g/cm³)	1.90	1.84	1.10	1.43 - 1.45
Specific heat (cal/g·℃)	0.17	-	-	-
Thermal conductivity (W/m·℃)	85	-	//a 160 //c 4.0	15 - 17
Thermal expansion ($\times 10^{-6}$/℃)	6.5	-	//a ~ 0 //c 25 - 28	2.0 - 2.2
Electrical resistivity ($\mu\Omega$·cm)	1500	1780	//a 1000 //c 50000	3500 - 4000
Young's modulus (kg/mm²)	1300	-	-	2200 - 2500
Tensile strength (kg/mm²)	7.0	-	//a 0.66	-
Flexural strength (kg/mm²)	9.5	8.4	-	5.0 - 6.0
Charpy impact value (kg·cm/cm²)	6.5	-	-	2.1 - 2.6
Shore hardness	90	-	//a 25	70 - 80
Thermal shock resistivity (W/cm)	703	-	-	-
Ash content (ppm)	1000	5	1000	1000
Grain diameter (μm)	mean 5	max 25	-	-
Pore diameter (μm)	mean 0.4	max 1	-	-
Porosity (%)	11 - 12	-	-	3 - 5

surface features of four samples have been studied.

2. Crystallographic characters of graphite samples

Surface deformation and roughening under ion irradiation are usually caused by the following processes.

i) blistering and flaking

ii) void swelling

iii) amorphization

iv) crystal growth

v) preferential sputtering

These processes should be affected by the individual properties of graphite samples, therefore, the information especially on crystallographic characters is needed to study the surface deformation process under ion irradiation. Figure 2-1 shows the typical graphite structure [1]. Artificial graphite materials such as graphite samples used in the present study are composed of fine grains which consist of the graphite structure on a microscopic scale. Isotropic graphite can be usually divided into two categories. One is the polycrystalline graphite composed of nearly

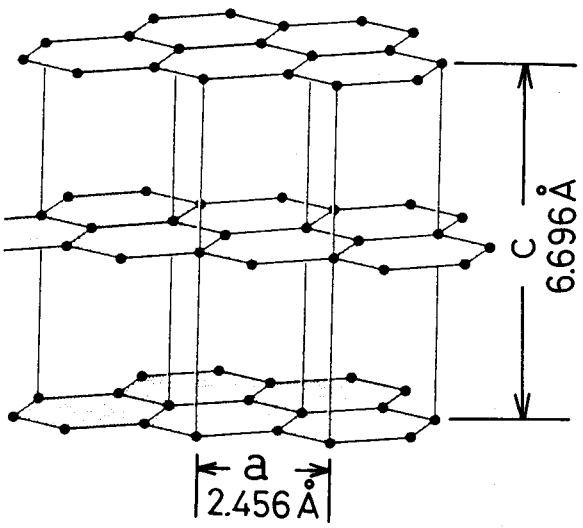

Fig. 2-1 Graphite structure [1].

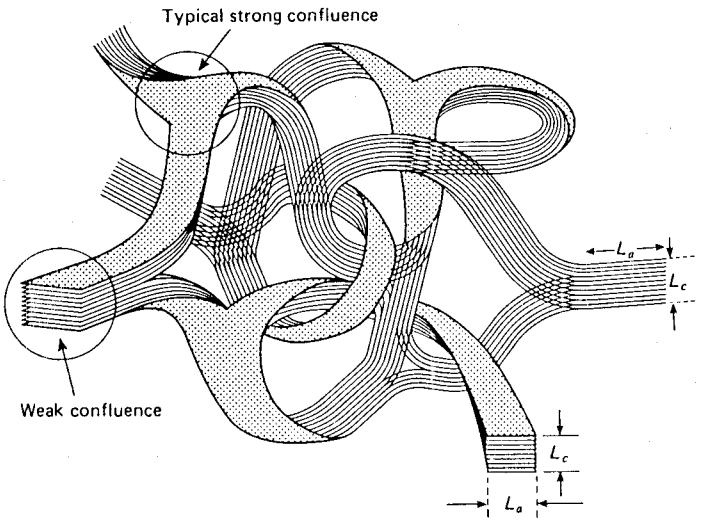

Fig. 2-2 Schematic structural model for a glassy carbon [2].

isotropic grains, and the other is composed of strongly anisotropic grains. Namely, this means that the completely isotropic graphite can be manufactured from the anisotropic grains, if the each shape of the grain is sphere and the grains are molded in keeping the random orientation. It may be impossible to distinguish the difference in structure only by the X-ray diffraction analysis on bulk graphite samples. POCO DFP-3-2 may correspond to the former, and ISOGRAPH-88 may correspond to the later as discussed below.

PAPYEX consists of stacks of graphite lamella whose thickness is approximately 0.1 μm estimated by scanning electron microscope (SEM)

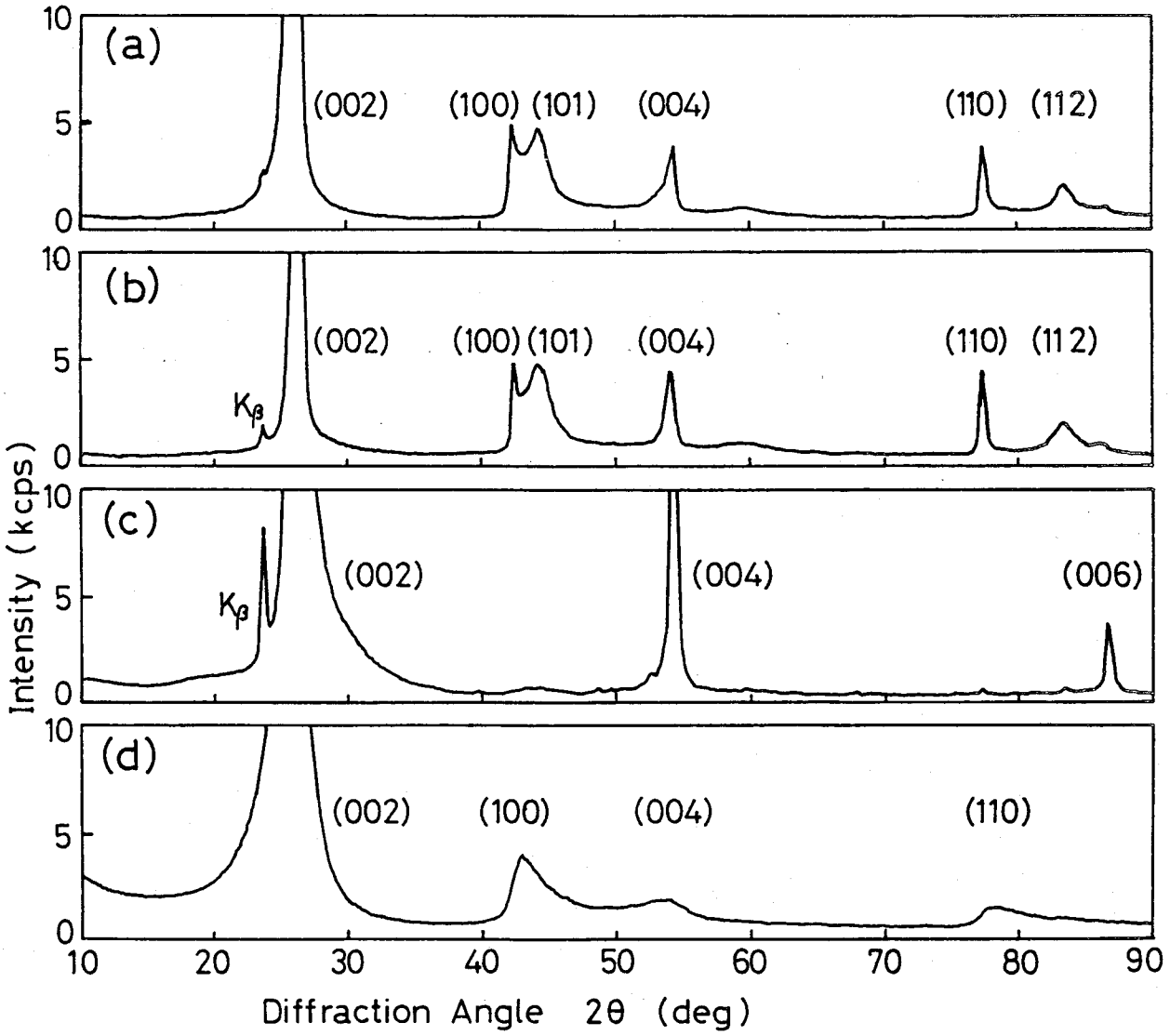

Fig. 2-3 X-ray diffraction patterns of graphite samples.
(a) ISOGRAPH-88 , (b) POCO DFP-3-2 , (c) PAPYEX , (d) GC-30 .

observation. Glassy carbon is believed to have a network structure which consists of condensed aromatic ribbon molecules (Fig. 2-2) [2].

X-ray diffraction patterns of these graphite samples are shown in Fig.2-3. Apparently, this figure shows ISOGRAPH-88 and POCO DFP-3-2 are typical isotropic graphite which have both peaks for basal planes ((002),(004); direction parallel to c-axis) and prism planes ((100),(110); direction parallel to a-axis). The diffraction pattern of PAPYEX apparently shows the strong orientation to the basal plane. As for GC-30, each peak is broad and obscure, therefore, this sample probably has a low graphitization or minute crystallite. In this study, ISOGRAPH-88 and POCO DFP-3-2 have been considered on the difference of crystallographic parameters. Table 2-2 lists the diffraction angle and the full width at half maximum (FWHM) of each peak calibrated with standard silicon powder. Lattice constants, size of crystallite and degrees of graphitization were obtained with the method reported by Noda and Akamatsu et al. [3] and by Inagaki [4]. These values are listed in Table 2-3. Degrees of graphitization do not differ significantly, however, the sizes of crystallite are different in the parallel direction to basal plane. This difference may affect the variety of surface deformation under ion irradiation.

Table 2-2 X-ray diffraction angles of ISOGRAPH-88 and POCO DFP-3-2.

	ISOGRAPH-88		POCO DFP-3-2	
Miller index	peak (2θ)	FWHM (Δθ)	peak (2θ)	FWHM (Δθ)
(002)	26.385	0.414	26.374	0.470
(004)	54.464	0.660	54.394	0.648
(110) $K\alpha_1$	77.487	0.241	77.532	0.296
(110) $K\alpha_2$	77.723	0.245	77.772	0.306
(112)	83.607	1.136	83.569	1.484

Table 2-3 Crystallographic parameters of ISOGRAPH-88 and POCO DFP-3-2.

		ISOGRAPH-88	POCO DFP-3-2
lattice constant	a_0	2.4596 Å	2.4583 Å
	c_0	6.7323 Å	6.7374 Å
size of crystallite	//a	62.1 nm	46.0 nm
	⊥a	23.2 nm	20.4 nm
degree of graphitization *		0.624	0.578

* Flanklin's P value [5]

3. Surface observations on graphite

Surface topography of the graphite samples irradiated by D_2^+ and He^+ ions was examined mainly by SEM. In this chapter, as preliminary considerations, surface observations on graphite have been performed with a SEM and an optical microscope. Figure 2-4 shows the optical micrographs of four graphite samples. The grain size and pore distribution of isotropic

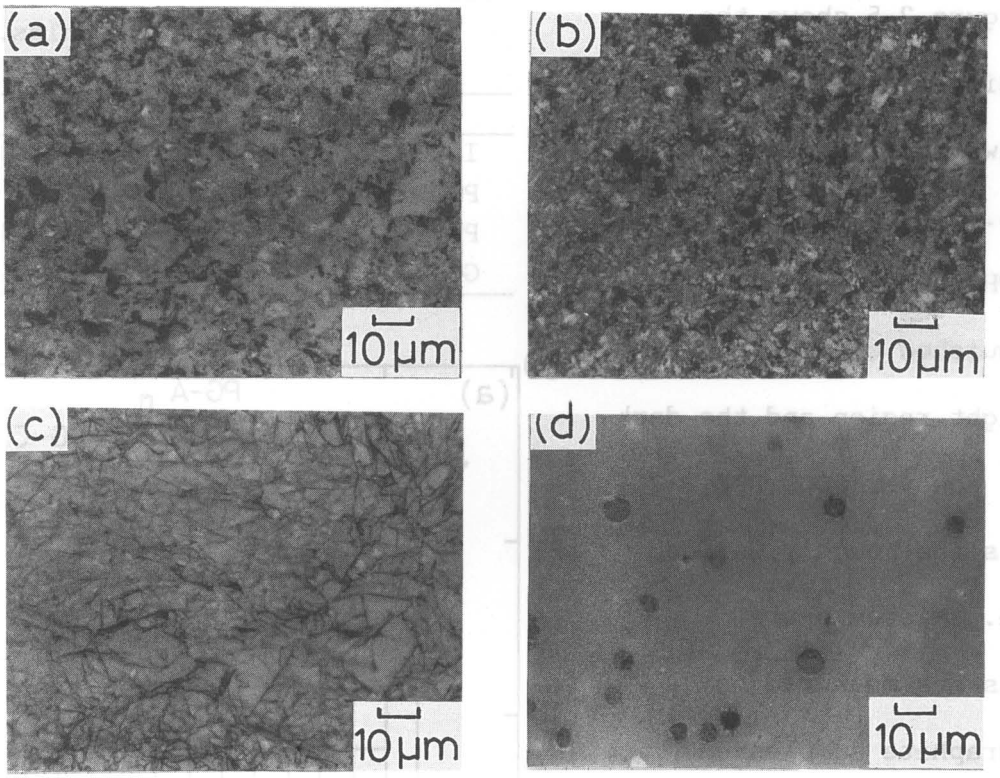

Fig. 2-4 Optical surface micrographs of graphite samples.
(a) ISOGRAPH-88 , (b) POCO DFP-3-2 , (c) PAPYEX , (d) GC-30 .

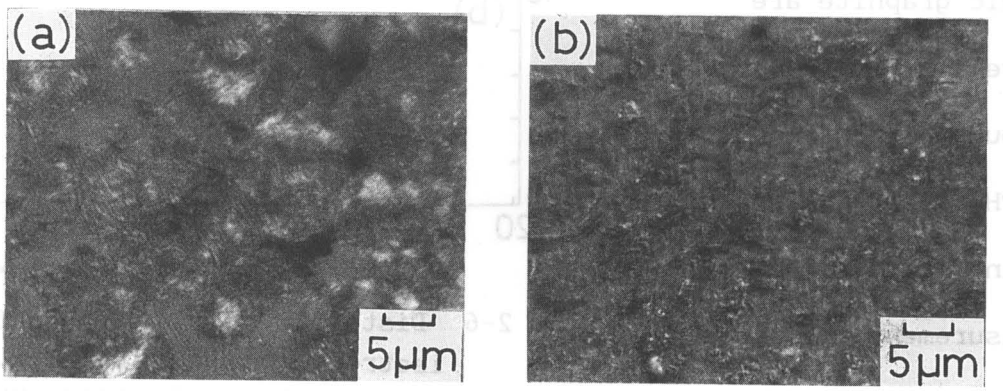

Fig. 2-5 Polarizing surface micrographs of isotropic graphite samples.
(a) ISOGRAPH-88 , (b) POCO DFP-3-2 .

graphite samples (ISOGRAPH-88 and POCO DFP-3-2) can be clearly seen in these optical micrographs. The grain sizes of ISOGRAPH-88 and POCO DFP-3-2 are approximately identical. PAPYEX had the bright surface due to high reflectance. GC-30 has several spherical pores within the flat surface (Fig. 2-4(d)). For the surface observations, ISOGRAPH-88 and POCO DFP-3-2 have been examined in detail.

Figure 2-5 shows the polarizing micrographs of these two isotropic graphite samples. The surface of ISOGRAPH-88 can be distinguished clearly between the bright region and the dark region, however POCO DFP-3-2 exhibits the roughly uniform surface. Microvickers hardness was measured on these graphite samples and listed in Table 2-4. Distributions of hardness for isotropic graphite are displayed in Fig. 2-6. The distribution of hardness for ISOGRAPH-88 spreads in the wide range of 19-1880. From the measurements of microvickers hardness on ISOGRAPH-88, it was found that

Table 2-4 Microvickers hardness of graphite samples.

Sample	VHN
ISOGRAPH-88	386 ± 351
POCO DFP-3-2	163 ± 54
PAPYEX	0.44 ± 0.12
GC-30	889 ± 102

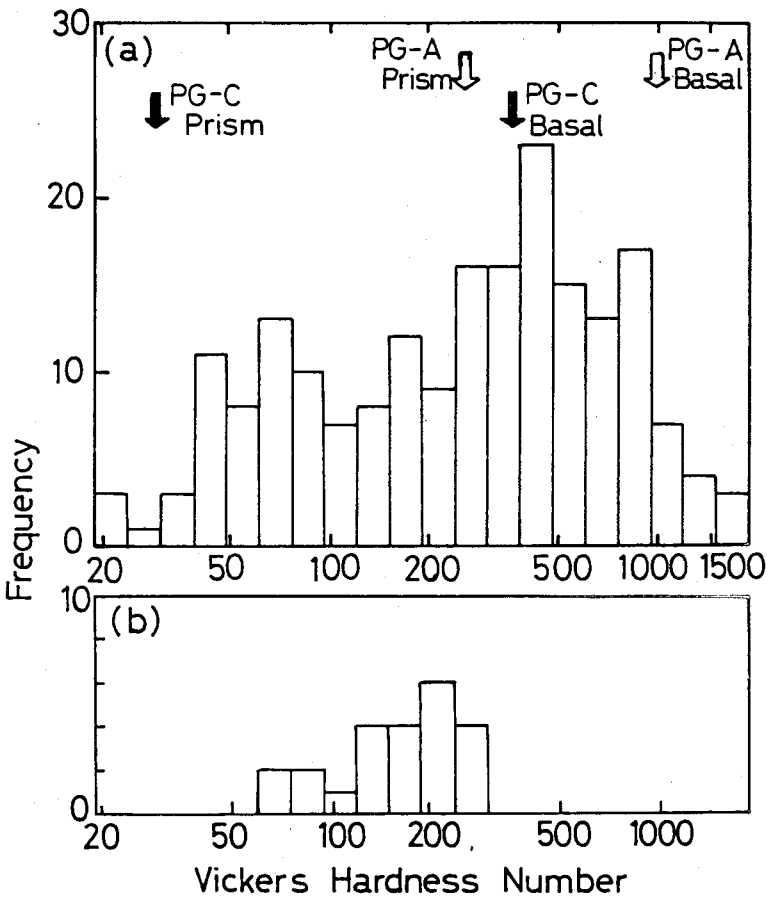

Fig. 2-6 Distribution of hardness for isotropic graphite samples.
(a) ISOGRAPH-88 , (b) POCO DFP-3-2 .
(PG-A : Carbonaceous pyrolytic carbon
PG-C : Graphitized pyrolytic carbon)

the bright region in the polarizing micrograph (Fig.2-5(a)) had higher hardness and the dark region had lower hardness. As for POCO DFP-3-2, the hardness numbers are nearly constant at around 160. For the above reasons, it may be safely assumed that POCO DFP-3-2 is composed of isotropic grains which have random oriented crystallite and ISOGRAPH-88 is composed of strongly anisotropic grains.

SEM surface observations have also performed for preliminary

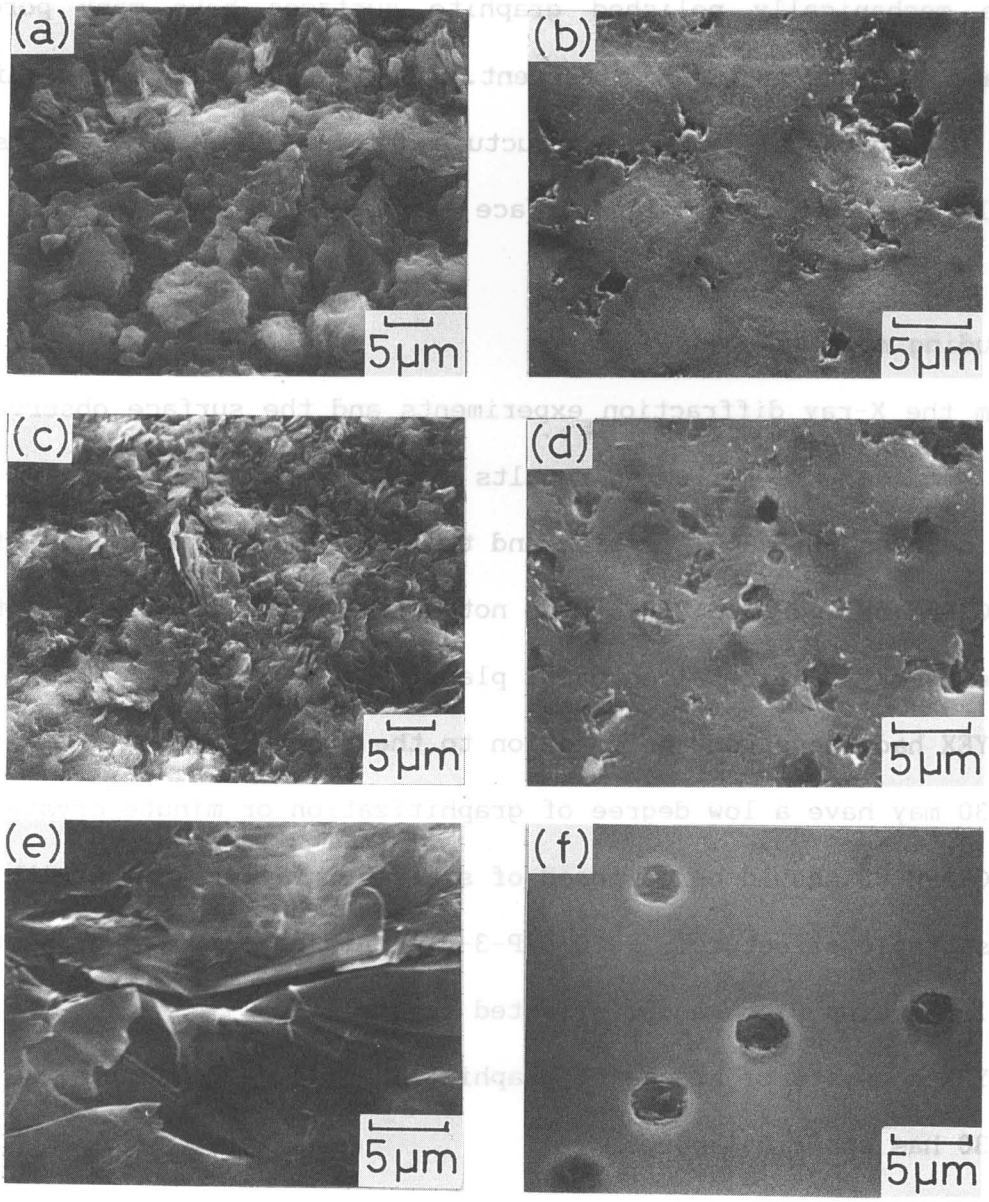

Fig. 2-7 SEM surface micrographs of graphite samples.
(a) ISOGRAPH-88, in section (b) ISOGRAPH-88, polished
(c) POCO DFP-3-2, in section (d) POCO DFP-3-2, polished
(e) PAPYEX, as-received (f) GC-30, polished

considerations. Figure 2-7 shows the SEM micrographs of the surfaces in section ((a) and (c)) and polished surfaces ((b), (d) and (f)). These carbon samples were given a fine mechanical polish with Al_2O_3 suspension (ISOGRAPH-88 and POCO DFP-3-2) and diamond paste (GC-30). The PAPYEX sample was not polished to avoid peeling. The shapes and dimensions of grains of two isotropic graphite samples can be clearly seen in the micrographs of the surfaces in section (Figs. 2-7(a) and (c)). As shown in Figs. 2-7(b) and (d), the mechanically polished graphite surfaces have many pores whose shapes and sizes are quite different. The PAPYEX samples significantly exhibits the stacks of lamellar structure (Fig. 2-7(e)). GC-30 has several spherical pores within the flat surface (Fig. 2-7(f)), as described before.

4. Concluding remarks

From the X-ray diffraction experiments and the surface observations of graphite samples, the following results can be summarized.

(1) The degrees of graphitization and the dimensions of crystallite of ISOGRAPH-88 and POCO DFP-3-2 do not differ significantly except for the size of crystallite along basal plane.

(2) PAPYEX had the strong orientation to the basal plane.

(3) GC-30 may have a low degree of graphitization or minute crystallite.

(4) ISOGRAPH-88 should be composed of spherical filler grains with strongly anisotropic structure. POCO DFP-3-2 should be composed of isotropic filler grains with random oriented crystallite.

(5) PAPYEX consists of stacks of graphite lamella (~ 0.1 μm).

(6) GC-30 has spherical pores.

References

[1] W.D.Kingery, H.K.Bowen and D.R.Uhlmann, "Introduction to ceramics, 2nd edition" (John Wiley & Sons, New York, 1975) p.80.

[2] G.M.Jenkins and K.Kawamura, "Polymeric Carbons - Carbon Fibre, Glass and Char" (Cambridge University Press, Cambridge, 1976) p.67.

[3] Nihon gakujutu shinkoukai dai-117 iinkai ed., Tanso 1963 (no.36) (1963) 25 (in Japanese).

[4] M.Inagaki, in "Tansozairyou jikkengijutu 1" (Kagaku Gijutu-sha, Tokyo, 1978) p.55 (in Japanese).

[5] R.E.Franklin, Acta Cryst. 4 (1951) 253.

Ⅲ Surface Erosion of Graphite by D_2^+ Ion Irradiation

1. Introduction

There are various types of carbon such as isotropic graphite, pyrolytic graphite and glassy carbon. The erosion behavior caused by D_2^+ ion irradiation is quite different among the types of graphite. There are several studies concerning the surface erosion of pyrolytic graphite samples by energetic hydrogen isotope ions [1-5], but little information is available on the other types of graphite. For practical use of graphite, the surface erosion under various conditions is required to be studied.

In this chapter, the surface erosion of different types of graphite by 20 keV D_2^+ ion irradiation has been studied with attention to the change in surface features as the results of irradiation.

2. Review of previous works

A number of investigators have been reported on graphite surface erosion for various types of graphite by ion (H^+, D^+, He^+) irradiation. In this section, the typical surface deformation reported by several authors [1,4,6] is shown to consider the diffence of surface features obtained by these authors and those obtained in this study. Figure 3-1 shows the SEM surface micrographs after H^+ and D^+ ion irradiation. Figures 3-1(a) and (b) are the surfaces of pyrolytic graphite with prism plane orientation reported by Roth et al [1]. After irradiation to a very high irradiation dose, the surface exibits the smooth features (Fig.3-1(b)). Sone et al.[4] have reported the blister formation by H_2^+ ion irradiation on pyrolytic graphite with basal plane orientation (Fig.3-1(c)). Further irradiation to the graphite leads these blisters to be blown away and become smoother (Fig.3-1(d)). The formation of ridges and grooves was reported by Das et al.[6]

for ATJ graphite (extrusion molded, Union Carbide Ltd.) irradiated with D^+ ions. They measured the spacing between the ridges (measured from peak to peak) to be 0.65-3.5 μm depending on projectile energy and total irradiation doses. The properties of ATJ graphite is similar to those of ISOGRAPH-88 and POCO DFP-3-2 used in the present study, but ATJ is one of the anisotropic graphite. As mentioned above, the surface deformation due

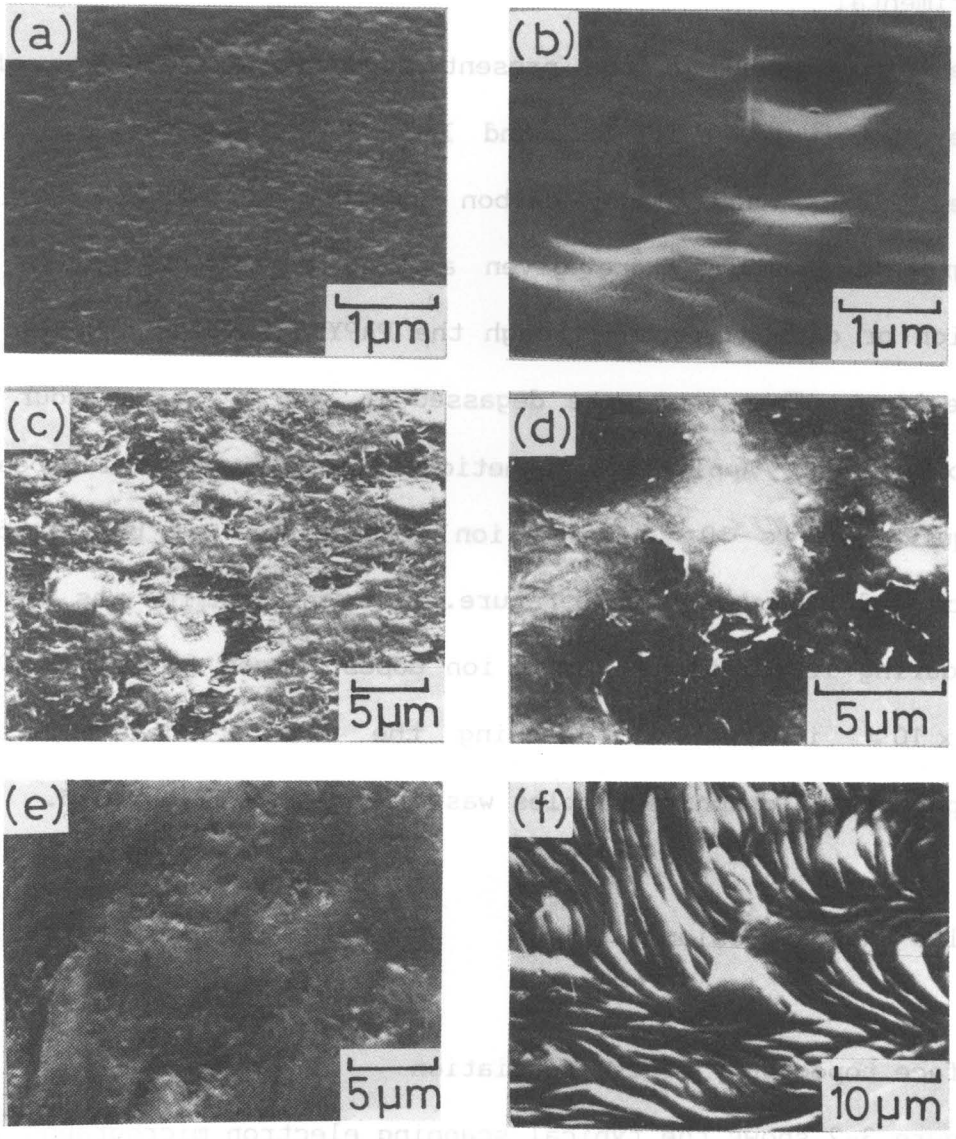

Fig. 3-1 Typical surface deformation by H^+ and D^+ ion irradiation.
edge-oriented pyrolytic graphite [1] (a) unirradiated
(b) 3 keV H_3^+ , 3×10^{20} ions/cm^2
basal-oriented pyrolytic graphite [4] (c) 200 keV H_2^+, 1×10^{18} ions/cm^2
(d) 200 keV H_2^+, 5×10^{18} ions/cm^2
ATJ graphite [6] (e) unirradiated
(f) 120 keV D^+, 1.7×10^{18} ions/cm^2

to ion irradiation is quite different among the types of graphite and irradiation conditions. The main mechanism of surface deformation have been proposed as the results of specific upliftings due to the formation of gas bubbles [4,6] or the crystal growth (i.e. twinning) [7,8]. These deformation mechanisms must be considered in this work.

3. Experimental

The sample used in the present study were two types of isotropic graphite sheets (POCO DFP-3-2 and ISOGRAPH-88), exfoliated recompressed graphite (PAPYEX) and glassy carbon (GC-30). Prior to ion irradiation, these graphite samples were given a fine mechanical polish with Al_2O_3 suspension or diamond paste, though the PAPYEX samples was not polished to avoid peeling. Then they were degassed at 1400 ℃ for an hour in a vacuum below 1×10^{-3} Pa. Applying a magnetically mass analyzed ion beam of 20 keV D_2^+ (equivalent to 10 keV D^+), ion irradiation was performed at normal incidence and at ambient temperature. Current density was kept up to 1.0 mA/cm² during irradiation. Total ion doses ranged from 5.0×10^{16} ions/cm² to 2.0×10^{19} ions/cm². Following the ion irradiation, the surface topography of the graphite samples was examined mainly by SEM.

4. Results and discussion

4.1 Surface topography after irradiation

Figure 3-2 shows the typical scanning electron micrographs of POCO DFP-3-2 and ISOGRAPH-88 after irradiation with D_2^+ ions at various doses. These two are both high-density isotropic graphites. The physical and mechanical properties of these samples are similar, though ISOGRAPH-88 is slightly harder than POCO DFP-3-2 (Table 2-1 and 2-4). As shown in Figs.3-2(a)

and (e) the mechanically polished graphite surfaces have pores whose shapes and sizes are quite different. The micrograph of the POCO graphite sample irradiated to a dose of 5.0×10^{17} ions/cm^2 shows uniform wrinkles (Fig.3-2(b)). At a dose of 2.0×10^{18} ions/cm^2, these wrinkles were likely disappear by successive ion irradiation (Fig.3-2(c)). Further irradiation made the surface smoother, yet several depressions were still present (Fig.3-2(d)). These depressions appear to correspond to the original pores. The smooth surface obtained at a high irradiation dose is similar to that of pyrolytic graphite showing smooth feature due to amorphisation reported by several authors (Fig.3-1(b)) [2,3].

As for ISOGRAPH-88, localized ridges and grooves were formed on the surface after irradiation with D_2^+ ions to a dose of 5.0×10^{17} ions/cm^2 (Fig.3-2(f)), while the wrinkles on the POCO graphite sample were uniform. At a dose of 2.0×10^{18} ions/cm^2, the ridges and grooves gradually disappeared, and surface deformation was developed (Fig.3-2(g)). At a dose of 5.0×10^{18} ions/cm^2, the surface showed scraped off and scalelike features with a great number of pits. However, after irradiation to a dose of 2.0×10^{19} ions/cm^2, the surface became a smooth feature with several dimples as observed in the case of POCO graphite (Fig.3-2(h)).

Figure 3-3 shows typical SEM micrographs of the surfaces of PAPYEX and glassy carbon. The PAPYEX sample exhibits significant lamellar structure (Fig.3-3(a)). A network of uplifting structure like leaf veins was developed by irradiation with D_2^+ ions to a dose of 2.0×10^{18} ions/cm^2. The surface became a smooth feature as well as the isotropic graphite as a result of subsequent irradiation to a dose of 2.0×10^{19} ions/cm^2 (Fig.3-3(c)). Glassy carbon has several sperical voids within the flat surface (Fig.3-3(d)). No marked change in surface features was observed after irradiation to a dose of 2.0×10^{18} ions/cm^2 (Fig.3-3(e)), though the many

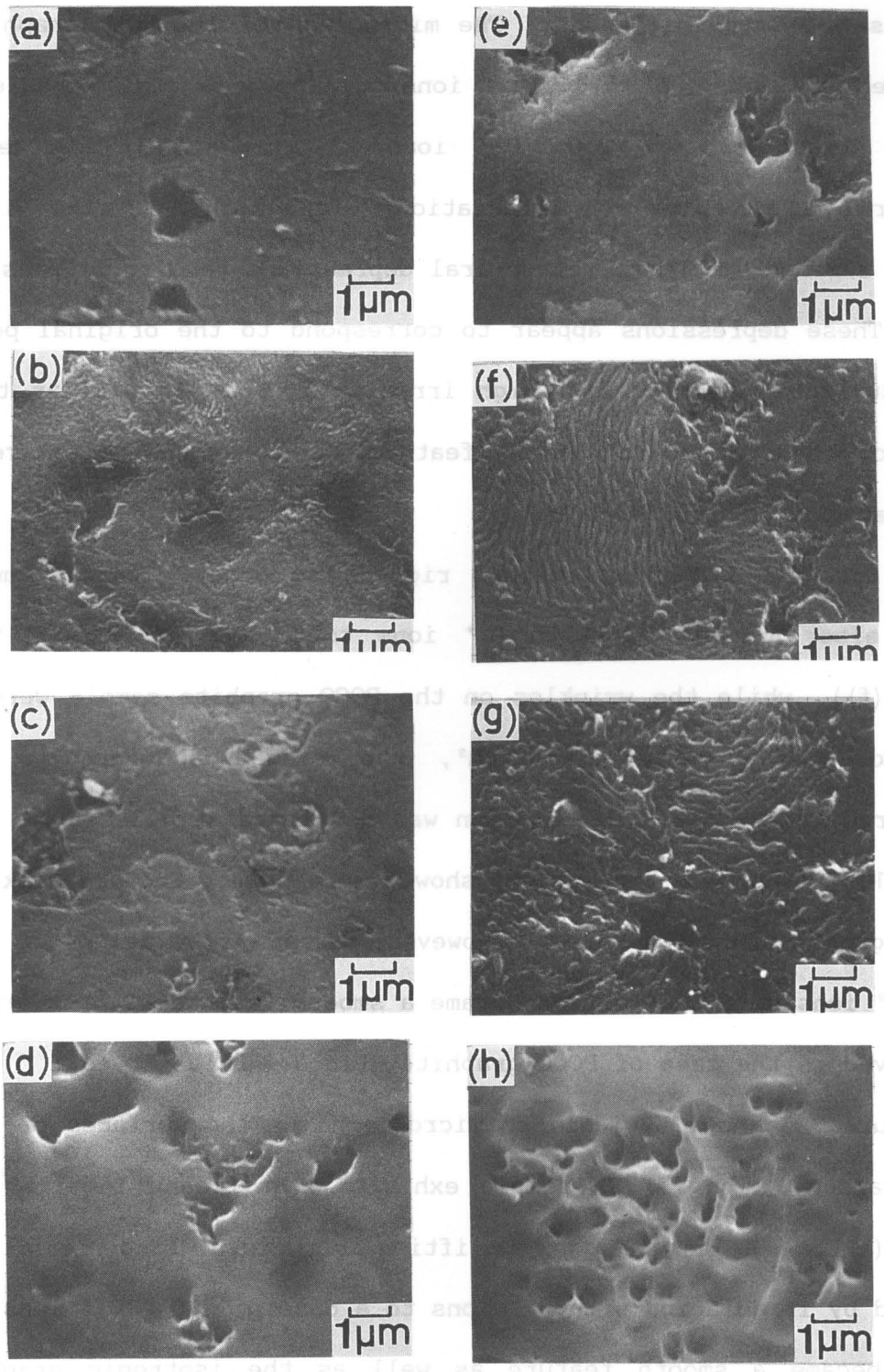

Fig. 3-2 SEM micrographs of isotropic graphite surfaces after irradiation of 20 keV D_2^+ ions to various doses.

POCO DFP-3-2

(a) as-polished
(b) 5.0×10^{17} ions/cm²
(c) 2.0×10^{18} ions/cm²
(d) 2.0×10^{19} ions/cm²

ISOGRAPH-88

(e) as-polished
(f) 5.0×10^{17} ions/cm²
(g) 2.0×10^{18} ions/cm²
(h) 2.0×10^{19} ions/cm²

small (< 0.1 μm) spots which might be derived from the redeposition of sputtered carbon were revealed. At a dose of 2.0×10^{19} ions/cm^2, the SEM micrograph shows that the voids appear to gradually close up (Fig.3-3(f)).

Through the D_2^+ ion irradiation at various doses in the present study, no spherical uplifting which can be clearly recognized to be blisters could be observed. This result differs from the results for pyrolytic graphite reported by Sone et al. (Fig.3-1(c)) [4].

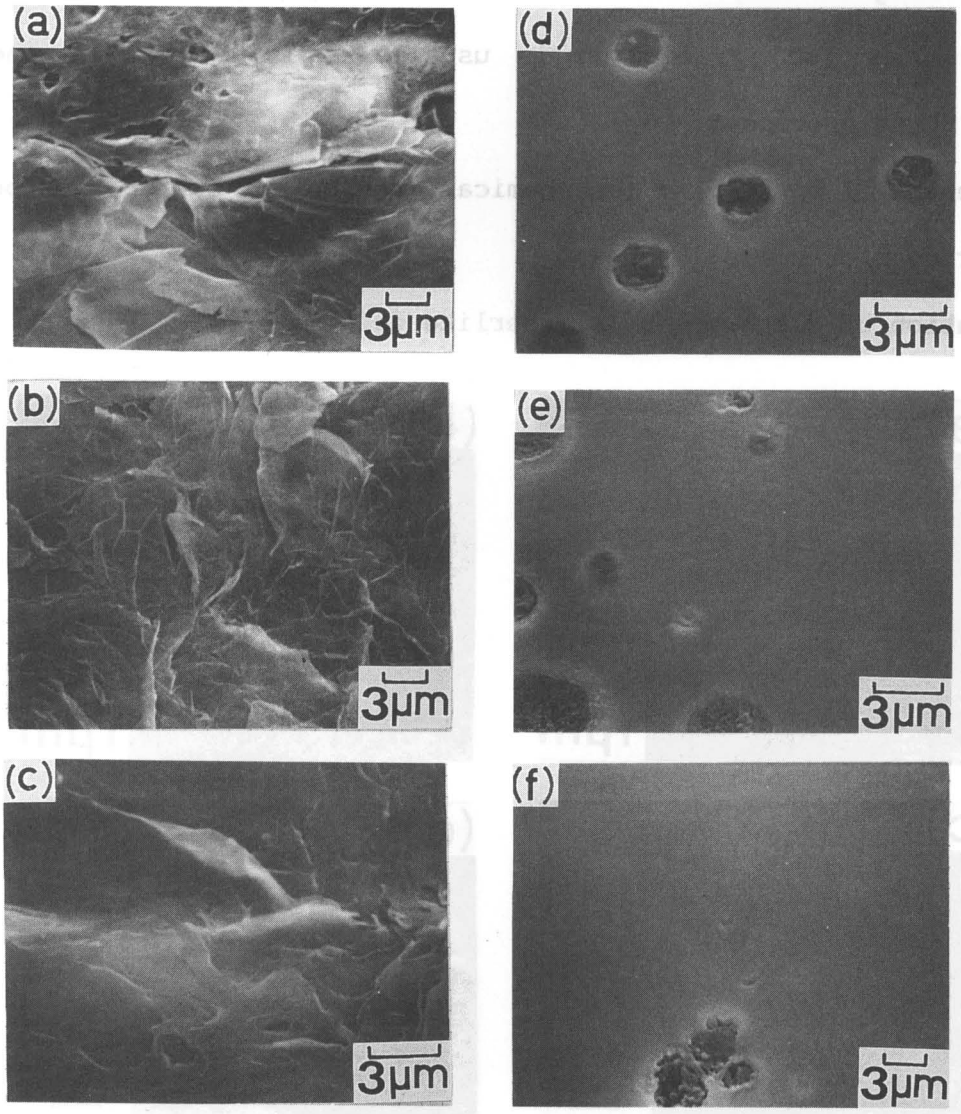

Fig. 3-3 SEM micrographs of PAPYEX and glassy carbon after irradiation of 20 keV D_2^+ ions.

PAPYEX

(a) as-received
(b) 2.0×10^{18} ions/cm^2
(c) 2.0×10^{19} ions/cm^2

Glassy carbon GC-30

(d) as-polished
(e) 2.0×10^{18} ions/cm^2
(f) 2.0×10^{19} ions/cm^2

4.2 Surface deformation process

The formation of ridges and grooves was reported on ATJ graphite irradiated with D^+ ions [6], and on WCA graphite [9] and Le Carbone Lorraine 7477PT [10] irradiated with He^+ ions. The values of the spacing between ridges measured on WCA graphite were quite similar to those of ISOGRAPH-88 (mean value ~ 0.16 μm), however the values for ATJ (0.65-3.5 μm) and Le Carbone Lorraine 7477PT were considerably larger.

Roughening of material surface due to ridge, groove [6] or cone [4,11] formation under ion irradiation is usually explained by the one of the following three processes.

(1) Preferential sputtering (or chemical erosion) of surface surrounding the ridges or cones.

(2) Formation of gas bubbles (blisterlike deformation).

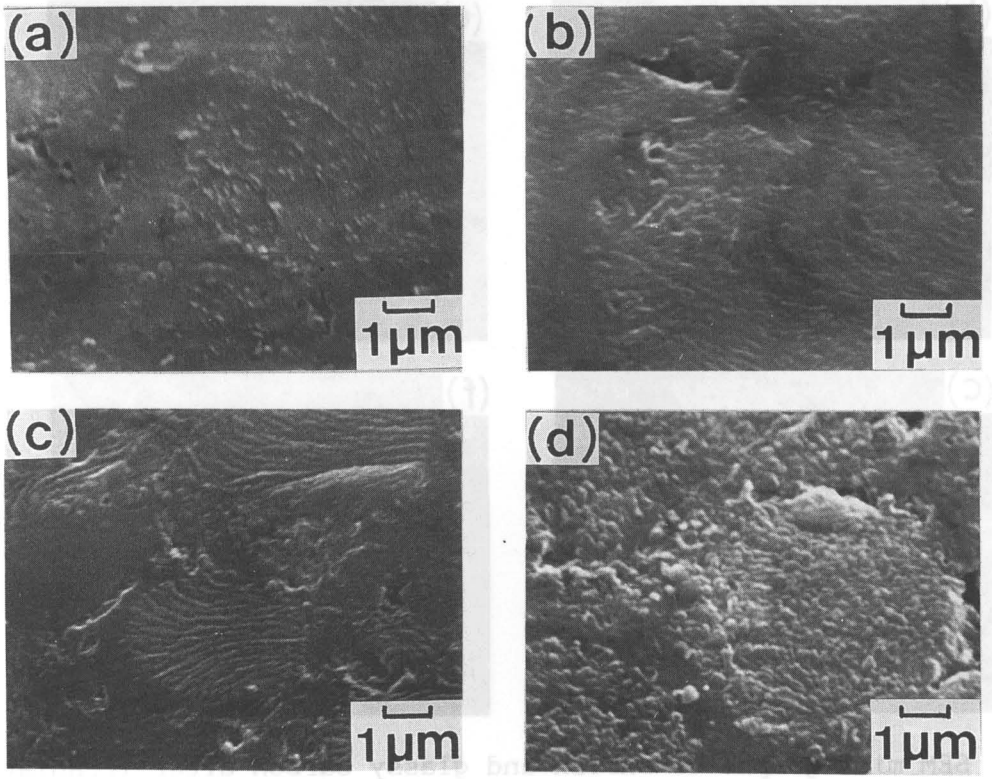

Fig. 3-4 SEM micrographs of irradiated ISOGRAPH-88 before and after isochronal annealing tests up to 1000 ℃.
(a) before (b) after ; 1.0×10^{17} ions/cm^2
(c) before (d) after ; 5.0×10^{17} ions/cm^2

(3) Volume change and associated stress accumulation in the lattice (a sort of crystal growth : e.g. twinning)

Assuming that the sputtering yield for pyrolytic graphite obtained by Bohdansky et al.[12] can be applied to the isotropic graphite, erosion thicknesses are estimated to be about 0.1 nm and 0.5 nm at irradiation doses of 1.0×10^{17} ions/cm^2 and 5.0×10^{17} ions/cm^2, respectively. Due to the small values of thickness loss, preferential sputtering cannot lead to the surface deformation shown in Fig.3-2(f),(g). Therefore, ridge and groove formation should not be caused by the process (1). To define the process which leads to the ridge and groove formation, annealing tests up to 1000℃ in a vacuum were carried out. Figure 3-4 shows typical surface micrographs before and after annealing tests on ISOGRAPH-88, in which the graphite samples were heated isochronally up to 1000℃. After the annealing, the surface of ISOGRAPH-88 irradiated to a dose of 1.0×10^{17} ions/cm^2 exhibits wrinkly feature (Fig.3-4(b)), and the surface irradiated to a dose of 5.0×10^{17} ions/cm^2 exhibits warty feature (Fig.3-4(d)). There is no evidence of cracks and flakes caused by gas bursts and blowing away of blister covers. On the other hand, no marked change in surface features through the annealing tests was observed for the sample with a total irradiation dose above 5.0×10^{18} ions/cm^2. As described above, the surface topography of ion irradiated ISOGRAPH-88 was changed more definitely after thermal annealing, as compared with that of POCO graphite. Implanted deuterium ions will be retained in the graphite around the projected range. Accordingly, during the annealing, implanted deuterium will be released from graphite samples. Figure 3-5 shows typical thermal desorption curves of D_2 and CD_4 determined by quadrupole mass spectrometer for ISOGRAPH-88 irradiated with D_2^+ ions to a dose of 5.0×10^{17} ions/cm^2. Many acute gas burst peaks during He^+ ion irradiation to pyrolytic graphite were observed

in the re-emission experiments by Saido et al.[10] (Fig.3-6). Since the desorption peaks of D_2 and CD_4 obtained in the present study (Fig.3-5) were quite different from that of the gas bursts[10] (Fig.3-6), these peaks did not appear to result from gas burst due to blister explosion. In such case, the deformation during annealing might be caused by release of residual stress within the graphite filler particles as reported by several authors [11,12] for graphite after He^+ ion irradiation. These facts suggest the roughening, and ridge and groove formation observed at relatively lower doses should take place due to volume change and stress accumulation in the graphite lattice during irradiation. Since the surface deformation was enlarged due to annealing, this explanation may be supported.

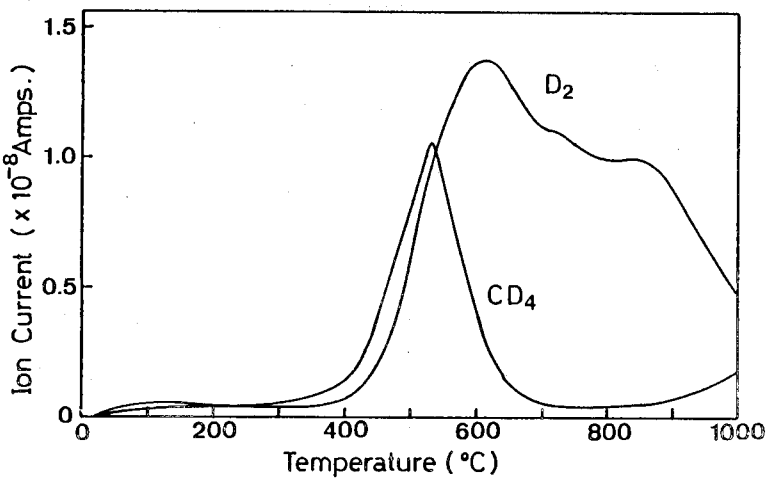

Fig. 3-5 Thermal desorption curves of D_2 and CD_4 from graphite irradiated with 20 keV D_2^+ ions to a dose of 5.0×10^{17} ions/cm² (heating rate : 10 ℃/min).

Above a dose of 5.0×10^{18} ions/cm², the sputtering process would be more predominant on the structural changes of graphite surface rather than the deformation due to volume change taking place at lower doses. Accordingly, the

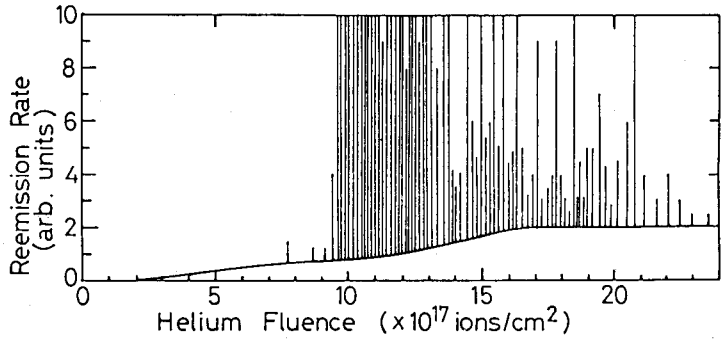

Fig. 3-6 Helium re-emission rate as a function of the fluence of 200 keV helium ions at ambient temperature in basal-oriented pyrolytic graphite (polished surface). (from ref.[10])

graphite surface with ridges and grooves would be gradually scraped off with increasing irradiation dose.

The difference in the topography between ISOGRAPH-88 and POCO DFP-3-2 has been examined in the crystallographic characters. Microvickers hardness of these graphite samples irradiated to a dose of 5.0×10^{17} ions/cm^2 was measured. The results obtained for ISOGRAPH-88 are shown in Fig.3-7. The distribution of hardness for ISOGRAPH-88 covers a wide range. It can be clearly seen that the region with ridges and grooves has lower hardness, on the other hand, the region without ridge has higher hardness. As described in Chapter Ⅱ, the bright region in the polarizing micrograph (**Fig.2-5(a)**) had high hardness and the dark region had low hardness. From the polarizing surface micrographs of ISOGRAPH-88 after D_2^+ ion irradiation, the dark region had ridges and grooves, and the bright region did not have ridges without exception. Therefore, in the case of ISOGRAPH-88, the grains with prism plane orientation gives the ridges and grooves after D_2^+ ion irradiation, and the grains with basal plane orientation does not give the

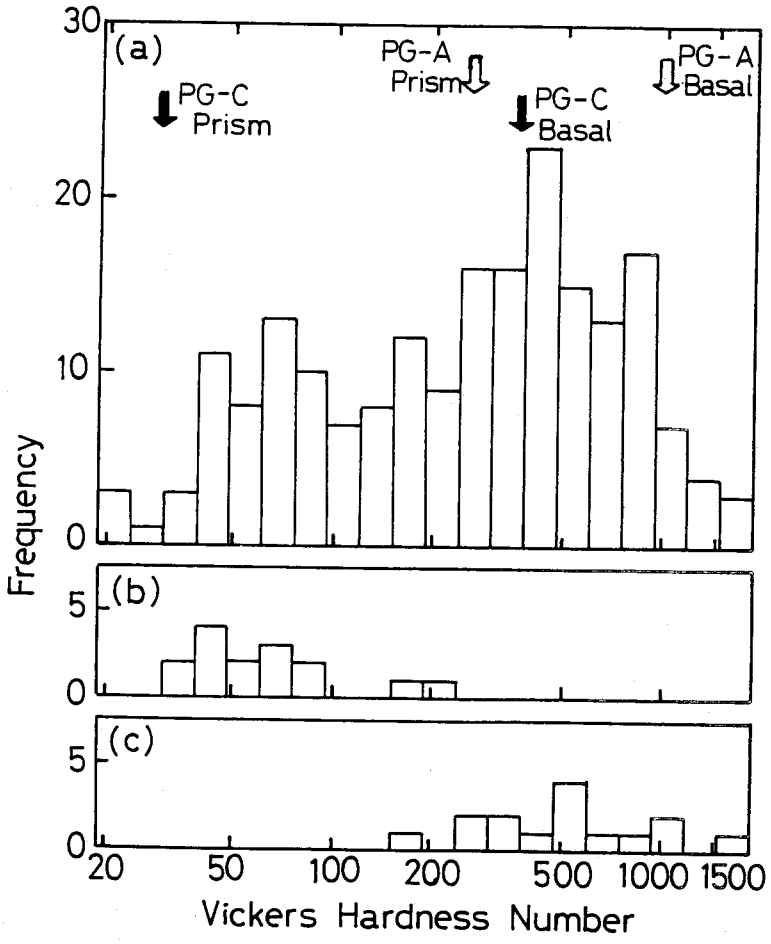

Fig. 3-7 Distribution of hardness for ISOGRAPH-88 after irradiation of D_2^+ ions to a dose of 5.0×10^{17} ions/cm^2.
(a) as-polished
(b) region with ridge
(c) region without ridge

ridges. In the case of POCO DFP-3-2, the hardness numbers are nearly constant and the polarizing micrograph shows relatively uniform brightness (Figs.2-5 and 2-6). Namely, POCO DFP-3-2 should be composed of isotropic grains. And the surface of POCO DFP-3-2 irradiated with D_2^+ ions would naturally show the uniform surface deformation. For the above reasons, the difference of surface topography between the two isotropic graphite is attributed to the orientation of filler grains, and the significant surface deformation will be generated on the surface with prism orientation. This hypothesis may be supported by the facts that ridge and groove formation was observed on the prism plane of pyrolytic graphite irradiated by He^+ ions [10].

The PAPYEX sample showed a network uplifting (Fig.3-3(b)). The network formation has also been observed on the basal plane of pyrolytic graphite irradiated with He^+ ions (Figs.4-1(a),(b)) [14-17]. The network observed on the basal plane is consistent with that observed on PAPYEX, whose surface is parallel to the basal plane, in the present work.

Glassy carbon has the minimum surface deformation among the four types of carbon materials studied in the present work. This might be caused by the random structure of glassy carbon, while the isotropic graphite has polycrystalline structure and an anisotropy on a microscopic scale. Namely, glassy carbon does not grow or expand in a specific direction.

The deformation with network structure on the basal plane of highly oriented graphite is generally explained by the twinning produced by displacement damage [7,8]. In such a case, twinning provides a network of steps on the surface of natural and pyrolytic graphite which have relatively simple structure. However, artificial graphite, including POCO and ISOGRAPH-88, with complicated structure shows quite different surface deformation [6,10,14,18] which might be caused by the shape, size and orientation of

crystallite within each graphite grain and by the degree of graphitization.

As described before, there is no evidence of blistering on these four graphite samples, while in the case of pyrolytic graphite, for example, blister formation above a dose of 1.0×10^{18} ions/cm^2 with 200 keV H_2^+ ions was reported by Sone et al (**Figs.3-1(c), (d)**) [4]. Blister formation and following exfoliation or flaking lead to a great increase of effective sputtering loss of materials. Therefore, from this standpoint, these four graphite samples might have an advantage over pyrolytic graphite, if the blister formation does not appear under the same irradiation conditions with pyrolytic graphite.

5. Concluding Remarks

Surface erosion of various types of carbon by 20 keV D_2^+ ions has been observed. The main results of this study can be summarized as follows:

(1) The surfaces of isotropic graphite (POCO DFP-3-2 and ISOGRAPH-88) exhibit deformation in the form of wrinkles, ridges and grooves at lower doses (5.0×10^{17} ions/cm^2), and smooth features at higher doses (2.0×10^{19} ions/cm^2). These changes in surface may be explained by an initial volume change due to stress accumulation and subsequent uniform sputtering erosion. The difference of surface topography between ISOGRAPH-88 and POCO DFP-3-2 after D_2^+ ion irradiation may be attributed to the orientation of filler grains. And the significant surface deformation will be occurred on the grain surface with prism plane orientation.

(2) As for PAPYEX irradiated to a dose of 2.0×10^{18} ions/cm^2, the surface exhibits network uplifting structure, which might be formed by the twinning as reported on natural graphite. Further irradiation produces smooth features on the surface.

(3) Glassy carbon has the minimum surface deformation among the four types of carbon after the ion irradiation up to 2.0×10^{19} ions/cm^2. Many small spots and closing up the pores were observed at a dose of 2.0×10^{18} ions/cm^2 and 2.0×10^{19} ions/cm^2, respectively.

Refereces

[1] J.Roth, J.Bohdansky, W.Poschenrieder and M.K.Sinha, J.Nucl.Mater. 63 (1976) 222.

[2] J.Bohdansky, J.Roth and M.K.Sinha, "Fusion Technology 1976": Proc. 9th Symp. on Fusion Technology, Garmisch-Partenkirchen (1976) p.541.

[3] R.Behrisch, J.Bohdansky, G.H.Oetjen, J.Roth, G.Schilling and H.Verbeek, J.Nucl.Mater. 60 (1976) 321.

[4] K.Sone, T.Abe, K.Obara, R.Yamada and H.Ohtsuka, J.Nucl.Mater. 71 (1977) 82.

[5] K.Watanabe, M.Sasaki, M.Mohri and T.Yamashina, J.Nucl.Mater. 76/77 (1978) 235.

[6] S.K.Das, M.Kaminsky, R.Tishler and J.Cecchi, J.Nucl.Mater. 85/86 (1979) 225.

[7] D.J.Bacon and A.S.Rao, J.Nucl.Mater. 91 (1980) 178.

[8] D.J.Bacon, I.Dümler and A.S.Rao, J.Nucl.Mater. 103/104 (1981) 427.

[9] B.Feinberg and R.S.Post, J.Vac.Sci.Technol. 13 (1976) 443.

[10] M.Saidoh, R.Yamada and K.Nakamura, J.Nucl.Mater. 102 (1981) 97.

[11] R.S.Gvosdover, V.M.Efremenkova, L.B.Shelyakin and V.E.Yurasova, Radiat. Eff. 27 (1976) 237.

[12] J.Bohdansky, H.L.Bay and W.Ottenberger, J.Nucl.Mater. 76/77 (1978) 163.

[13] S.Veprek, A.Portmann, A.P.Webb and H.Stuessi, Radiat.Effects 34 (1977)

82.

[14] B.Navinsek, Fusion Technol. 6 (1984) 491.

[15] S.Vepřek, A.P.Webb, H.R.Oswald and H.Stuessi, J.Nucl.Mater. 68 (1977) 32.

[16] Y.Kazumata, J.Nucl.Mater. 68 (1977) 257.

[17] H.Stuessi, S.Vepřek and A.P.Webb, Radiat.Effects Letters 43 (1979) 133.

[18] L.H.Rovner and K.Y.Chen, J.Nucl.Mater. 63 (1976) 307.

Ⅳ Surface Erosion of Graphite by He^+ Ion Irradiation

1. Introduction

In Chapter Ⅲ, surface erosion of different types of graphite by D_2^+ ion irradiation was studied, and entirely different surface deformation could be observed.

In this chapter, surface erosion and surface deformation have been studied on various types of graphite irradiated with 20 keV He^+ ions. The sputtering yield for graphite by helium ions is approximately five times as much as that for deuterium at the same projectile energy [1]. The surface erosion behavior has been studied paying special attention to changes in surface feature and surface uplifting with an irradiation dose.

2. Review of previous works

There are various types of graphite and the erosion behavior is quite different among the types of graphite. Furthermore, the projectile energy of He^+ ions and the irradiation dose should lead to appear various surface deformation. There are relatively large number of studies concerning on pyrolytic graphite samples [2-13], but a little information is available on artificial graphite (e.g. isotropic graphite) [12-17] (refs [16,17] are the papers presented by the author). Especially on isotropic graphite as candidates for first walls in a fusion reactor, only LeCarbone 7477PT [11] and POCO graphite [14] have been studied previously. In this section, the typical surface deformation reported by several authors for various types of graphite is shown to consider the difference of surface features from this study.

Figure 4-1 shows the SEM surface micrographs of pyrolytic graphite after He^+ ion irradiation. Figures 4-1(a)-(e) are the surfaces of basal

oriented pyrolytic graphite, and Figs.4-1(f)-(h) show the surfaces of prism plane. Figure 4-1(a) shows a crystallite structure rimmed with edges of a few micrometers in height and high dense conical features inside the crystallite area [13]. After 100 keV He^+ ion irradiation at 1.0×10^{18} ions/cm^2, flaking of the first covers occurs (Fig.4-1(b)), and a cone structure appears at a further irradiation dose (Fig.4-1(c)) [7]. Many cones and cone-like protrusions are produced by the 200 keV He^+ ion irradiation (Fig.4-1(d)) [12]. The energetic ion irradiation causes radiation damage in the surface layer resulting in twinning, flaking and faulting (Fig.4-1(e)) [5]. In the case of the prism plane, the surface shows a small etch pits ,long and narrow grooves with a width of 0.1 to 0.2 μm (Fig.4-1(f)) [13]. Ridge and grooves with fibrous structure giving a lateral-striped pattern and exfoliation takes place (Figs.4-1(g),(h)) [12]. This feature is similar to the grain surface of ISOGRAPH-88 after D_2^+ ion irradiation (Figs.3-2(f) and 3-4(c)). Typical surface deformation of basal plane after He^+ ion irradiation can be regarded as network upliftings (Figs.4-1(a),(b),(c) and (d)). The network upliftings tend to appear in the case of the irradiation with relatively high projectile energy. And the domed or conical protrusions tend to appear after the irradiation at the lower projectile energy and at high irradiation doses. The sputtering yield of graphite for helium ions has a maximum at approximately 1 keV of ion energy [1,18]. And over 100 keV, the sputtering process cannot affect the surface deformation any longer. On the other hand, the displacement damage increases with the projectile energy of helium ions, therefore, volume expansion will be larger in the case of the irradiation at higher energy. From the above reasons, the network upliftings may be produced mainly by the displacement damage due to ion bombardment, and the domed or conical protrusions may be produced mainly by the erosion due to sputtering. As for

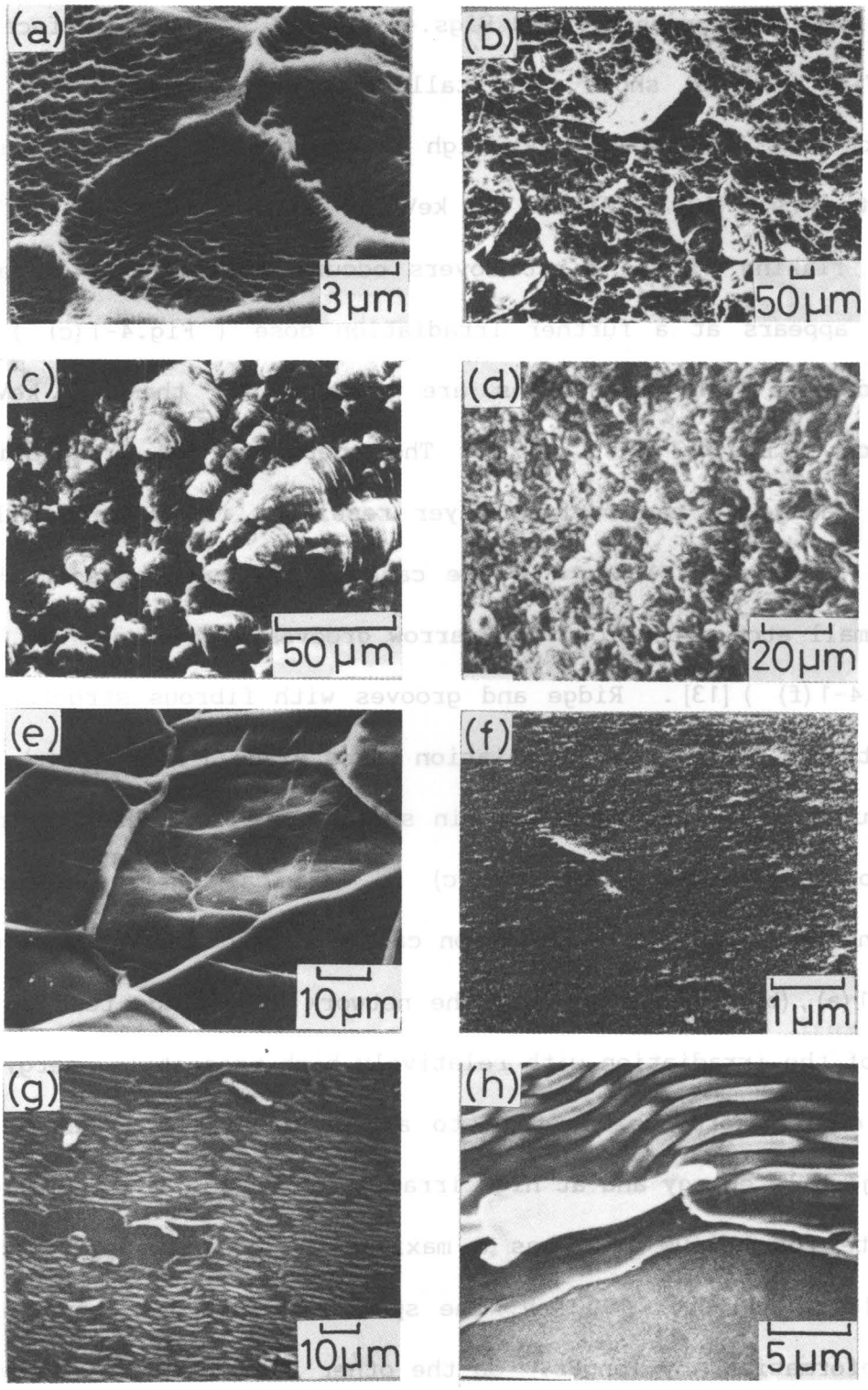

Fig. 4-1 Typical surface deformation of pyrolytic graphite irradiated by He^+ ions.

basal plane	(a)	10 keV He^+	2.2×10^{19} ions/cm²	[13]
	(b)	100 keV He^+	1.0×10^{18} ions/cm²	[7]
	(c)	100 keV He^+	5.0×10^{18} ions/cm²	[7]
	(d)	200 keV He^+	2.5×10^{18} ions/cm²	[12]
	(e)	2 MeV He^+	6.0×10^{17} ions/cm²	[5]
prism plane	(f)	10 keV He^+	3.5×10^{19} ions/cm²	[13]
	(g), (h)	200 keV He^+	2.5×10^{18} ions/cm²	[12]

prism plane, the ridge and groove formation can be seen after He^+ ion irradiation.

Figure 4-2 shows the typical surface deformation of artificial graphite after He^+ ion irradiation at various projectile energies and irradiation doses. A large surface area of ATJ graphite remaining resistant to 10 keV He^+ ion impact (Fig.4-2(b)), however grooves and narrow ridges are developed in the pores (Figs.4-2(a) and (b)) [13]. The formation of ridges and grooves on the surface of ATJ graphite has also reported by Das et al. (Fig.4-2(c)) [15]. This figure shows that the ridge and groove formation takes place uniformly, while in the case of Figs.4-2(a) and (b), the ridges and grooves appear in the pores. These difference of surface features may be caused by projectile energy of He^+ ions. Spacing and width of ridges in Fig.4-2(c) are relatively smaller as compared with those by the D_2^+ ion irradiation at similar projectile energy (Fig.3-1(f)). The ridge and groove formation should be related to the crystal orientation which is settled by the direction of extrusions during manufacturing. Saidoh et al.[12] divided the surface deformation of ridges and grooves into four groups which are : (1) well-aligned ridges, (2) two-dimensionally developed ridges, (3) spheroidal ridges, and (4) large bulging ridges. Figure 4-2(d) will belong to the group (3) and Fig.4-2(e) belongs to the group (1). For the POCO graphite, the surface after He^+ ion irradiationshows the spheroidal uplifting expanded by separation along the original particle boundaries (Fig.4-2(f)) [14].

There are two theories on the surface uplifting process of graphite irradiated by He^+ ions. One is the process of blister-like deformation due to the helium agglomeration into bubbles [7,12,14]. The conical and spheroidal upliftings seem to be produced by this process. The other is the process of the stress accumulation due to displacement damage [8,13]. This

process may produce the network upliftings and narrow ridges. Surface deformation of graphite should be produced by the competing of these processes and sputtering erosion. The dominative process of surface deformation may depend on the energy of He^+ ions, the total irradiation dose, properties of graphite samples, etc. Therefore, numerous data are needed to consider these processes on the graphite surface erosion by He^+

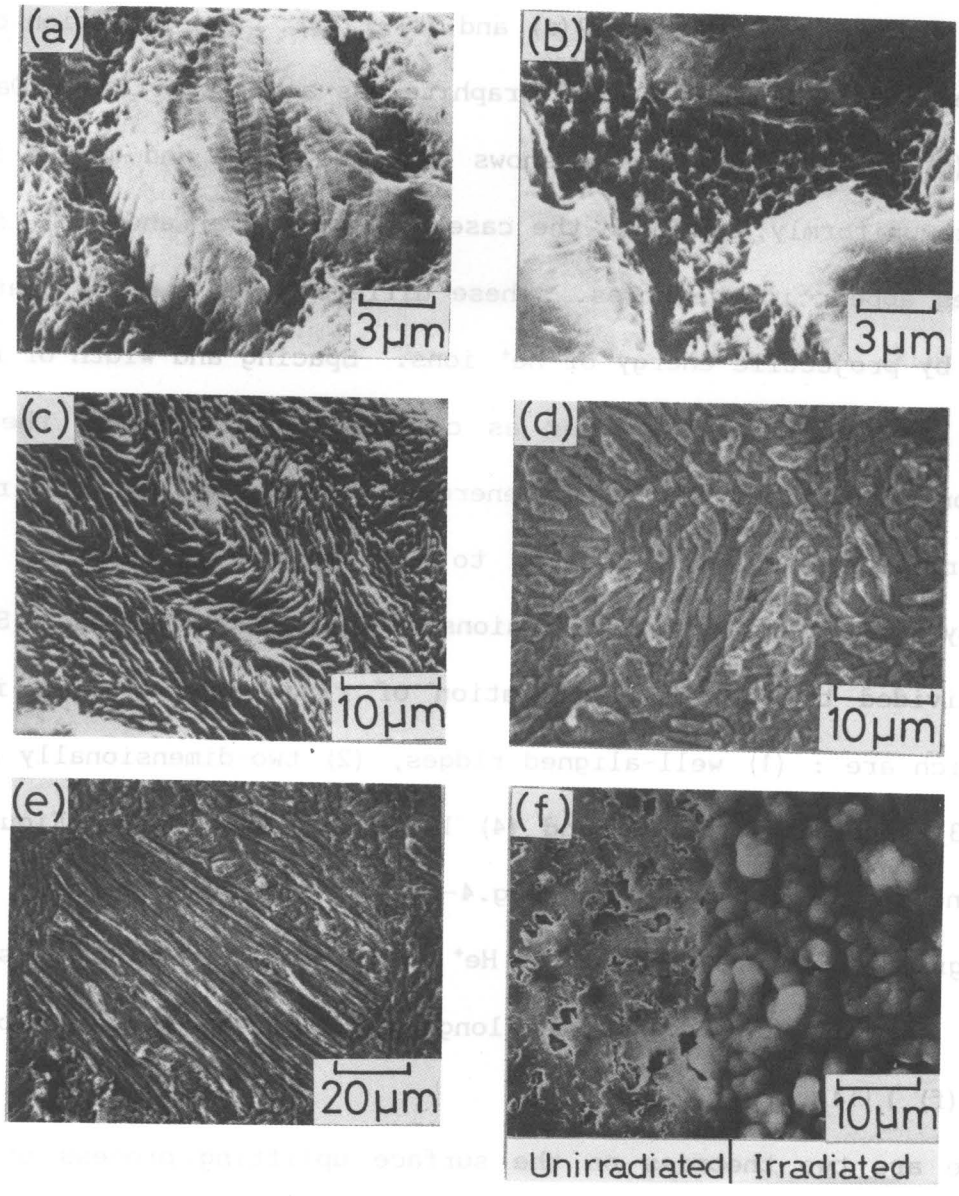

Fig. 4-2 Typical surface deformation of artificial graphite irradiated by He^+ ions.

ATJ graphite	(a), (b)	10 keV He^+	1.0×10^{19} ions/cm^2	[13]
	(c)	63 keV He^+	1.6×10^{18} ions/cm^2	[15]
Le Carbone 7477PT	(d), (e)	200 keV He^+	2.5×10^{18} ions/cm^2	[12]
POCO graphite	(f)	600 keV He^+	9.4×10^{18} ions/cm^2	[14]

ion irradiation.

3. Experimental

The graphite samples used in the present work were ISOGRAPH-88, POCO DFP-3-2, PAPYEX and GC-30. Prior to ion irradiation, these samples were mechanically polished with Al_2O_3 suspensions (ISOGRAPH-88 and POCO DFP-3-2) and diamond paste (GC-30). Then they were degassed at 1400℃ for an hour in a vacuum below 1×10^{-3} Pa. Ion irradiation was performed with 20 keV He^+ ions at normal incidence and at ambient temperature. Current density was below 2.0 mA/cm² during irradiation. Total ion doses ranged from 5.0×10^{16} ions/cm² to 2.0×10^{18} ions/cm². Following the ion irradiation, the surface topography of these graphite samples was examined with a SEM and a surface profilometer.

4. Results and discussion

4.1 Surface topography after irradiation

Figure 4-3 shows SEM micrographs and surface profiles of ISOGRAPH-88 after irradiation with 20 keV He^+ ions. The polished surface of the sample have many pores (Fig.4-3(a)). Significant surface deformation does not occur after ion irradiation to a dose of 1.0×10^{17} ions/cm², compared with the unirradiated surface. At a dose of 5.0×10^{17} ions/cm², the micrograph (Fig.4-3(c)) shows some protrusions. It can be clearly seen in Fig.4-3(d) that the irradiated area changes into significant rough surface and the surface is expanded outward. At a dose of 5.0×10^{18} ions/cm², the protrusions are developed to form many domed and conical upliftings on the whole surface. And the surface of irradiated area (Fig.4-3(f)) is much more expanded as compared with Fig.4-3(d). The step height of expanded area

can be estimated at approximately 0.2 μm. With a higher irradiation dose (2.0×10^{19} ions/cm^2), the domed upliftings become conical structure (Fig.4-3(g)). On the general surface features, however, the smoothing of the surface appears to be started around this irradiation dose. The tendency of smoothing can be also recognized from the decrease of the step height and the roughness value shown in Fig.4-3(h).

Figure 4-4 shows SEM micrographs and surface profiles of POCO DFP-3-2 after He^+ ion irradiation. Surface deformation did not occur by He^+ ion irradiation to a dose of 5.0×10^{16} ions/cm^2. Protrusions are observed on the surface after irradiation of 5.0×10^{17} ions/cm^2 (Fig.4-4(c)). These protrusions are developed to form many conical upliftings with the increase of irradiation dose. The roughness value rises with irradiation doses, though the value for ISOGRAPH-88 decreased at 2.0×10^{19} ions/cm^2 (Fig.4-3(h)). There are no significant difference on the surface deformation between ISOGRAPH-88 and POCO DFP-3-2 in contrast to the case of D_2^+ ion irradiation. This contrast suggests the dominant surface deformation processes differ between the D_2^+ ion irradiation and the He^+ ion irradiation.

Figure 4-5 shows typical SEM micrographs and a surface profile of PAPYEX. After 20 keV He^+ ion irradiation at 5.0×10^{18} ions/cm^2, a network of uplifting structure is observed (Fig.4-5(b)). At a lower magnification range ($\times$ 30), the macro-exfoliation can be observed (Fig.4-5(c)). As shown in Fig.4-5(d), the surface profile of the irradiated area also exhibits this exfoliation. The height of deformation extends to 30 μm, which is more than 10 times as much as the step height of ISOGRAPH-88 and POCO DFP-3-2. It can be concluded that the surface of PAPYEX was subjected to the heavy damage by He^+ ion irradiation to a dose of 5.0×10^{18} ions/cm^2. The similar surface features were observed for low magnified view

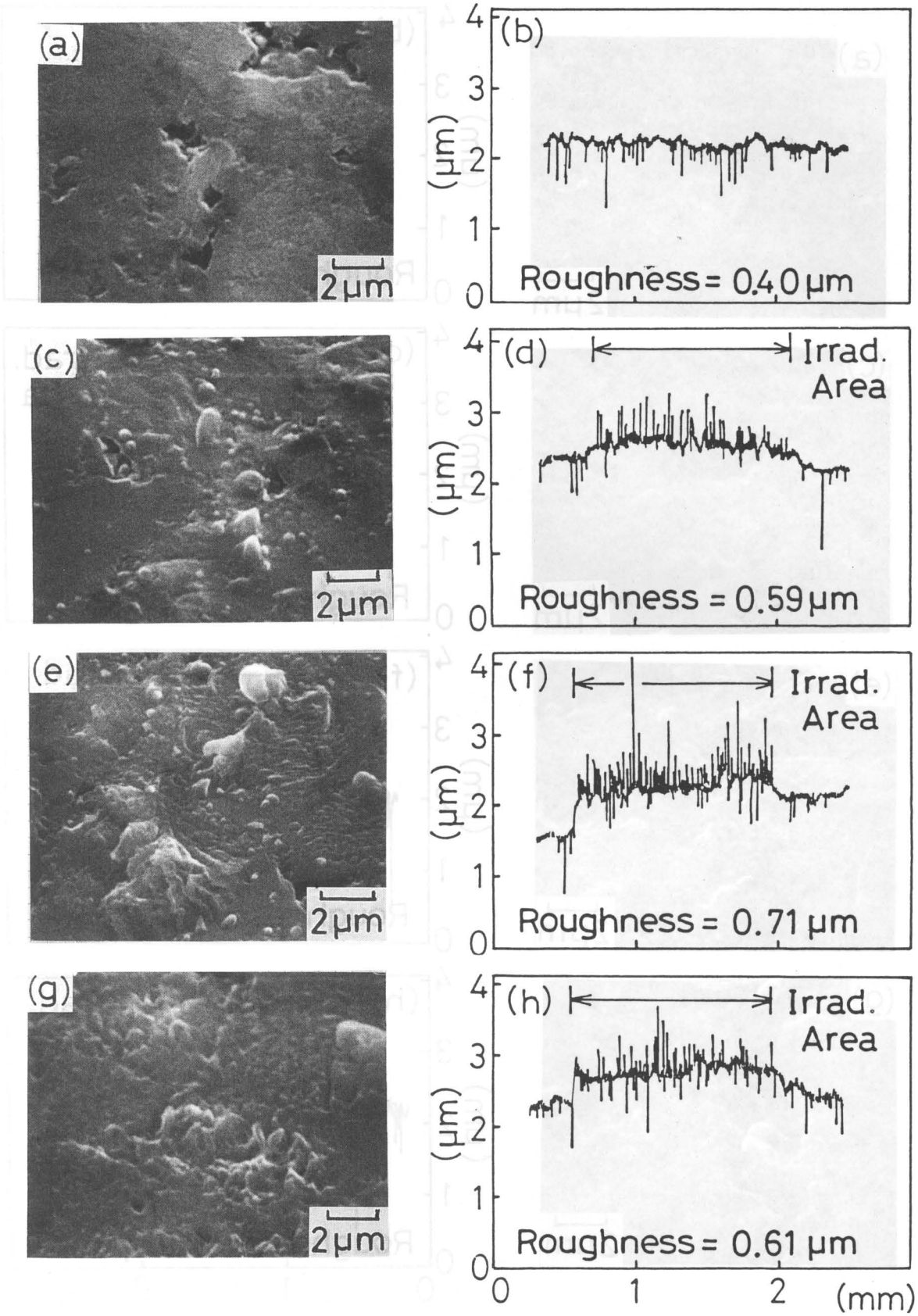

Fig. 4-3 SEM surface micrographs and surface profiles of ISOGRAPH-88 irradiated with 20 keV He^+ ions.

(a), (b) uniradiated
(c), (d) 5.0×10^{17} ions/cm^2
(e), (f) 5.0×10^{18} ions/cm^2
(g), (h) 2.0×10^{19} ions/cm^2

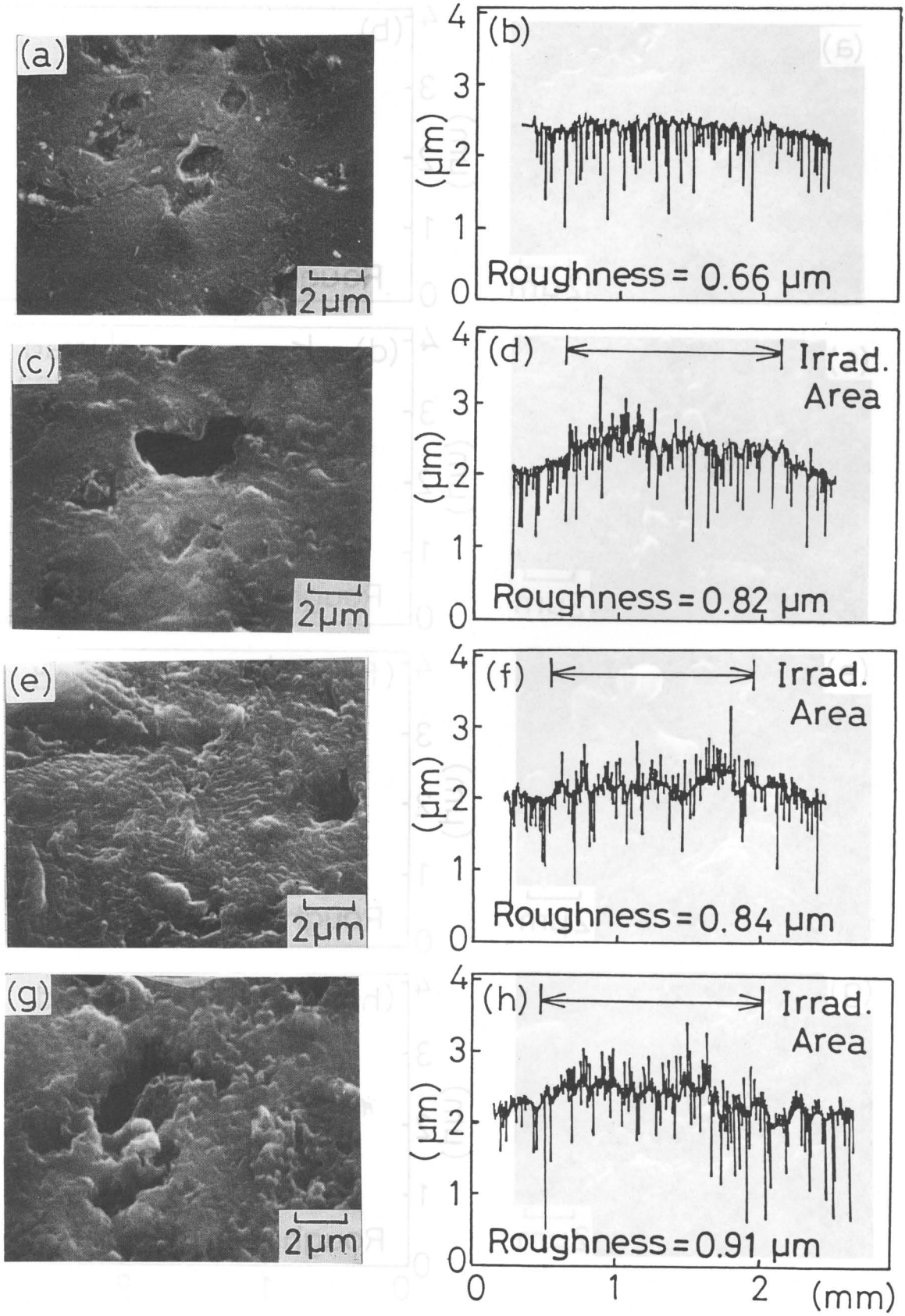

Fig. 4-4 SEM surface micrographs and surface profiles of POCO DFP-3-2 irradiated by 20 keV He^+ ions.

(a), (b) unirradiated
(c), (d) 5.0×10^{17} ions/cm²
(e), (f) 5.0×10^{18} ions/cm²
(g), (h) 2.0×10^{19} ions/cm²

of PAPYEX at further irradiation doses. However, microscopically, the surface showed rough features likely as shagreen. The typical rough surfaces were shown in Figs.4-5(e) and (f). The surface exhibits the range of sharp protrusions, and these protrusions are accompanied with several needles (Fig.4-5(f)). This surface structure can be frequently seen on the basal plane of graphite irradiated by He^+ ions (Figs.4-1(a) and (b)). It is consistent with the orientation of PAPYEX, whose surface faces

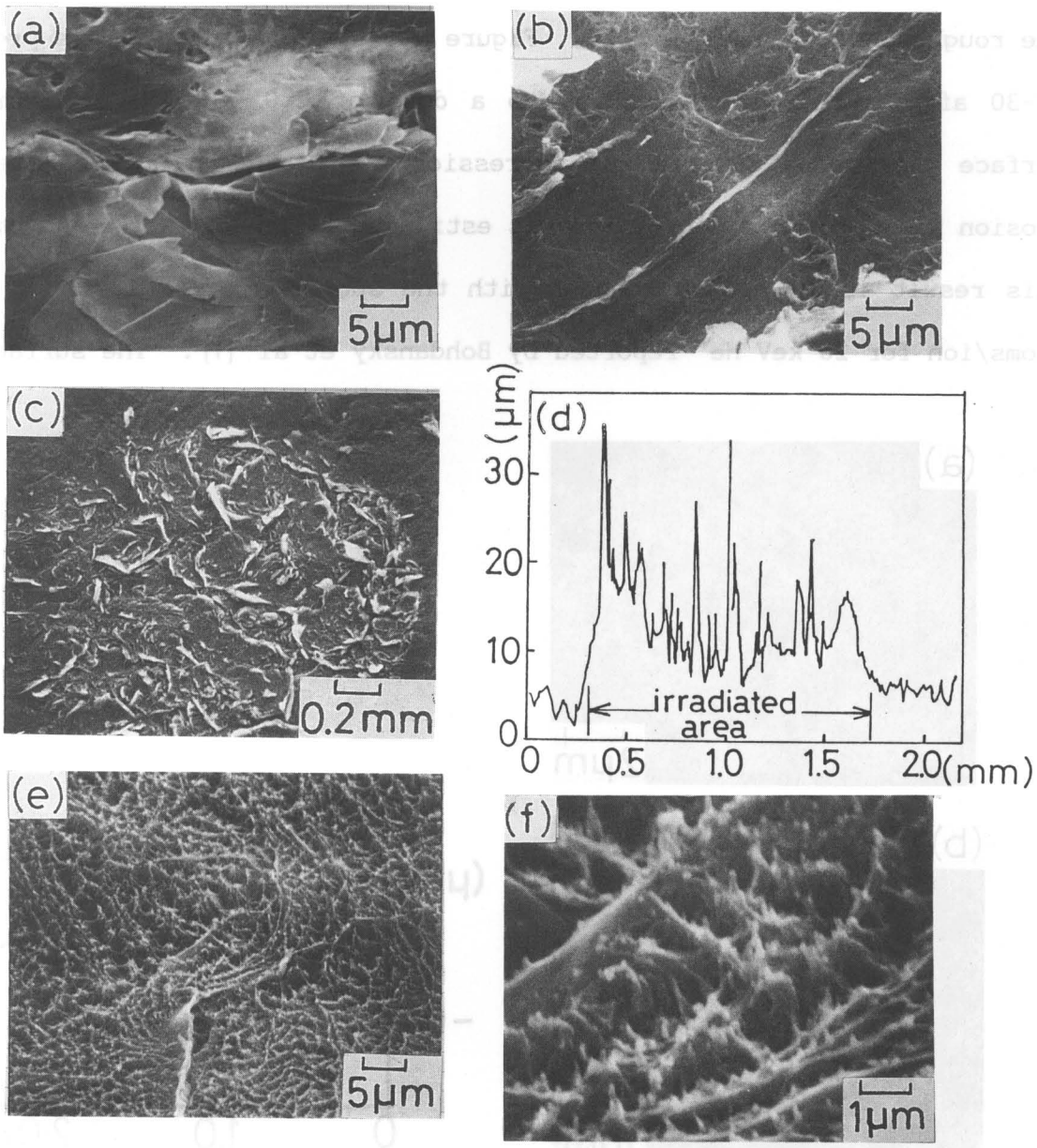

Fig. 4-5 SEM surface micrographs and a surface profile of PAPYEX irradiated by 20 keV He^+ ions.

(a) unirradiated (b), (c), (d) 5.0×10^{18} ions/cm²

(e), (f) 2.0×10^{19} ions/cm²

parallel to the basal plane as described in chapter Ⅱ.

Figure 4-6 shows the SEM micrographs and a surface profile of GC-30 after He^+ ion irradiation. The micrograph of glassy carbon after polishing with diamond paste shows the flat and smooth surface (Fig.4-6(a)). After irradiation to a dose of 1.0×10^{19} ions/cm², the surface gave to the rough features with many small dimples (Fig.4-6 (b)). As for the measurement of roughness value, no marked change could be determined, since the scale of the roughening is rather minute. Figure 4-6(c) shows the surface profile of GC-30 after He^+ ion irradiation to a dose of 2.0×10^{19} ions/cm². The surface was eroded to form the depression within the irradiated area. The erosion yield for the depression was estimated to be 4.3×10^{-2} atoms/ion. This result is in good agreement with the sputtering yield of $\sim 4 \times 10^{-2}$ atoms/ion for 20 keV He^+ reported by Bohdansky et al [1]. The surface

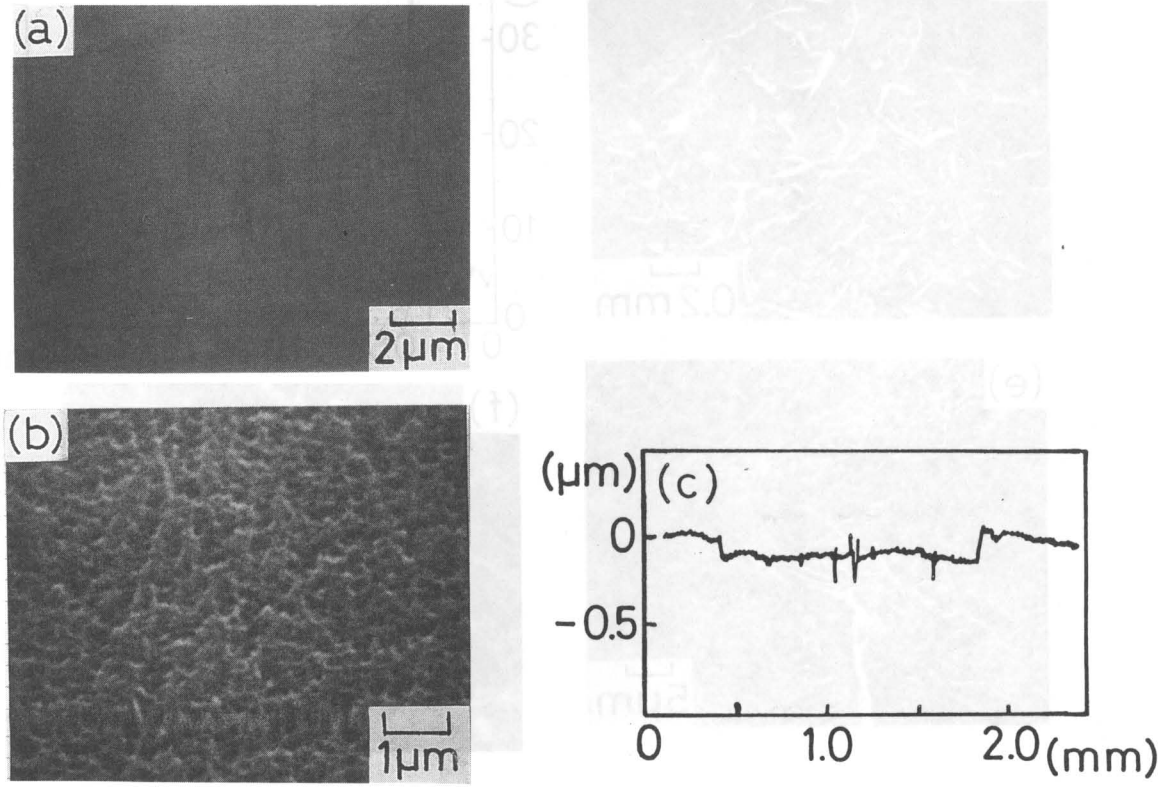

Fig. 4-6 SEM surface micrographs and a surface profile of GC-30 irradiated by 20 keV He^+ ions.
(a) unirradiated, (b) 1.0×10^{19} ions/cm², (c) 2.0×10^{19} ions/cm²

deformation of GC-30 by He^+ ion irradiation is different from that for D_2^+ ion irradiation (Fig.3-3). And the degree of deformation is much larger than that for D_2^+ ion irradiation.

4.2 Surface deformation process

To know the information of the deformation process, isochronal annealing tests up to 1000℃ were performed in a vacuum for the same samples whose surface was observed by SEM. Figure 4-7 is the typical results of annealing tests for ISOGRAPH-88 irradiated by He^+ ions. There is no evidence of clacks and flakes caused by gas bursts and blowing away of blister covers. This suggests that the surface deformation is not caused by the blister formation. The roughness values tend to decrease by 10-20 % after annealing up to 1000℃ in a vacuum. The step height of irradiated area does not change significantly. Figure 4-8 shows SEM micrographs and surface profiles of POCO DFP-3-2 after annealing tests. When the sample irradiated at 5.0×10^{17} ions/cm² was annealed up to 1000℃, the number of protrusions was increased and changed to uniform upliftings which were similar to the surface irradiated at a higher dose (Fig.4-8(a)). The roughness values, accordingly, are increased by thermal annealing (Fig.4-8(b), (d) and (f)). The change of surface before and after annealing tests may be explained by the release of residual stress in graphite. Namely, stress may be accumulated in the graphite lattice during irradiation, and transformed into the strain (upliftings and protrusions) during the subsequent thermal annealing. This mechanism is the same process to the deformation of graphite irradiated with D_2^+ ions, however, surface topography is entirely different from that for D_2^+ ion irradiation. Following items can be listed as the cause of the difference of topography change.

i) sputtering yield

ii) projected range

iii) displacements per atom (dpa)

iv) solubility and diffusivity

The difference of sputtering yield between D_2^+ and He^+ can not explain the variety of deformation at lower irradiation doses, where the sputtering erosion is below 0.5 nm. The projeced range of 20 keV D_2^+ for graphite is

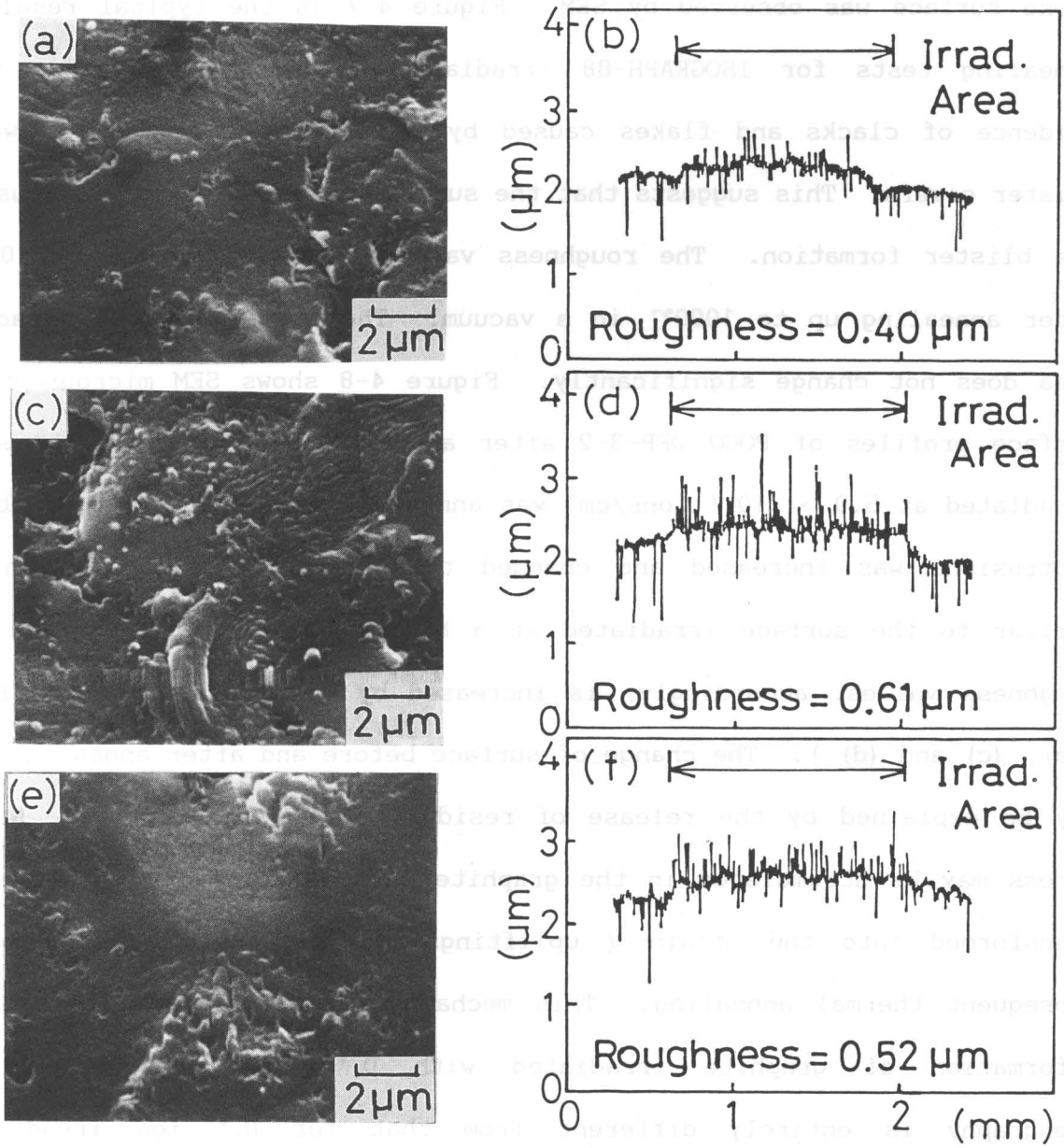

Fig. 4-7 SEM surface micrographs and surface profiles of irradiated ISOGRAPH-88 after annealing up to 1000℃.

(a), (b) 5.0×10^{17} ions/cm² (c), (d) 5.0×10^{18} ions/cm²

(e), (f) 2.0×10^{19} ions/cm²

almost equal to that of He^+ as described in Chapter V and VI. From the observations on the change of surface features with irradiation dose, the difference of dpa can not explain the variety of deformation, since the surface features of graphite irradiated by D_2^+ and He^+ are quite different among those for every dose. Thus, the cause of the difference may be attributed mainly to the variety of the solubility and diffusivity of deuterium and helium in graphite. This hypothesis may be supported by the

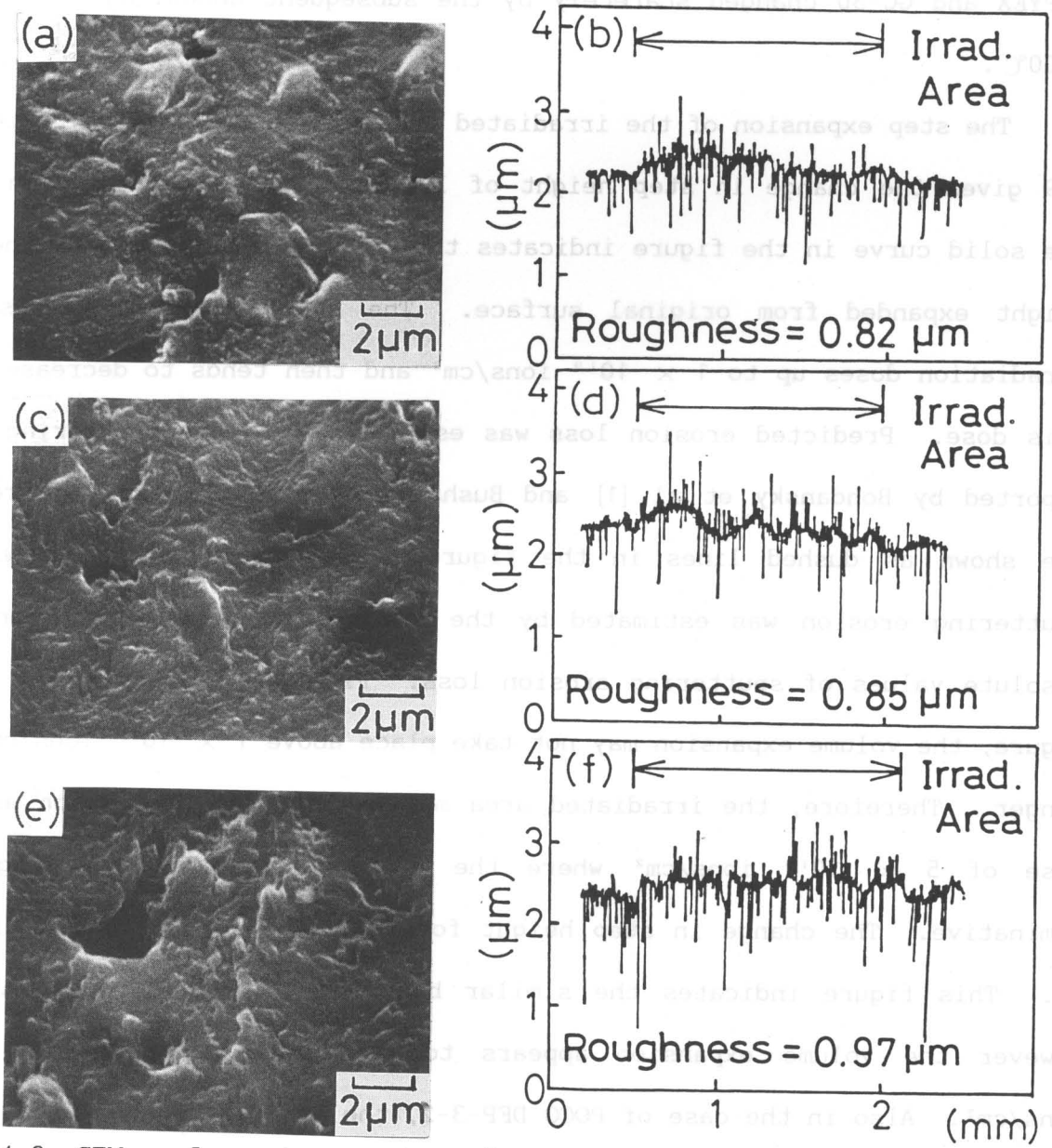

Fig. 4-8 SEM surface micrographs and surface profiles of irradiated POCO DFP-3-2 after annealing up to 1000℃.

(a), (b) 5.0×10^{17} ions/cm² (c), (d) 5.0×10^{18} ions/cm²

(e), (f) 2.0×10^{19} ions/cm²

shape of protrusions with domed or conical structure on the graphite irradiated with He^+ ions. It is reported that helium atoms implanted into graphite form the clusters of gas atoms [19]. For the reasons, the surface deformation of graphite irradiated by He^+ ions may be assisted by the bubble growth of helium gas. However, since diffusivity of helium in graphite is rather large as mentioned in Chapter Ⅵ, helium atoms in the bubble may migrate and spread before the development of blisters. The topography of PAPYEX and GC-30 changed scarecely by the subsequent annealing tests up to 1000℃.

The step expansion of the irradiated area has been discussed. Figure 4-9 gives the change in step height of ISOGRAPH-88 with irradiation dose. The solid curve in the figure indicates the experimental values of the step height expanded from original surface. The step height increases with irradiation doses up to 1×10^{19} ions/cm² and then tends to decrease above this dose. Predicted erosion loss was estimated from the sputtering yield reported by Bohdansky et al.[1] and Busharov et al [10]. And the results are shown as dushed lines in the figure. Net volume expansion without sputtering erosion was estimated by the sum of the step heights and the absolute values of sputtering erosion loss. From the results shown in the figure, the volume expansion may not take place above 1×10^{19} ions/cm² any longer. Therefore, the irradiated area may exhibit the depression above a dose of 5×10^{19} ions/cm² where the erosion loss will be large and dominative. The change in step height for POCO DFP-3-2 is shown in Fig.4-10. This figure indicates the similar behavior to that for ISOGRAPH-88, however the volume expansion appears to still remain above 1×10^{19} ions/cm². Also in the case of POCO DFP-3-2, the irradiated area may exhibit the depression above 5×10^{19} ions/cm². From the results described above, isotropic graphite will expand outward due to the stress accumulation and/or

the bubble growth of helium gas during He^+ ion irradiation. Above a dose of 1.0×10^{19} ions/cm², the decrease of step height and smoothening took place since the sputtering erosion would be predominant on the deformation of graphite surface at higher doses.

PAPYEX suffered the heavy damage on surface even at lower irradiation doses, and the change in step height could be hardly identified. As shown in Fig.4-5, PAPYEX has not much durability against the He^+ ion irradiation. The heavy damage on PAPYEX may be caused by the singularity of the structure. PAPYEX consists of the stacks of graphite lamella and has the strong orientation to the basal plane. Since the migration rate of gas atoms is generally low along the direction normal to the basal plane, the partial exfoliation may be occurred to release the helium gas from the bubbles accumulated between the lamella during He^+ ion irradiation. This model may be supported by the helium retention behavior of PAPYEX, which shows the large retention of helium below 5×10^{17} ions/cm² and the drastic decrease of helium retention

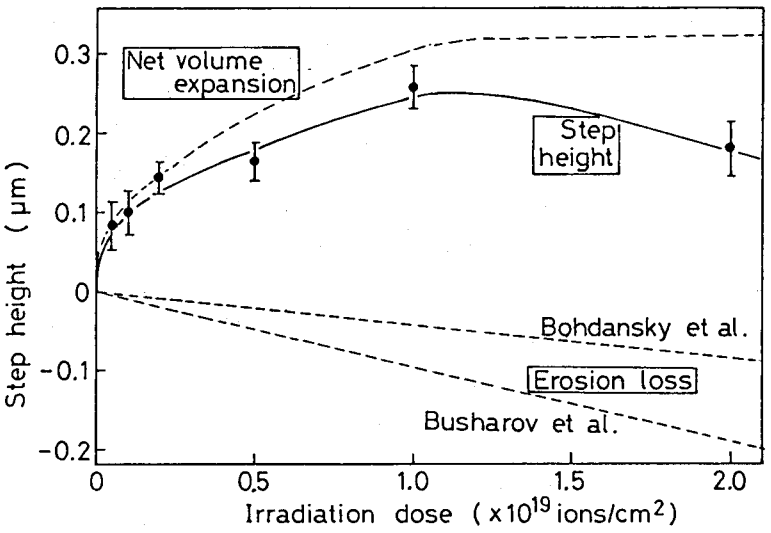

Fig. 4-9 Change in step height of ISOGRAPH-88 with irradiation dose.

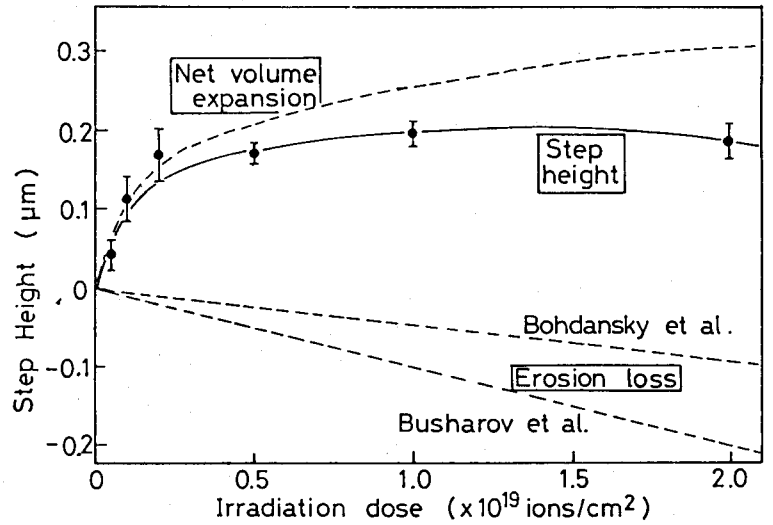

Fig. 4-10 Change in step height of POCO DFP-3-2 with irradiation dose.

above this dose, as will be mentioned in Chapter Ⅵ.

Figure 4-11 shows the change in step height of GC-30 with irradiation dose. Surface uplifting did not practically observed in contrast with the case of isotropic graphite. Erosion loss estimated from the surface depression corresponds well with the sputtering data reported by Bohdansky et al [1]. Thus, the surface deformation of GC-30 by He^+ ion irradiation should be dominated only by the sputtering erosion. This may be caused by the following two reasons.

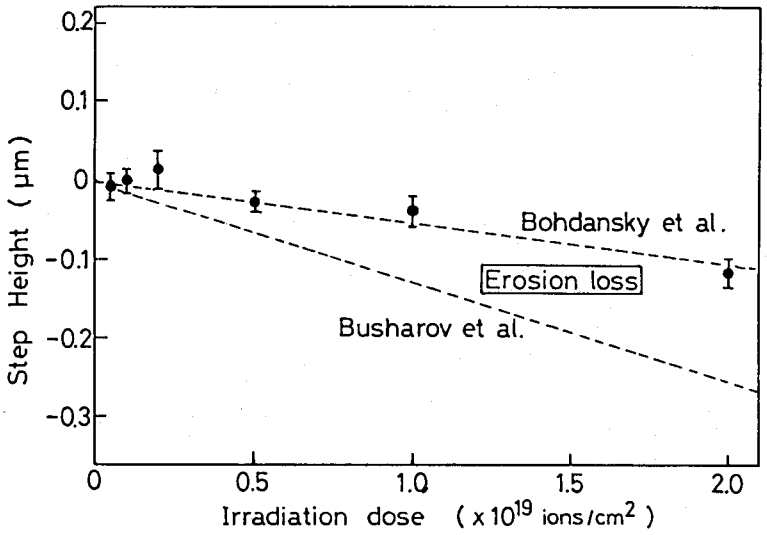

Fig. 4-11 Change in step height of GC-30 with irradiation dose.

i) Glassy carbon does not grow or expand in a specific direction due to the random structure, while the isotropic graphite shows the large deformation.

ii) Glassy carbon has a low helium retention as described later in Chapter Ⅵ. It may not lead to develop the helium gas bubbles which are the origin of the large deformation.

GC-30 can be recognized to have the highest durability against the surface erosion by He^+ ion irradiation among the four samples studied in the present work.

5. Concluding remarks

Surface erosion of various types of carbon by 20 keV He^+ ions has been observed. The main results of this study can be summarized as follows :

(1) The surface deformation of the four samples is different from that for

D_2^+ ion irradiation. Considerably large deformation was observed on the surface of ISOGRAPH-88, POCO DFP-3-2 and PAPYEX.

(2) The surface deformation may be assisted by the bubble growth of helium gas during He^+ ion irradiation.

(3) The surface of isotropic graphite (ISOGRAPH-88 and POCO DFP-3-2) exhibits the volume expansion in the irradiated area. And the decrease of step height and smoothening take place above a dose of 1.0×10^{19} ions/cm^2 due to the sputtering erosion.

(4) PAPYEX was subjected to the heavy damage with many exfoliation by He^+ ion irradiation.

(5) GC-30 shows little change in surface features without surface upliftings. This may be caused by the microscopical isotropy of the structure and the low helium retention in glassy carbon.

(6) GC-30 has the highest durability against the He^+ ion irradiation. And PAPYEX shows the worst durability among four types of carbon.

References

[1] J.Bohdansky, H.L.Bay and W.Ottenberger, J.Nucl.Mater. 76/77 (1978) 163.

[2] R.Behrisch, J.Bohdansky, G.H.Oetjen, J.Roth, G.Schilling and H.Verbeek, J.Nucl.Mater. 60 (1976) 321.

[3] J.Roth, J.Bohdansky, W.Poschenrieder and M.K.Sinha, J.Nucl.Mater. 63 (1976) 222.

[4] G.J.Thomas, W.Bauer, P.L.Mattern and B.Granoff, "Radiation Effects on Solid Surfaces" (M.Kaminsky ed., American Chemical Society, Washington D.C., 1976), p.97.

[5] S.Veprek, A.P.Webb, H.R.Oswald and H.Stuessi, J.Nucl.Mater. 68 (1977)

32.

[6] Y.Kazumata, J.Nucl.Mater. 68 (1977) 257.

[7] K.Sone, T.Abe, K.Obara, R.Yamada and H.Ohtsuka, J.Nucl.Mater. 71 (1977) 82.

[8] S.Vepřek, A.Portmann, A.P.Webb and H.Stuessi, Radiat.Effects 34 (1977) 183.

[9] K.Sone, M.Saidoh, T.Abe, R.Yamada, K.Obara, H.Ohtsuka and Y.Murakami, in: "Proc. 7th International Vacuum Congress and 3rd International Conference on Solid Surfaces, Vol.1", Vienna, Austria, Sep. 1977 (1977) p.375.

[10] N.P.Busharov, V.M.Gusev, M.I.Guseva, Yu.L.Krasuliu, Yu.V.Martynenko, S.V.Mirnov and I.A.Rozina, Sov.Atomic Energy 42 (1977) 554.

[11] K.Obara, T.Abe, K.Sone, R.Yamada and H.Ohtsuka, Sinkuu 20 (1977) 176 (in Japanese).

[12] M.Saidoh, R.Yamada and K.Nakamura, J.Nucl.Mater. 102 (1981) 97.

[13] B.Navinsek, Fusion Technol. 6 (1984) 491.

[14] L.H.Rovner and K.Y.Chen, J.Nucl.Mater. 63 (1976) 307.

[15] S.K.Das, M.Kaminsky, R.Tishler and J.Cecchi, J.Nucl.Mater. 85/86 (1979) 225.

[16] H.Atsumi, S.Yamanaka, P.Son and M.Miyake, J.Nucl.Mater. 133/134 (1985) 268.

[17] H.Atsumi, S.Tokura, T.Yamauchi, S.Yamanaka and M.Miyake, J.Nucl.Mater. 141-143 (1986) 258.

[18] J.B.Roberto, "Physical Sputtering of Candidate Plasma-side Materials for FED/INTOR", ORNL/TM-8593 (1983).

[19] K.Niwase, M.Sugimoto, T.Tanabe and F.E.Fujita, J.Nucl.Mater. 155-157 (1988) 303.

Ⅴ Thermal Desorption of D_2 and CD_4 from Graphite Irradiated by D_2^+ Ions

1. Introduction

It has been regarded as the important matter to know the behavior of hydrogen in graphite, since the graphite becomes to be frequently applied to the inner walls (liners, limiters, etc.) of fusion experimental reactors. However, it will not be suitable to apply the graphite to the first walls if the tritium inventory or the formation of hydrocarbon is considerably high under a certain condition. From this point of view, there are numerous studies concerning the hydrogen recycling on graphite [1]. It is worthy of notice that these studies concentrate especially on the thermal desorption behavior of hydrogen isotopes implanted into graphite [2-9]. Ashida et al. [5-9,13] have reported the thermal desorption behavior and its mechanisms of deuterium and tritium implanted into pyrolytic graphite at 5 keV. However, thermal desorption of hydrogen isotopes may be different among the types of graphite and various projectile energy.

In Chapter Ⅲ, the surface erosion of different types of graphite by 20 keV D_2^+ ion irradiation has been studied. In this chapter, thermal desorption of deuterium (D_2) and deutero-methane (CD_4) from different types of graphite irradiated with 20 keV D_2^+ ions has been studied paying attention to the difference of the graphite structure.

2. Experimental

The samples used in this study were two types of isotropic graphite (ISOGRAPH-88 and POCO DFP-3-2), exfoliated recompressed graphite (PAPYEX) and glassy carbon (GC-30). Their fundamental properties are given in Table 2-1, 2-3 and 2-4. Prior to ion irradiation, these samples were given a fine mechanical polish, though the PAPYEX sample was not polished. Then

they were annealed at 1100℃ for 2 hours in a vacuum below 1×10^{-3} Pa. Ion irradiation was performed with 20 keV D_2^+ ions at normal incidence and at ambient temperature. Current density was kept up to 0.5 mA/cm² during irradiation. Total ion doses ranged from 5.0×10^{16} ions/cm² to 5.0×10^{18} ions/cm². Thermal desorption measurements of D_2 and CD_4 from the irradiated graphite were carried out with the apparatus displayed in Fig.5-1. The samples were heated at a constant heating rate of 10℃/min in a vacuum below 10^{-6} Pa. D_2 and CD_4 released from a graphite sample were identified with a quadrupole mass spectrometer.

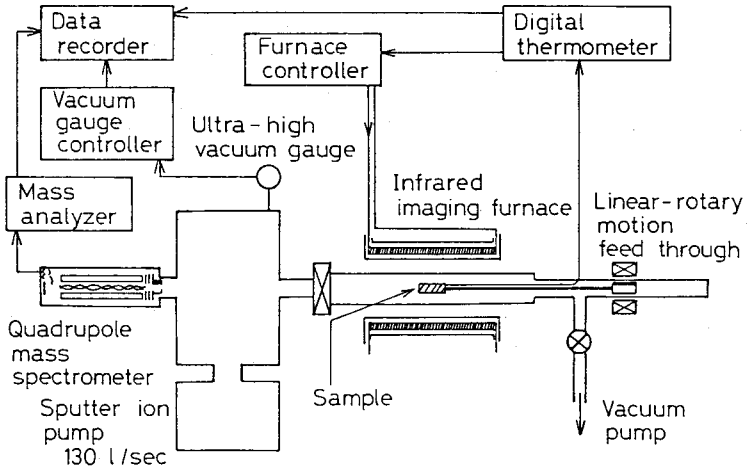

Fig. 5-1 Schematic diagram of the apparatus for thermal desorption measurement.

3. Results and discussion

3.1 Thermal desorption measurements

Figure 5-2 shows the thermal desorption curves of D_2 from ISOGRAPH-88 irradiated with D_2^+ ions at various doses. It is clearly seen in the figure that the amount of released deuterium increases with irradiation dose. This figure exhibits relatively broad desorption curves which appear to consist of three peaks at approximately 600℃, 750℃ and 800℃. It can be seen on the desorption curves from the graphite samples irradiated at 5.0×10^{16} and 5.0×10^{18} ions/cm². These peaks are termed peak Ⅰ, Ⅱ and Ⅲ in sequence from the peak at the lowest temperature, respectively. The mutual

ratio of each peak height is quite different for the experimental conditions. In Fig.5-2, peak I shows the highest peak among the three. The occurrence of three peaks suggests the presence of, at least, three different sites of deuterium in carbon or three different chemical bonds between carbon and deuterium. The thermal desorption spectra having three peaks is in agreement with the desorption results obtained by Ashida et al. [6,7,8].

Figure 5-3 shows the thermal desorption curves of CD_4 from ISOGRAPH-88 irradiated with D_2^+ ions at various doses. The amount of released CD_4 increases with irradiation dose similarly to the deuterium desorption. Each CD_4 desorption curve shows relatively narrow and single peak at approximately 520 - 550℃. These results correspond well with the data for different types of graphite obtained by several authors [2,5,6,13]. No marked desorption of CD_4 was detected (see Chapter Ⅶ) for the graphite sample exposed to D_2 gas atmosphere

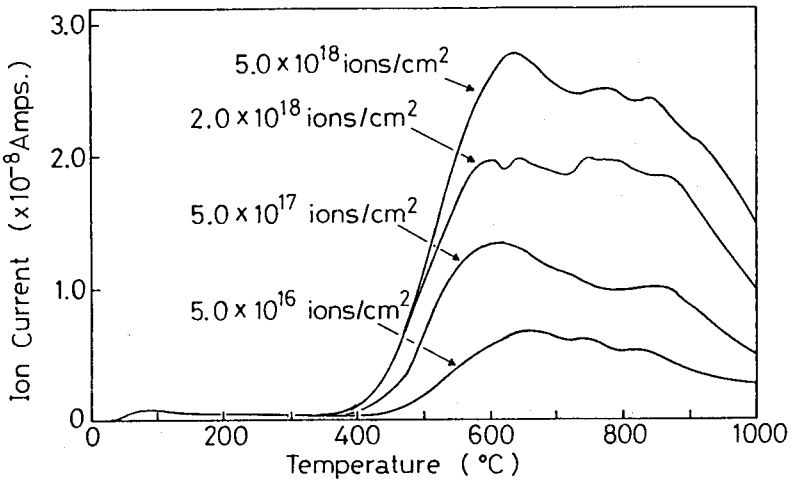

Fig. 5-2 Thermal desorption curves of D_2 from ISOGRAPH-88 irradiated with 20 keV D_2^+ ions to various doses (beam diameter : 8 mm).

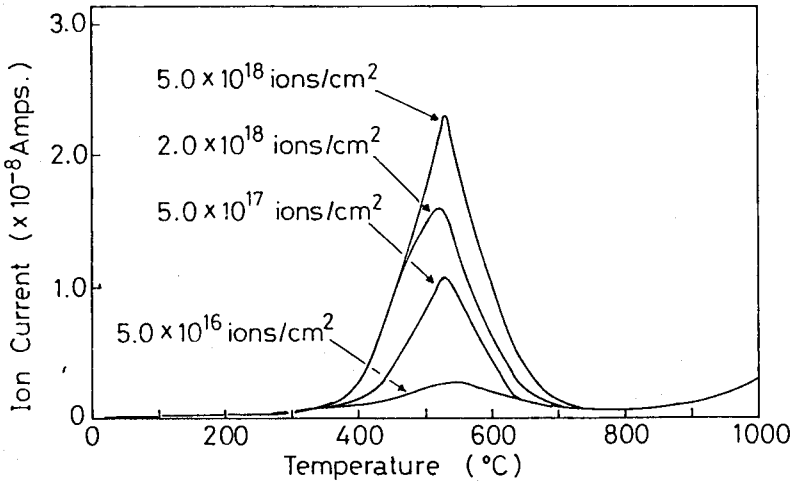

Fig. 5-3 Thermal desorption curves of CD_4 from ISOGRAPH-88 irradiated with 20 keV D_2^+ ions to various doses (beam diameter : 8 mm).

at elevated temperatures. The CD_4 desorption from the graphite irradiated with D_2^+ ions suggests that there exist strong chemical interactions between deuterium ions and carbon atoms in bombarded graphite. Figure 5-4 gives the total amounts of D_2 and CD_4 released from ISOGRAPH-88 as a function of the irradiation dose in a logarithmic scale. Langley et al. [2] have been reported that the trapping efficiency of deuterium kept at approximately 100% below 1.0×10^{18} ions/cm² and decreased continually with increasing fluence above this dose. General agreement can be found between the present results and trapping behavior obtained by Langley et al. Figure 5-5 shows the thermal desorption curves of D_2 and CD_4 from four types of carbon samples irradiated with D_2^+ ions to a dose of 2.0×10^{18} ions/cm². Deuterium desorption curves of the four have relatively broad peaks at around 750℃, and deutero-methane curves have peaks at about 550℃. In this case, peak Ⅱ appears to be the highest peak for these deuterium desorption curves. Not only desorption curves of D_2 and CD_4, but also cumulative amounts of released species are similar for each sample, therefore, thermal desorption of D_2 and CD_4 released from graphite may be independent of the structure of the materials, in contrast with the desorption of helium implanted into various types of graphite (Figs. 6-1, 6-2, 6-3, 6-4 and 6-6). Namely, thermal desorption of D_2 and CD_4 may take place mainly through the detrapping process and/or the recombination process of

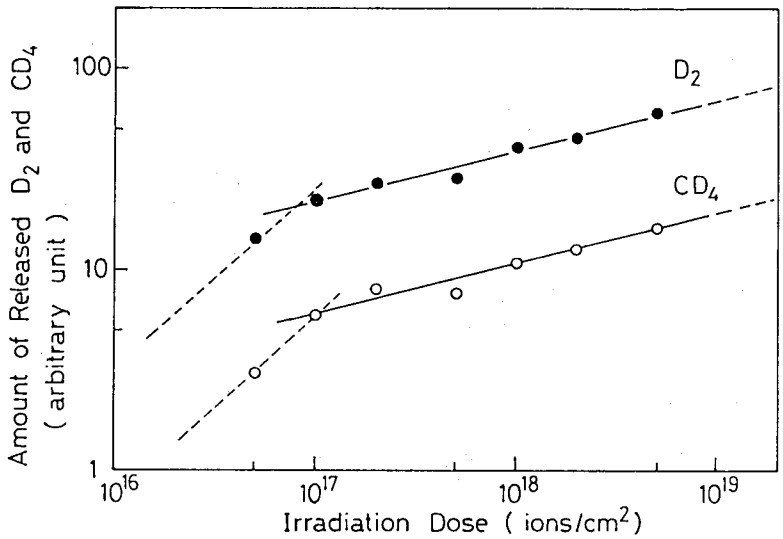

Fig. 5-4 Change in amount of D_2 and CD_4 released from ISOGRAPH-88 with irradiation dose.

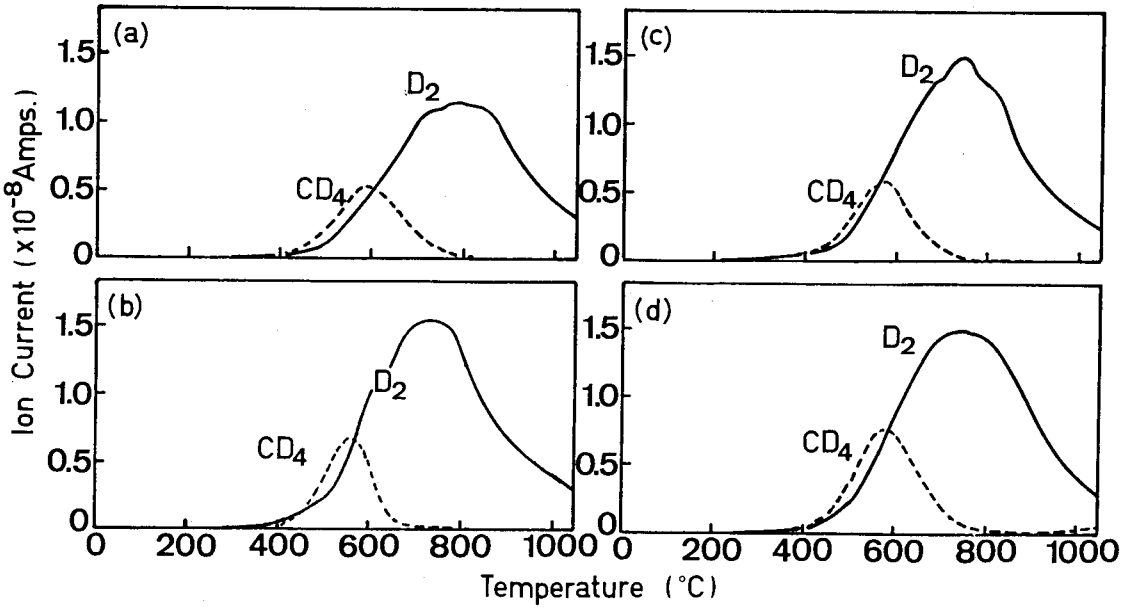

Fig. 5-5 Thermal desorption curves of D_2 and CD_4 from various types of carbon irradiated with 20 keV D_2^+ ions to a dose of 2.0×10^{18} ions/cm² (beam diameter : 5 mm).

(a) POCO DFP-3-2 (c) PAPYEX

(b) ISOGRAPH-88 (d) GC-30

deuterium and deutero-methane chemically trapped in the graphite, as proposed by Ashida et al. [6,7,8].

3.2 Desorption mechanism

Desorption mechanism of D_2 and CD_4 has been discussed on pyrolytic carbon irradiated with 5 keV D^+ ions by Ashida et al [6,7,8]. They have reported the presence of three peaks (peaks Ⅰ, Ⅱ and Ⅲ) in the H_2 and D_2 desorption curve. It is believed that the hydrogen and deuterium desorption for peaks Ⅰ and Ⅱ occur due to the second order reaction (e.g. recombination-controlled process) in the surface, because the peak temperature shifts to lower temperature with increasing hydrogen fluence [6-9,12]. PeakⅢ, which is observed at the highest temperature, seems to be controlled by diffusion process [9], however the diffusion coefficient of deuterium in graphite has not been studied enough. Diffusion of deuterium

in graphite has been estimated and discussed in Chapter Ⅶ of this thesis. Thereupon, the mechanism of deuterium desorption is discussed on peaks Ⅱ and Ⅲ in this section, since the peak Ⅰ can not be distinguished from the desorption curves obtained in the present conditions. The shift of peak temperature with irradiation dose has been also observed for peak Ⅱ of D_2 desorption in this study. The following methods are usually applied to evaluate the desorption mechanism (cf. Appendix):

i) curve fitting with computer-generated curves

ii) analyzing the peak shift by varying the heating rate

iii) analyzing the desorption curve obtained by step heating

In this chapter, method ii) was used to determine the parameters of the desorption controlled by detrapping and recombination. Figure 5-6 shows the peak temperature shift by varying the heating rate. The frequency factor and activation energy for recombination-controlled process were determined, and

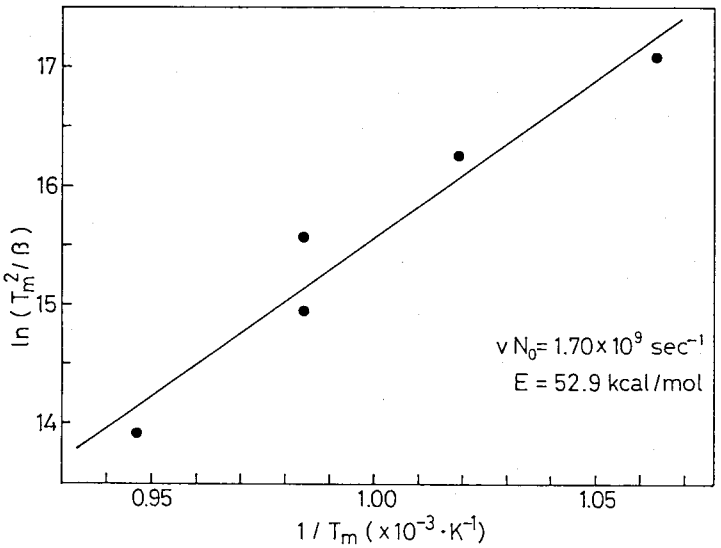

Fig. 5-6 Change in peak temperature of D_2 desorption with heating rate (Tm: peak temperature (K), β: heating rate (K/sec)).

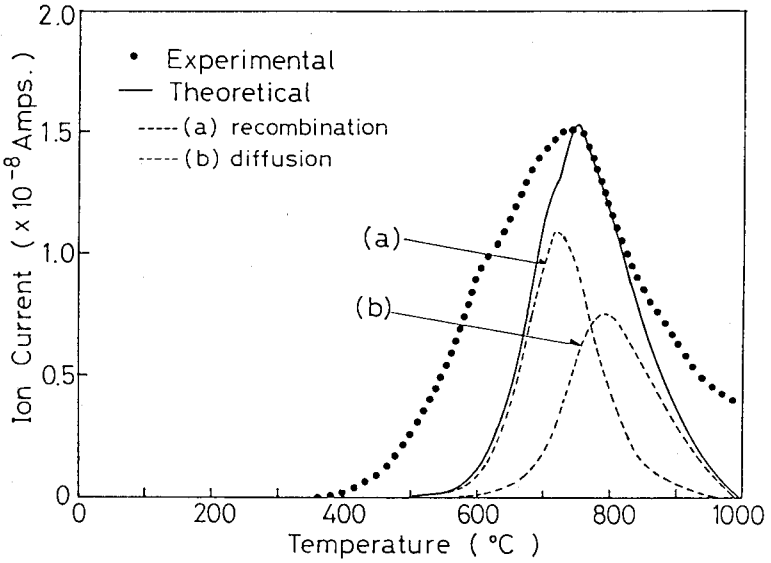

Fig. 5-7 Thermal desorption curve of D_2 derived from recombination and diffusion analysis.

the desorption rate can be expressed by :

$-dN/dt\,(atoms/sec) = 1.7\times 10^{9}\,(sec^{-1})\ N^{2}(t)/N_{0}\ \exp[-52.9\,(kcal/mol)/RT]$ --(1)

(cf. Fig.5-6). Here, for Fig.5-6, ν is the preexponential factor for desorption of second order (sec^{-1}), N_0 is the initial fractional surface coverage and E is the activation energy for recombination. The activation energy roughly agrees with the value of 59 kcal/mol reported by Ashida et al.[7]. Thermal desorption curve was calculated by means of the present data (see Appendix) and drawn in Fig.5-7. This peak is consistent with the temperature of a maximum of the experimental desorption curve.

Diffusion coefficient of D_2 in graphite can be described as the following equation :

$D\ (cm^{2}/sec) = 1.69\ \exp[-60\,(kcal/mol)/RT]$ ---------- (2) ,

according to the analysis discussed in Chapter Ⅶ. Thermal desorption curve for diffusion-controlled process was calculated with the diffusion data and mean projected range of 150 nm [15], using the finite difference equations given in Appendix of this thesis. The result derived from the computation are shown as curve (b) in Fig.5-7. Broad desorption curves of deuterium may be well expressed by the sum of the three desorption curves for each fundamental process though the curve for peak Ⅰ is not analyzed. The start of diffusional release appears to be later than the desorption controlled by recombination process. Deuterium atoms for peaks Ⅰ and Ⅱ may be situated at the surfaces or the boundary of graphite grains where the bulk diffusion can not be effective, since the diffusional release, which is the earlier stage of desorption (see Fig.9-1), does not controlled the whole process of deuterium desorption.

The analysis on the CD_4 desorption from ISOGRAPH-88 has been performed with the same technique. It is believed that the deutero-methane desorption occurs due to the first order reaction (detrapping), because the peak

temperature does not shift with increasing deuterium fluence [6]. Desorption parameters were determined from the peak shift by varying the heating rate. The results of the desorption tests are given in Fig.5-8. The frequency factor and activation energy for detrapping process were estimated, and the desorption rate becomes

$$-dN/dt\,(\text{atoms/sec}) = 4.01 \times 10^{12}\,(\text{sec}^{-1})\; N(t)\; \exp[-56.1\,(\text{kcal/mol})/RT] \quad -- \quad (3)$$

This value of activation energy is considerably large as compared with 38 kcal/mol reported by Ashida et al. [6]. Thermal desorption curve calculated with the data is shown as curve (b) in Fig.5-9. Curve (a) is the desorption curve assumed the recombination-controlled process. Curve (a) with broad shape is closer to the experimental results rather than curve (b). However, the shape of desorption curve appears to be first-ordered desorption (detrapping-controlled) with steeper slope on the side of

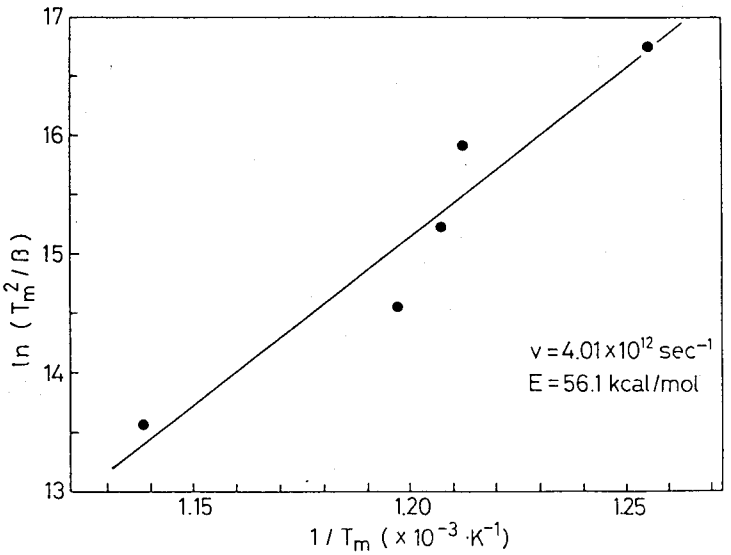

Fig. 5-8 Change in peak temperature of CD_4 desorption with heating rate (Tm: peak temperature (K), β: heating rate (K/sec)).

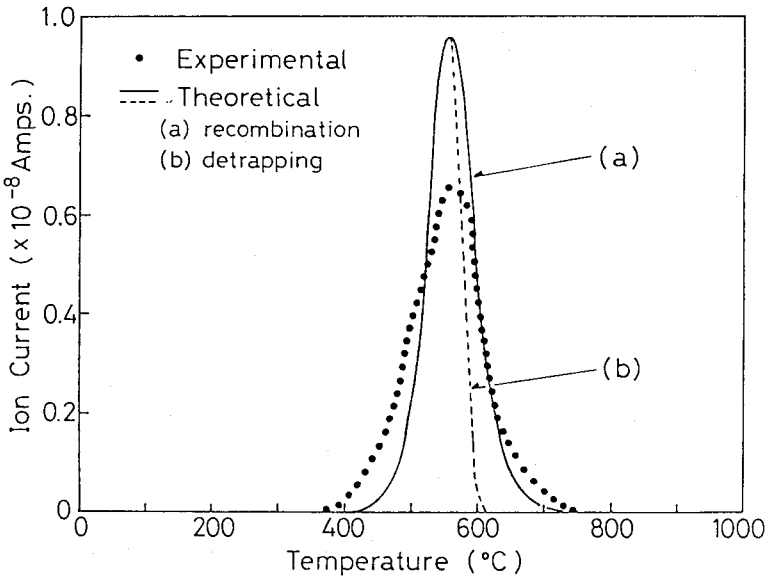

Fig. 5-9 Thermal desorption curve of CD_4 derived from detrap and recombination analysis.

higher temperatures while second-order desorption (recombination-controlled) is approximately symmetrical (cf. Figs.9-2 (a) and (b)). Further measurements under various conditions and the considerations of evaluation technique should be necessary to discuss the release mechanism and parameters of CD_4 desorption more accurately.

4. Concluding remarks

In this chapter, thermal desorption behavior of D_2 and CD_4 from graphite irradiated with 20 keV D_2^+ ions has been studied. The results obtained in this study are summarized as follows :

(1) Thermal desorption curves of D_2 and CD_4 are similar among the four types of carbon, and thermal desorption of D_2 and CD_4 should be irrespective of the structure of the sample.

(2) Deuterium desorption curves on graphite irradiated by D_2^+ ions appear to have three peaks at approximately 600℃ (peakⅠ), 750℃ (peakⅡ) and 800℃ (peakⅢ). Peaks Ⅱ and Ⅲ may be attributed to recombination-controlled desorption and diffusional release, respectively. These desorption behavior can be expressed by the equations :

recombination (peakⅡ)

$$-\frac{dN(t)}{dt}\ (\text{atoms/sec}) = 1.7\times 10^{9}\ (\text{sec}^{-1})\ \frac{N^2(t)}{N_0}\ \exp\left(-\frac{52.9\ (\text{kcal/mol})}{RT}\right)$$

diffusion (peakⅢ)

$$D\ (\text{cm}^2/\text{sec}) = 1.69\ \exp\left(-\frac{60\ (\text{kcal/mol})}{RT}\right)$$

(3) The start of diffusional release appears to be later than the recombination-controlled process. Deuterium atoms for peaks Ⅰ and Ⅱ may be situated at the surfaces or the boundary of graphite grains where the bulk diffusion can not be effective.

(4) Deutero-methane desorption curves on graphite are attributable to detrapping-controlled process, and expressed by the equation :

$$-\frac{dN(t)}{dt}\ (\text{atoms/sec}) = 4.01\times 10^{12}\ (\text{sec}^{-1})\ N(t)\ \exp\left(-\frac{56.1\ (\text{kcal/mol})}{RT}\right)$$

References

[1] K.L.Wilson and W.L.Hsu, J.Nucl.Mater. 145-147 (1987) 121.

[2] R.A.Langley, R.S.Blewer and J.Roth, J.Nucl.Mater. 76/77 (1978) 313.

[3] S.T.Picraux and W.R.Wampler, J.Nucl.Mater. 93/94 (1980) 853.

[4] B.M.U.Scherzer, R.A.Langley, W.Möller, J.Roth and R.Schulz, Nucl. Instrum.Meth. 194 (1982) 497.

[5] K.Ashida, K.Ichimura, M.Matsuyama, H.Miyake and K.Watanabe, J.Nucl. Matar. 111/112 (1982) 769.

[6] K.Ashida, K.Ichimura, M.Matsuyama and K.Watanabe, J.Nucl.Mater. 128/129 (1984) 792.

[7] K.Ashida and K.Watanabe, Annual Report of Tritium Research Center, Toyama University, Japan 5 (1985) 31 (in Japanese).

[8] K.Watanabe and K.Ashida, Annual Report of Tritium Research Center, Toyama University, Japan 5 (1985) 41 (in Japanese).

[9] K.Ashida, M.Matsuyama and K.Watanabe, Annual Report of Tritium Research Center, Toyama University, Japan 6 (1986) 83.

[10] H.Atsumi, S.Tokura, S.Yamanaka, M.Nunogaki and M.Miyake, J.Nucl.Mater. 141-143 (1986) 113.

[11] V.Philipps, E.Vietzke, M.Erdweg and K.Flaskamp, J.Nucl.Mater. 145-147 (1987) 292.

[12] K.Nakayama, S.Fukuda, T.Hino and T.Yamashina, J.Nucl.Mater. 145-147 (1987) 301.

[13] K.Ashida, K.Ichimura, M.Matsuyama and K.Watanabe, J.Nucl.Mater. 148

(1987) 217.

[14] S.K.Erents, C.M.Braganza and G.M.McCracken, J.Nucl.Mater. 63 (1976) 399.

[15] H.H.Andersen and J.F.Ziegler, Stopping Powers and Ranges in All Elements Vol.3 Hydrogen (Pergamon Press, New York, 1977) p.59.

Ⅵ Thermal Desorption of Helium from Graphite Irradiated by He^+ Ions

1. Introduction

Surface erosion by D_2^+ ion irradiation and thermal desorption of deuterium were studied in Chapters Ⅲ and Ⅴ of this thesis. However, little research has been performed on thermal desorption measurements of helium implanted into graphite [1-4] (refs.3 and 4 are the papers by the author.), although the first wall will be heavily irradiated by energetic He^+ ions as the product of D-T fusion reaction. Furthermore, release mechanism of helium from graphite has not been made clear. On the other hand, wall conditioning to reduce the tritium inventory in graphite has been recently carried out by helium plasma discharge [5,6]. For the above reasons, it is important to study the thermal desorption behavior of helium implanted into graphite.

In this chapter, thermal desorption of helium implanted into various types of graphite has been studied.

2. Experimental

POCO DFP-3-2, ISOGRAPH-88, PAPYEX and GC-30 were used as the samples in this work. Before ion irradiation, these samples were mechanically polished and degassed at 1400℃ for one hour in a vacuum below 10^{-3} Pa. Ion irradiation was performed at ambient temperatures with a 20 keV He^+ ion beam (3 mm diameter) at a flux of approximately 1×10^{15} ions/cm^2 · sec. Total irradiation doses ranged from 2.0×10^{16} ions/cm^2 to 2.0×10^{18} ions/cm^2. Thermal desorption measurements of helium from the irradiated samples were made with the apparatus shown in Fig.5-1, and the heating of the sample was carried out isochronally mainly at a heating rate of 10℃/min in a vacuum below 10^{-5} Pa. Heating rates were varied from 2 to 50℃/min to evaluate the

value of activation energy for helium desorption. Released helium was identified with a calibrated quadrupole mass spectrometer.

3. Results and discussion

3.1 Thermal desorption measurements

In Fig.6-1, the results of thermal desorption measurements, which were carried out at a constant heating rate of 10℃/min, are shown for the POCO graphite irradiated with He^+ ions at various doses. Helium desorption from the graphite samples irradiated at 5.0×10^{16} ions/cm² starts at about 80℃, and the curve has a maximum at approximately 170℃. With a dose of 1.0×10^{17} ions/cm² the helium desorption curve peaked at 220℃, being higher than the dose of 5.0×10^{16} ions/cm². No helium desorption occurred above 400℃ from the sample irradiated at such lower doses (Fig.6-1(a)). The peak temperature rises to approximately 260℃ for the graphite sample irradiated at 3.0×10^{17} ions/cm². These desorption curves exhibit the tendency to

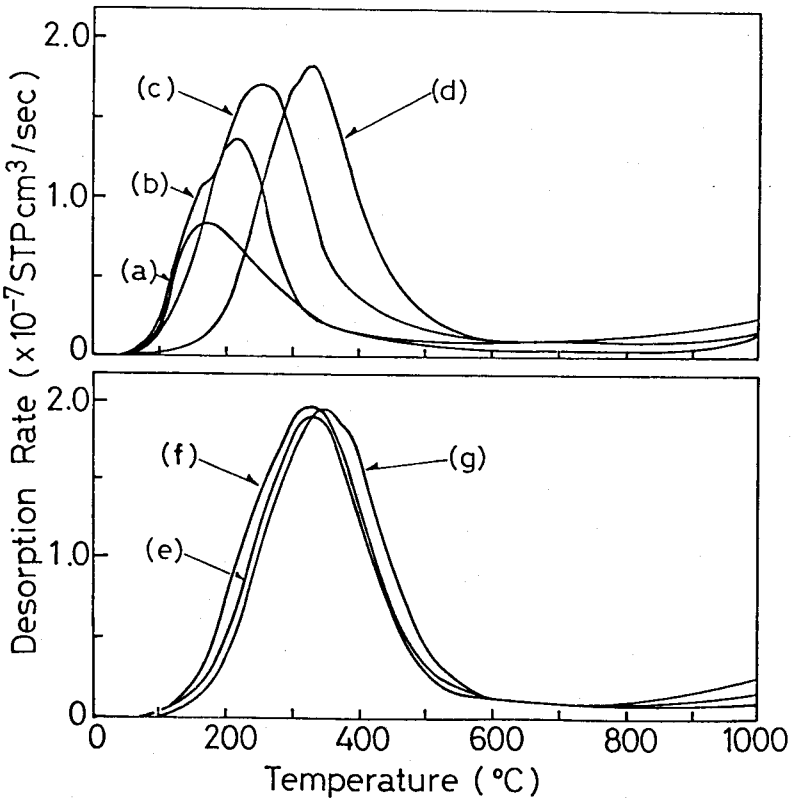

Fig. 6-1 Thermal desorption curves of helium from POCO DFP-3-2 irradiated with 20 keV He^+ ions at various doses (Heating rate : 10℃/min).
(a) 5.0×10^{16} ions/cm², (b) 1.0×10^{17} ions/cm²
(c) 3.0×10^{17} ions/cm², (d) 5.0×10^{17} ions/cm²
(e) 7.0×10^{17} ions/cm², (f) 1.0×10^{18} ions/cm²
(g) 2.0×10^{18} ions/cm²

shift toward higher temperature with irradiation dose up to 7.0×10^{17} ions/cm^2. At higher irradiation doses (above 1.0×10^{18} ions/cm^2), the desorption curves display nearly identical shapes and the peak temperature becomes constant at approximately 330℃.

Möller et al.[2] have reported the thermal desorption curves for edge-oriented pyrolytic graphite irradiated with 8 keV ^{3}He ions at doses of 4.5×10^{15} ions/cm^2 and 4.5×10^{17} ions/cm^2. The peak temperature reported by them is approximately 120℃ lower than that obtained in the present work at the same irradiation dose. The difference is quite large when the high heating rate of 2℃/sec in the study by Möller et al. is taken into account. And it is attributable to the sorts of graphite and/or the ion energy. Langley et al.[1] have examined the retention of helium, implanted with 8 keV He^+ ions into prism plane oriented graphite at doses of 5.0×10^{17} ions/cm^2 and 1.0×10^{18} ions/cm^2, and reported that almost all of implanted helium was released by post annealing at 200℃. However, in the case of POCO graphite studied here, only a few percent of retained helium will be released by the annealing up to 200℃, except for that of lower doses. As mentioned above, thermal desorption curves vary with the sorts of graphite and the ion energy, therefore, thermal desorption measurements have been carried out on various types of graphite in order to explore the

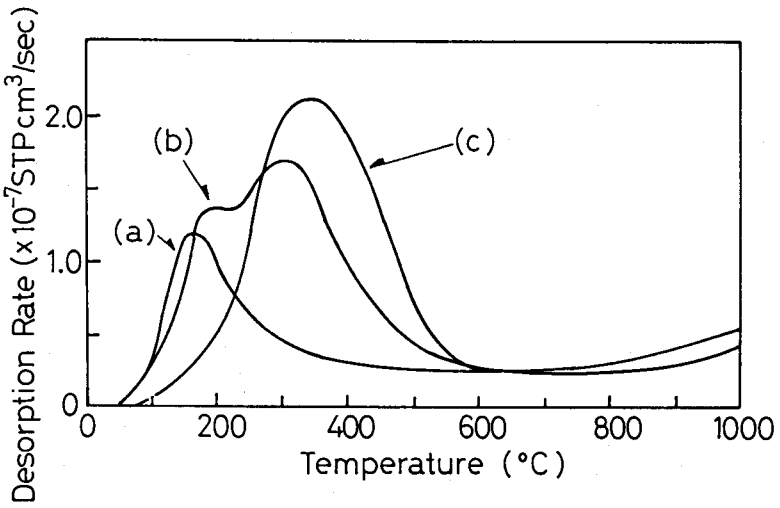

Fig. 6-2 Thermal desorption curves of helium from ISOGRAPH-88 irradiated with 20 keV He^+ ions at various doses (Heating rate : 10℃/min).
(a) 1.0×10^{17} ions/cm^2, (b) 1.0×10^{18} ions/cm^2 (c) 2.0×10^{18} ions/cm^2

difference of thermal desorption behavior among each sample.

In Fig.6-2, thermal desorption curves of helium are shown for ISOGRAPH-88 irradiated to various doses. In this case, the peak height of the desorption curve increases as the irradiation dose is raised from 1.0×10^{17} to 2.0×10^{18} ions/cm^2. Helium desorption of ISOGRAPH-88 irradiated at 1.0×10^{18} ions/cm^2 shows the broad desorption curve and two peaks (Fig.6-2 (b)). Two distinct peaks (approximately 200℃ and 300℃) appearing on the desorption curve for 1.0×10^{18} ions/cm^2 were also observed on the curve for a dose of 7.0×10^{17} ions/cm^2. Above a dose of 1.5×10^{18} ions/cm^2, a single peak was observed and the shapes of the desorption curves were almost identical to those of POCO graphite.

Figure 6-3 shows the

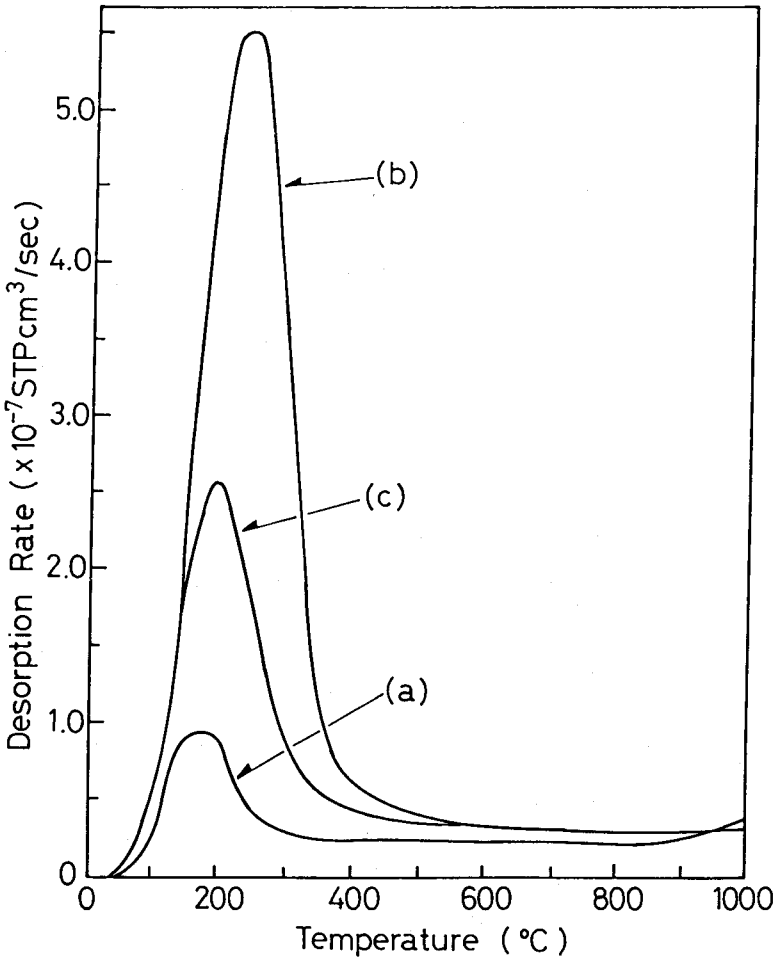

Fig. 6-3 Thermal desorption curves of helium from PAPYEX irradiated with 20 keV He$^+$ ions at various doses (Heating rate:10℃/min).
(a) 1.0×10^{17} ions/cm^2, (b) 5.0×10^{17} ions/cm^2
(c) 1.0×10^{18} ions/cm^2

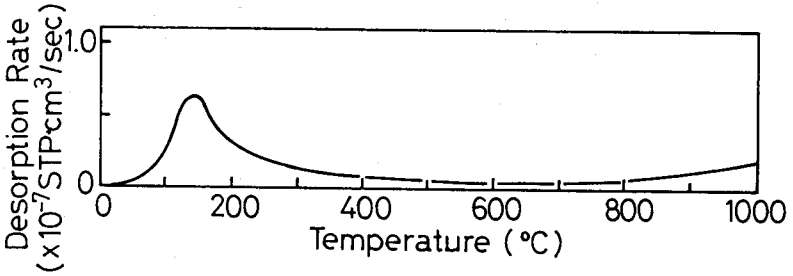

Fig. 6-4 Thermal desorption curve of helium from GC-30 irradiated with 20 keV He$^+$ ions at a dose of 5.0×10^{17} ions/cm^2 (Heating rate : 10℃/min).

desorption curves of helium for irradiated PAPYEX samples which have not studied before. The highest peak of these desorption curves occurred at 5.0 × 10^{17} ions/cm² of irradiation dose. Above 1.0 × 10^{18} ions/cm², no change in shape of the desorption curves was observed and the peak height was reduced to half that of 5.0 × 10^{17} ions/cm². Figure 6-4 shows the desorption curve of helium from GC-30 irradiated at a dose of 5.0 × 10^{17} ions/cm². The peak height for the curve of GC-30 is much lower than that of other samples. The peak temperature is very low and situated at approximately 140℃.

Changes in peak temperature of the desorption curves for irradiated graphite samples are shown in Fig.6-5 as a function of irradiation dose. Changes in peak temperature for POCO graphite samples are similar to that of ISOGRAPH-88. That is, the peak temperature rises

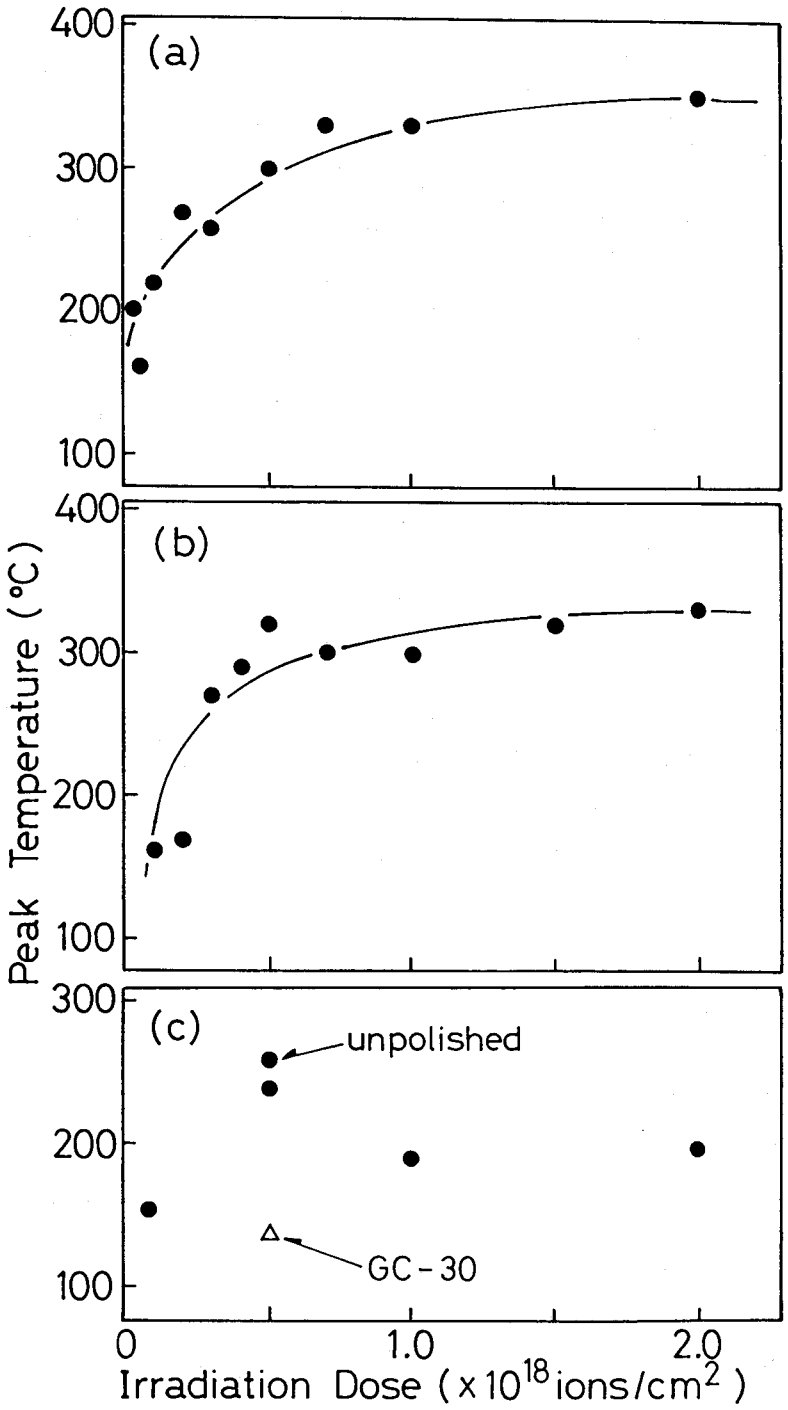

Fig. 6-5 Change in peak temperature with irradiation dose.
(a) POCO DFP-3-2 , (b) ISOGRAPH-88 , (c) PAPYEX (●) and GC-30 (△)

with irradiation doses of up to 5.0 × 10^{17} ions/cm² whereas higher doses tend to stabilize at approximately 330℃. As for PAPYEX, peak temperatures of the desorption curves are at approximately 200℃ above doses of 1.0 × 10^{18} ions/cm². These results were obtained for polished PAPYEX samples except for the point indicated by an arrow. Peak temperatures of PAPYEX are considerably lower than those for isotropic graphite (POCO DFP-3-2 and ISOGRAPH-88). It can be recognized that the helium in PAPYEX is easy to release at relatively low temperatures. GC-30 shows a lower peak temperature even than that for PAPYEX (Fig.6-5 (c)).

Figure 6-6 shows the total amount of helium released from graphite samples. The amount of released helium increases with the irradiation dose in both isotropic graphites, but released helium from ISOGRAPH-88 samples is slightly less than that from POCO DFP-3-2 below a dose of 1.0 × 10^{18} ions/cm².

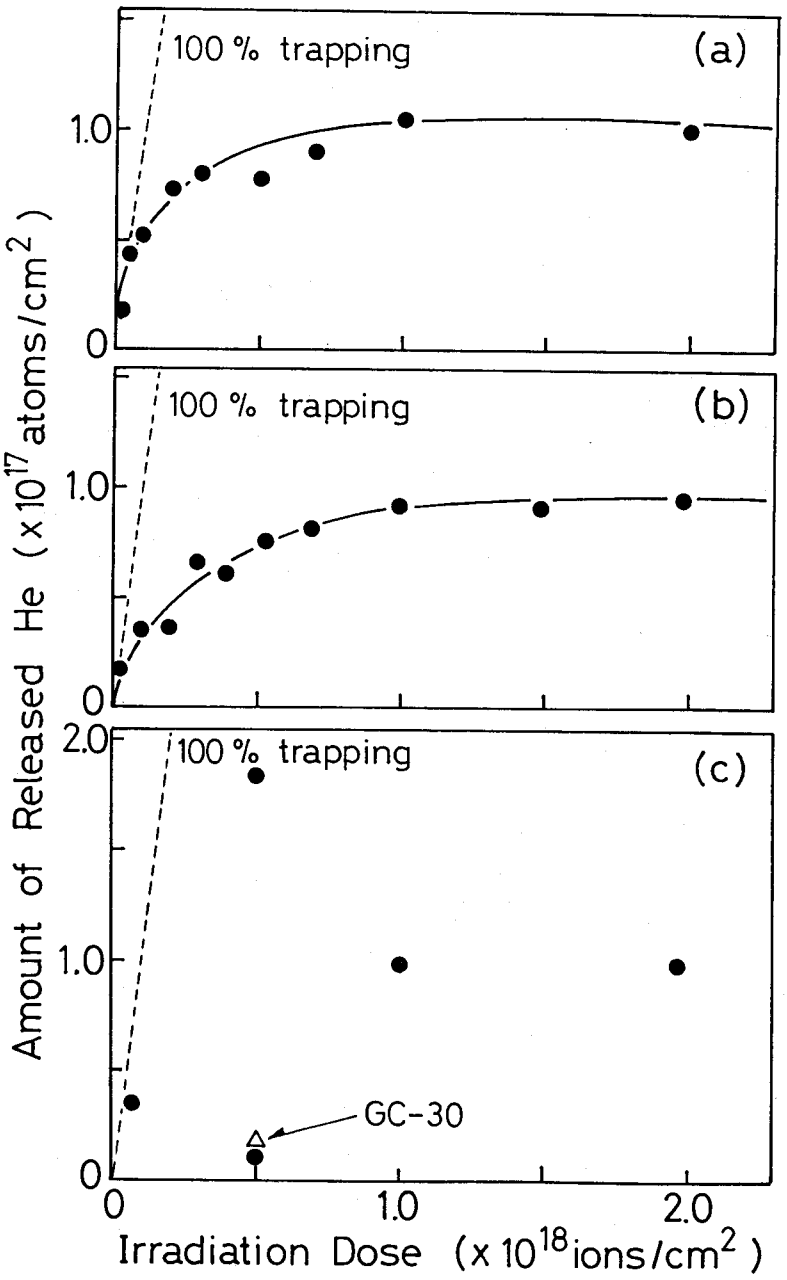

Fig. 6-6 Change in amount of released helium with irradiation dose.
(a) POCO DFP-3-2 , (b) ISOGRAPH-88 ,
(c) PAPYEX(●) and GC-30(△)

Above a dose of 1.0×10^{18} ions/cm^2, the amount of released helium from each graphite sample no longer increases. The saturation dose of helium retention appears to be about 1.0×10^{18} ions/cm^2 in the present work. This value is in agreement with those reported for pyrolytic graphite irradiated with 8 keV He^+ [1,2]. Saidoh et al.[7] have also reported similar saturation at a dose of 8.2×10^{17} ions/cm^2 through the re-emission measurement on isotropic graphite (Le Carbone 7477 PT) irradiated with 200 keV He^+ ions. These saturation doses should be consistent within experimental error, even though the saturation dose tends to shift upward with increasing the helium ion energy in the same way as the case of deuterium ion irradiation[8]. PAPYEX shows the distinctive change in total amount of released helium at approximately 5.0×10^{17} ions/cm^2. The total amount of helium released from polished PAPYEX is approximately twice as much as the amount for isotropic graphites at the same irradiation dose, on the other hand, unpolished PAPYEX retain only 12 % of the helium retention of isotropic graphite. Stangeby et al.[9] have also reported the low retention of deuterium in PAPYEX which may be caused by the release of deuterium from the inner surface of PAPYEX. Implanted helium in graphite will be distributed widely around the projected range (~ 0.2 μm [10]), as reported by Möller et al.[2]. However, PAPYEX consists of layers of graphite lamella (~ 0.1 μm) and is suffered the macro-exfoliation due to He^+ ion irradiation above a dose of 5.0×10^{17} ions/cm^2, as mentioned in Chapter Ⅳ. Thus, the significant change of released amount of helium from PAPYEX between 5.0×10^{17} ions/cm^2 and 1.0×10^{18} ions/cm^2 may be attributed to the helium gas release due to macro-exfoliation. This hypothesis is probably supported by the difference of helium retention between two PAPYEX samples irradiated at 5.0×10^{17} ions/cm^2. The polished PAPYEX retained a large amount of helium (Fig.6-6(c)) and was not suffered

the heavy damage by the He^+ ion irradiation at this dose, though the unpolished PAPYEX retained only a little amount of helium (Fig.6-6(c)) and was suffered the macro-exfoliation. Thus, the surface condition appears to directly affect the amount of helium retention.

As shown in Fig.6-6 (c), GC-30 retains only 22 % of the helium retention of isotropic graphite. Glassy carbon has a network structure which consists of condensed aromatic ribbon molecules (Fig.2-2), and has small pores with diameter of 5-10 nm within the network [11]. Interstitial helium atoms implanted into graphite can easily diffuse especially along the basal plane in the graphite lattice; namely, some of the helium will release into the pores before trapping will occur at defects in the lattice. Furthermore, these helium atoms in the pore might migrate easily from the projected range (~ 0.2 μm [10]) to the surface. Little helium retention in glassy carbon is consistent with the results obtained in the re-emission measurements by Saidoh et al. [7].

3.2 Desorption mechanism

Helium atoms implanted into graphite behave as interstitial atoms which can readily diffuse in graphite even at $T \lesssim 180$℃ [12]. And these interstitial atoms can nucleate and form interstitial dislocation loops at temperatures below 500℃. These dislocation loops will develop with increasing

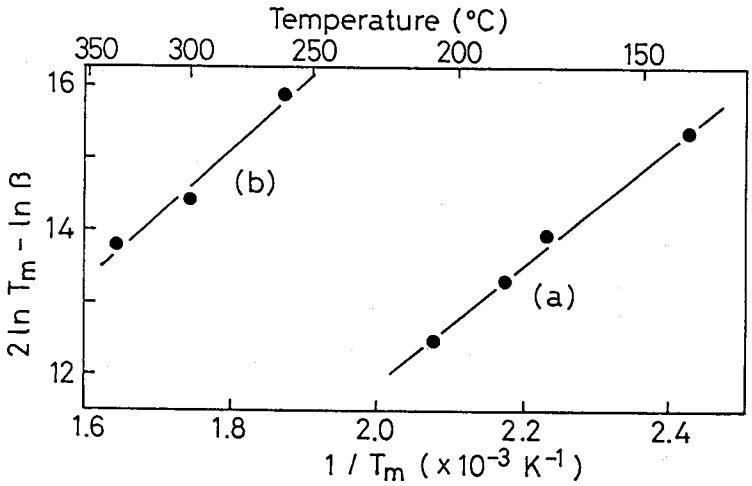

Fig. 6-7 Change in peak temperature of helium desorption with heating rate (Tm : peak temperature (K) , ß : Heating rate (K/sec))
(a) 5.0×10^{16} ions/cm^2,
(b) 5.0×10^{17} ions/cm^2

helium ion irradiation. On the other hand, thermal desorption of helium is believed to be controlled by detrapping process [2]. Thus, assuming that the concentration and binding energy of trapping sites for helium increase with the development of dislocation loops, it makes peak temperature shift upward. When the nucleation and development of dislocation loops are saturated, the peak temperature should not rise and the amount of trapped helium should increase no longer. Then, assuming the simple first-ordered process for the rate determining step of helium desorption, the activation energy (Ed) for thermal desorption of helium was determined from the peak shift of the desorption curves for POCO graphite samples by means of varying the heating rate (analysis method is given in Appendix). The results are shown in Fig.6-7 and Table 6-1. Ed values increase with the irradiation dose, namely

Table 6-1 Ed for helium desorption from irradiated POCO DFP-3-2.

Irradiation dose (ions/cm²)	Activation energy Ed (kcal/mol)
2.0×10^{16}	13.8
5.0×10^{16}	16.8
5.0×10^{17}	20.7
1.0×10^{18}	20.7

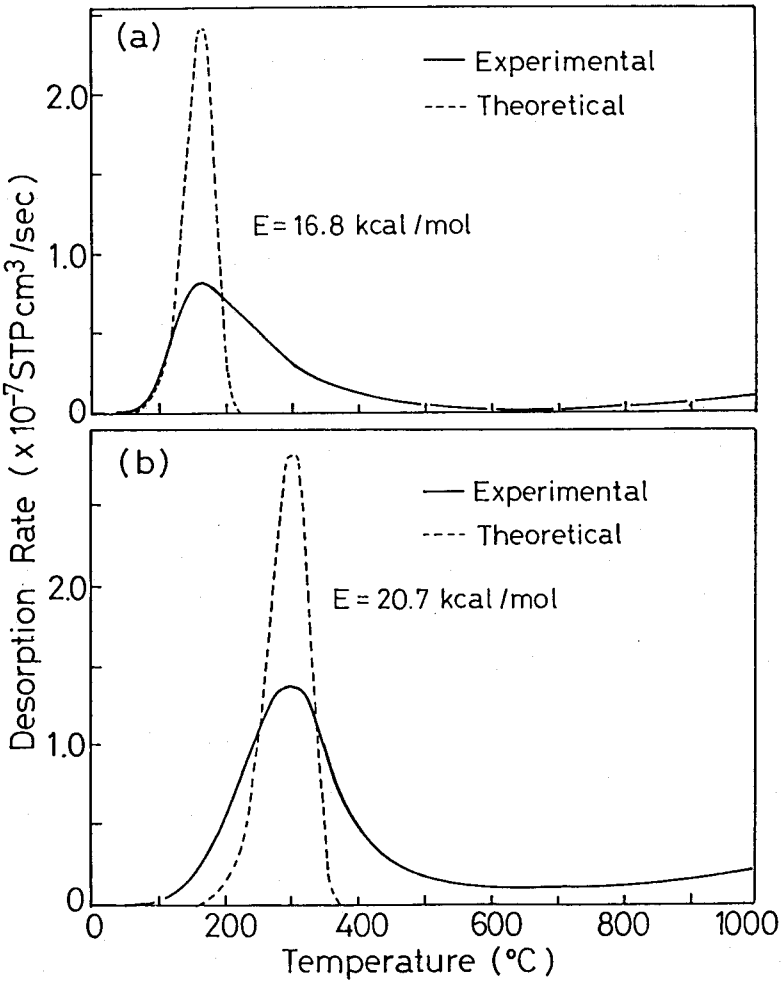

Fig. 6-8 Theoretical thermal desorption curves controlled by detrapping process.
(a) 5.0×10^{16} ions/cm²
(b) 5.0×10^{17} ions/cm²

this tendency supports that the desorption model can be explained by the simple first-ordered process. Möller et al.[2] have reported that the number of traps increase as the dislocation loops grow with the irradiation dose, but that above a certain critical dose no change in the number or characteristics of the traps occur as the irradiation dose increases. If the irradiation dose exceeds the critical value, the activation energy, Ed for desorption and the amount of released helium would be almost constant as described above. Changes in Ed with various irradiation doses (Table 6-1) appear to reflect the characteristics of the traps. From these results, we may assume a critical dose of approximately 5×10^{17} ions/cm^2. They have also reported that prism-oriented pyrolytic graphite irradiated with 8 keV He^+ ions have an activation energy of 1 ± 0.1 eV (23 kcal/mol) which is the sum of the trap binding energy and the activation energy for diffusion [2].

In the first place, analysis of thermal desorption curves has been performed by assuming the detrapping-controlled process. The results of calculation for detrapping are shown in Fig. 6-8. Theoretical desorption curves are considerably sharp as compared with experimental desorption curves. The main causes of disagreement can be listed as follows :

i) existence of various trapping sites
(distribution of trap binding energy)
ii) effect of diffusion
iii) effect of retrapping
iv) experimental error

Cause i) will affect the both temperature sides (higher and lower) of desorption curve to make the curve broader, and causes ii) and iii) will contribute to the higher temperature side of desorption curve to make tailing (cf. Fig.9-2(d) in Appendix).

In Fig. 6-8(a), the theoretical curve agrees well with the experimental desorption curve for the lower temperature side (R.T.- 120℃), hence thermal desorption behavior for lower irradiation doses (e.g. 2.0×10^{16} ions/cm^2 and 5.0×10^{16} ions/cm^2 (Fig. 6-1(a))) may be affected by diffusion or retrapping (causes ii) or iii)). It is possible that the trapping sites are not developed sufficiently at lower irradiation doses if the trap binding energy increases apparently with irradiation dose. In such a case, diffusion process will be dominative rather than detrapping process. On the other hand, if the retrapping process (cause iii)) is effective to the thermal desorption of helium, helium desorption curves for higher irradiation doses should be also gentler for higher temperature side. Furthermore, thermal desorption curves for lower irradiation doses exhibit the typical shape of diffusion-controlled desorption of gaseous species implanted into a material (see Fig. 9-2(d)). For the above reasons, diffusion analysis was performed on the thermal desorption behavior for lower irradiation dose (2.0×10^{16} ions/cm^2). It is necessary to solve

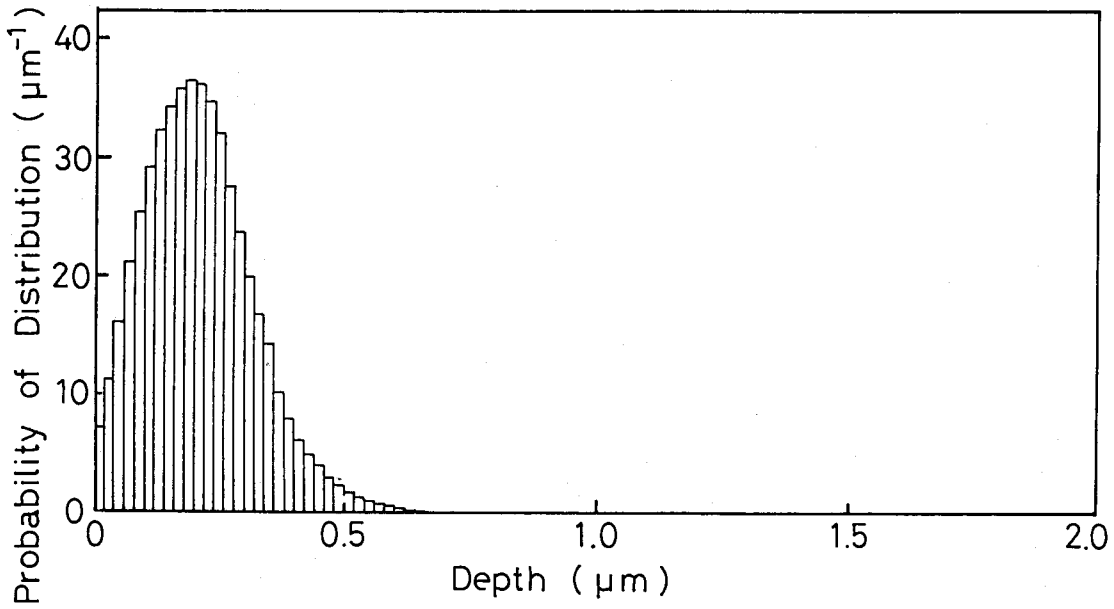

Fig. 6-9 Depth distribution of implanted helium used for diffusion analysis.

the finite difference equations (Fig.9-4 in Appendix) to analyse the diffusional release, since the process is non-steady state diffusion with variable diffusion coefficients and the initial helium distribution in graphite. The initial helium distribution used for the calculation is given in Fig. 6-9. The distribution was assumed to have the typical depth profile as reported by Möller et al. [2], and the mean projected range was settled to be 0.2 μm in accordance with the data obtained by Ziegler [10]. Desorption rates were calculated by solving the series of difference equations for 100 domains during a time interval of 0.1 second for the temperature range from 0 ℃ to 1000 ℃. As a typical result obtained in this calculation, theoretical desorption curve is shown in Fig. 6-10 for the diffusion coefficients of $D(cm^2/sec) \fallingdotseq 1.0 \times 10^{-7} \exp[-10.8(kcal/mol)/RT]$. The experimental desorption curve and theoretical curve are in good agreement, and the diffusion-controlled process may be adequate to analyze the helium desorption mechanism for the graphite irradiated at lower doses. Little information is available on the diffusion of helium in graphite at present. Diffusion data of helium reported by Holt et al. [13] and the results obtained in the present work are listed in Table 6-2. Further study is necessary to discuss the differences in these values and to estimate the desorption mechanism more concretely.

As for higher irradiation doses (above 5.0×10^{17} ions/cm^2), diffusion-controlled release will not affect any longer, since the helium desorption mainly takes place above 250 ℃ where the diffusion is considerably high. It is possible that the helium desorption behavior for

Table 6-2 Diffusion data of helium in graphite.

D_0 (cm^2/sec)	E (kcal/mol)	Temperature range (℃)	ref.
7.2×10^{-3}	19	350 - 850	[19]
1.0×10^{-7}	10.8	R.T.- 400	present work

higher irradiation doses is controlled by the detrapping process as shown from the shape of desorption curves (Fig. 9-2(a)). Theoretical curve fitting was performed for the desorption curve from the graphite irradiated at 5.0 × 10^{17} ions/cm² assuming the simple detrapping process. As shown in Fig.6-11, the experimental and the theoretical desorption curves correspond well. However, the activation energy for detrapping (8.07 kcal/mol) is considerably low, since the peak temperature of thermal desorption curve with such a low activation energy will shift markedly when the heating rate is varied. (In the heating rate variation experiment, peak temperature shift is larger for the lower activation energy (cf. Appendix)). This is inconsistent with the results of experiments with various heating rates (Fig. 6-7). If the various kinds of traps are produced by the He^+ ion irradiation, there will be the traps with different binding energies in graphite. Then, the Ed values determined by the peak shift may be the mean energy for detrapping among various binding energies

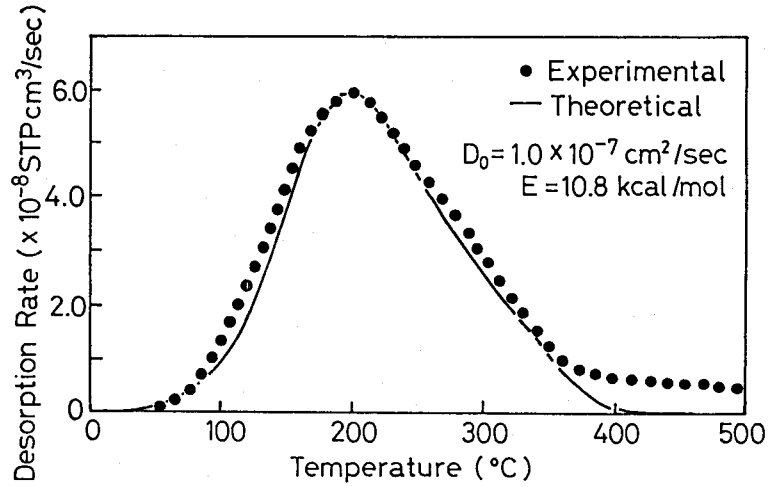

Fig. 6-10 Result of curve fitting for helium desorption from POCO DFP-3-2 irradiated at a dose of 2.0 × 10^{16} ions/cm².

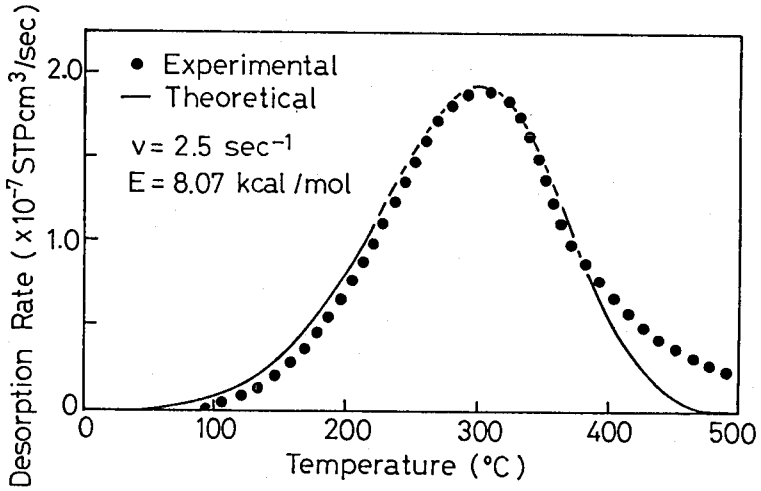

Fig. 6-11 Result of curve fitting for helium desorption from POCO DFP-3-2 irradiated at a dose of 5.0 × 10^{17} ions/cm².

of helium traps. Hence, the activation energy for desorption may distribute around the Ed value. Further experiments (e.g. step heating desorption test) are needed to clarify the distribution of trap binding energy.

The release mechanism of helium from graphite may be attributed to the diffusion-controlled process and the detrapping-controlled process for lower irradiation doses and higher irradiation doses, respectively. This model is highly suggestive on the fact of two distinct peaks (200 ℃ and 300 ℃) observed for ISOGRAPH-88 irradiated at doses of 7.0×10^{17} ions/cm^2 and 1.0×10^{18} ions/cm^2 (Fig.6-2(b)).

4. Concluding remarks

Thermal desorption behavior of helium from various graphite samples irradiated with 20 keV He^+ ions has been studied. The results of this study may be summarized as follows:

(1) Thermal desorption of helium depends considerably on the structure of the graphite samples studied here.

(2) The peak temperatures of helium thermal desorption curves from POCO DFP-3-2, ISOGRAPH-88 and PAPYEX rose with increasing irradiation doses and became constant at approximately 330 ℃ for POCO DFP-3-2 and ISOGRAPH-88 and at approximately 200 ℃ for PAPYEX.

(3) The amount of helium released from POCO DFP-3-2 and ISOGRAPH-88 increased with irradiation dose and reached a constant value for irradiation doses exceeding 1.0×10^{18} ions/cm^2.

(4) The amount of helium released from PAPYEX reached a maximum at a dose of 5.0×10^{17} ions/cm^2 and drastically decreased by macro-exfoliation above this dose. The amount of helium retention in PAPYEX was affected by the surface conditions.

(5) Glassy carbon retained only 22 % of the helium retention for isotropic

graphite at the same irradiation dose.

(6) The peak shift with irradiation dose may be explained by the increase of trap binding energy with the development of dislocation loops.

(7) The desorption mechanism of helium from graphite may be attributed to the diffusion-controlled process for lower irradiation doses (below 5.0×10^{16} ions/cm^2). And at higher irradiation doses (above 5.0×10^{17} ions/cm^2), the helium desorption may be controlled by the detrapping process which have various trap binding energies.

References

[1] R.A.Langley, R.S.Blewer and J.Roth, J.Nucl.Mater. 76/77 (1978) 313.

[2] W.Möller, B.M.U.Scherzer and J.Ehrenberg, J.Nucl.Mater. 111/112 (1982) 669.

[3] H.Atsumi, S.Tokura, T.Yamauchi, S.Yamanaka and M.Miyake, J.Nucl.Mater. 141-143 (1986) 258.

[4] S.Tokura, H.Atsumi, T.Yamauchi, M.Sinno, S.Yamanaka and M.Miyake, J.Nucl.Mater. 155-157 (1988) 246.

[5] K.L.Wilson, IPPJ-AM-50 (1987) 238.

[6] M.A.Ulrickson, IPPJ-AM-50 (1987) 475.

[7] M.Saidoh, R.Yamada and K.Nakamura, J.Nucl.Mater. 102 (1981) 97.

[8] K.Sone and G.M.McCracken, J.Nucl.Mater. 111/112 (1982) 606.

[9] P.C.Stangeby, O.Auciello, A.A.Haasz and B.L.Doyle, J.Nucl.Mater. 122/123 (1984) 1592.

[10] J.F.Ziegler, "Stopping Powers and Ranges in All Elements, vol.4 Helium" (Pergamon Press, New York, 1977) p.98.

[11] G.M.Jenkins and K.Kawamura, "Polymeric Carbons-Carbon Fibre, Glass and Char" (Cambridge University Press, Cambridge, 1976) p.67.

[12] S.Vepřek, A.P.Webb and H.Stuessi, in: "Proc. Int. Symp. on Plasma wall Interaction", Jülich (1976) p.431.

[13] J.B.Holt, M.W.Guinan, D.W.Hosmer, R.H.Condit and R.J.Borg, in: "Proc. 2nd Topical Meeting on the Technology of Controlled Nuclear Fusion, vol.Ⅳ ", Richland, Washington (1976) p.1565.

Ⅶ Absorption and Desorption of Deuterium on Graphite Exposed to Deuterium Gas Atmosphere at Elevated Temperatures

1. Introduction

According to a review paper [1] and numerous literature (e.g. refs. [2-7]), the retention and thermal release of hydrogen isotopes on graphite implanted with ions have been studied by a surprisingly large number of investigators. However, only a little information is available on the absorption and desorption behavior on graphite thermally exposed to hydrogen isotopes at elevated temperatures [2,3,8,9] as compared with hydrogen isotopes by ion implantation. This may be mainly due to 1) hydrocarbon formation during D_2 gas exposure at elevated temperatures, 2) low solubility of hydrogen in graphite, 3) the complicated structure of graphite with many closed or open pores, 4) the lack of data needs for practical use. It is important to know the fundamental properties (solubility, diffusivity, etc.) of hydrogen isotopes and helium in graphite to estimate the gas recycling behavior on graphite under various conditions.

In this chapter, measurements of the solubility and thermal desorption of deuterium have been performed on isotropic graphite exposed thermally to deuterium gas atmosphere under various conditions. And by using these data, the diffusion coefficients of deuterium in graphite and deuterium uptaking on graphite were discussed.

2. Experimental

The samples used in the present study were high density isotropic graphite sheets composed of fine grains (ISOGRAPH-88, 10× 10× 1 mm). These graphite samples were degassed at 1100 ℃ for two hours in a vacuum below 10^{-3} Pa before absorption and desorption experiments.

(1) Deuterium solubility measurement

Deuterium absorption measurements of D_2 on graphite were carried out with the apparatus displayed in Fig.7-1. In the absorption experiments, the graphite samples in the deuterium atmosphere were heated at the desired temperature of 850 - 1050 ℃ in a closed constant volume system, and the change in deuterium pressure due to absorption was measured with a Baratron manometer until the equilibrium pressure was established at each temperature.

(2) Desorption experiment

The treatment procedure for graphite samples used in the thermal desorption experiments is shown in Fig.7-2. The graphite samples occluding deuterium were prepared by deuterium exposure at a given temperature, T, within 200 - 900 ℃ under a pressure of 5 - 95 kPa for 0.1 - 20 h. After holding these graphite samples for the desired time in deuterium gas atmosphere, they were quenched to room temperature. Relatively high temperatures and pressures were chosen in order to dissolve a much larger amount of deuterium in the graphite grains compared with the amount

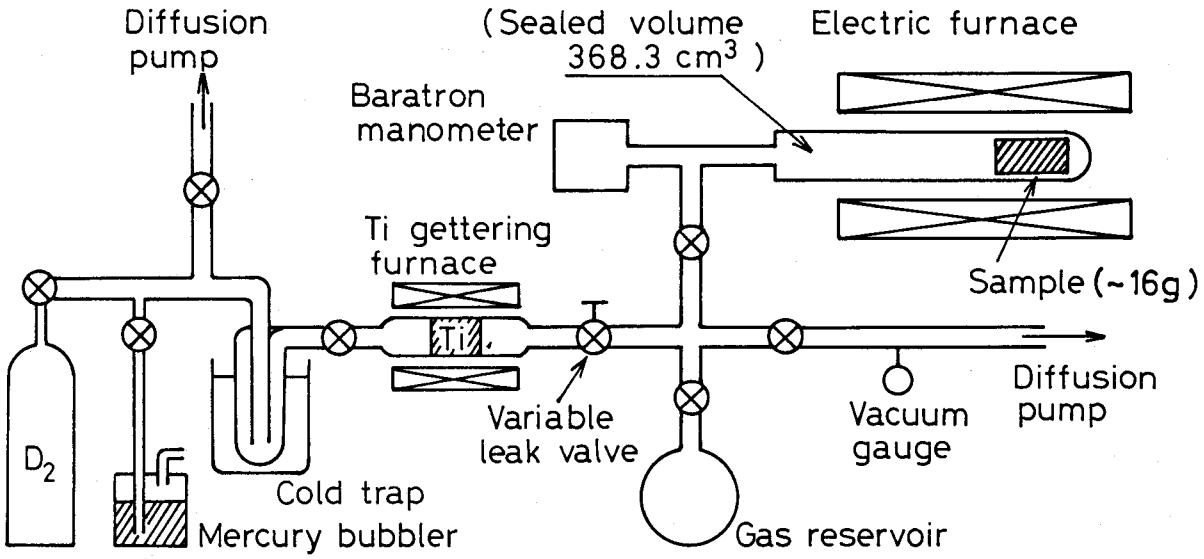

Fig. 7-1 Schematic diagram of the apparatus for the measurements of deuterium solubility in graphite.

adsorbed, since graphite usually adsorb a large amount of hydrogen at grain surfaces or in micro-pores. Thermal desorption measurements of deuterium were made at a constant heating rate of 10 ℃/min in a vacuum below 10^{-5} Pa. In order to determine the desorption mechanisms, step heating tests (reaching a desired temperature within 1 min) at 300 - 900 ℃ were also performed. Released species were analyzed with a quadrupole mass spectrometer.

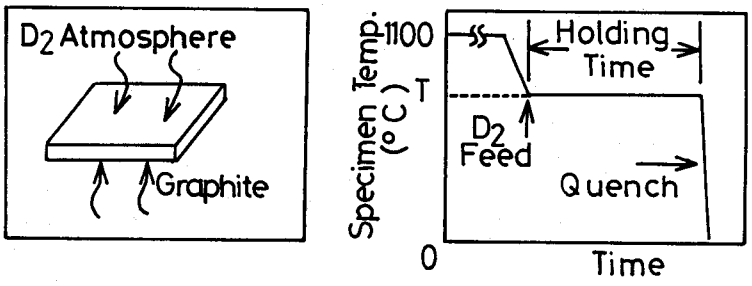

Fig. 7-2 Experimental procedure of D_2 gas exposure.

3. Results and discussion

3.1 Solubility of deuterium in graphite

Hydrogen seems to be soluble in graphite with a positive heat of solution [3,9], and the value was reported to be 33 kcal/mol [9]. Fig.7-3 shows the results of deuterium absorption experiments on graphite at 850 - 1050 ℃. The methane formation at this temperature and pressure range can be neglected by the calculation of CD_4 equilibrium pressures. The solubility of deuterium may increase proportionally to the square root of the deuterium gas pressure. From the present data shown in Fig.7-3, the solubility, S ($STPcm^3/g$), can be expressed by the equation :

$$S = 1.9\times 10^{-4}\ P^{1/2}(Pa) \times \exp[4.5\ (kcal/mol)/RT] \quad (850 - 1050\ ℃). \quad (1)$$

The extrapolated values of the solubility at one atmospheric pressure are shown in Fig.7-4 with the reported values obtained by Causey et al.[9] for laminar pyrolytic carbon. Both the heat of solution and the solubility are quite low compared with that reported for the temperature range of 1100 -

1500 ℃. Further measurements with a wide temperature range and under various pressure conditions are necessary to discuss the differences in these values.

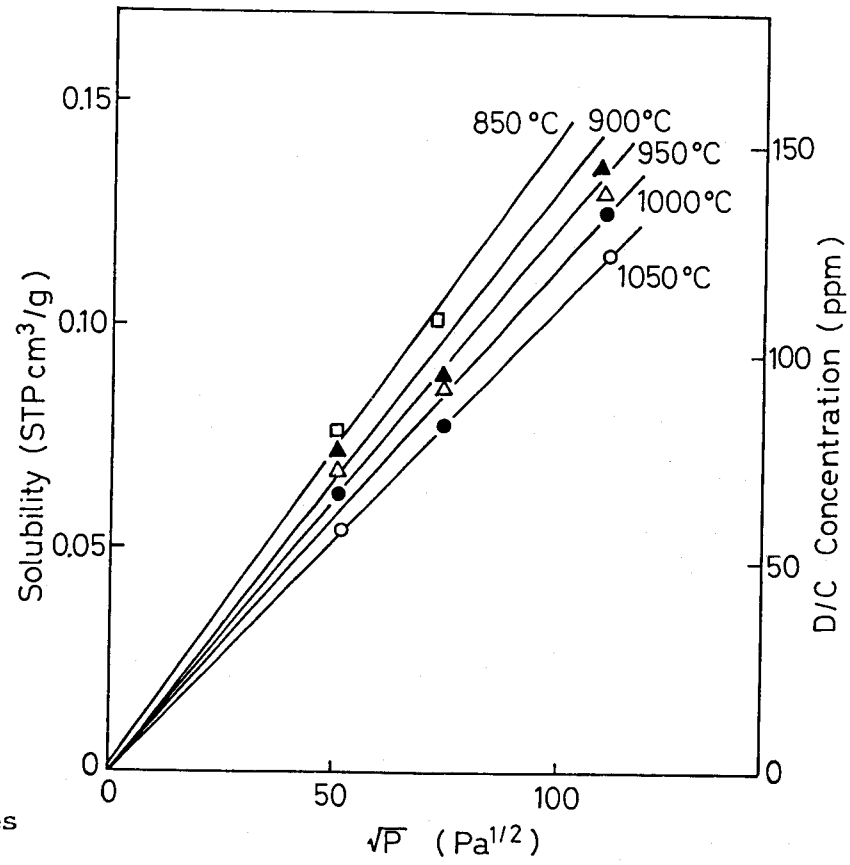

Fig. 7-3 Solubility isotherms for deuterium on graphite.

3.2 Thermal desorption measurements

Figure 7-5(a) gives deuterium desorption curves for the graphite exposed to D_2 gas at 700 ℃ for various exposure times. These curves show similar shape and peak temperature at approximately 930 ℃ for various exposure times. In Fig.7-5(b), total amount of deuterium released from graphite, i.e. integrated values of deuterium desorption curves, are plotted as a function of square root of exposure time. The amount of deuterium

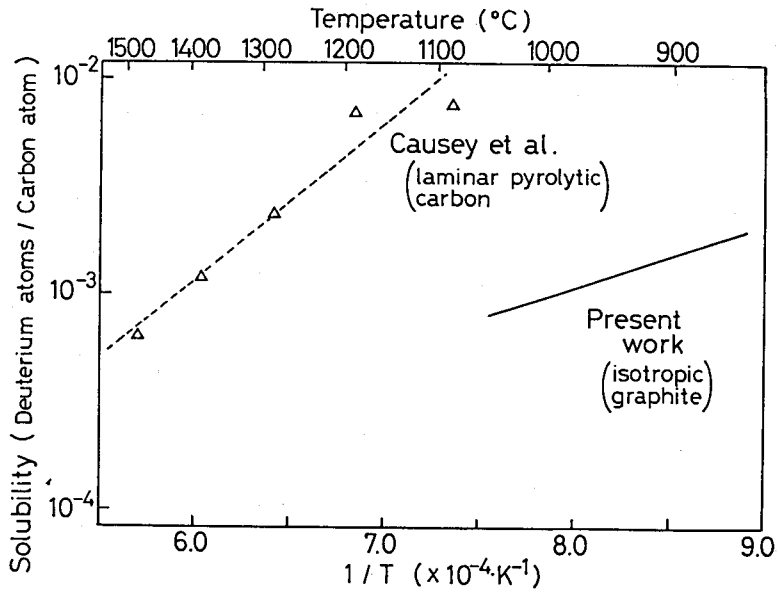

Fig. 7-4 Deuterium solubility at one atmosphere in isotropic graphite (ISOGRAPH-88) and laminar pyrolytic carbon [9] as a function of temperature.

increases in proportion with the square root of exposure time for short time gas exposure and then approaches to a constant value for exposure time above 10 hours.

Figure 7-6 (a) gives deuterium desorption curves for the graphite exposed to deuterium gas of various pressures at 700 ℃ for 5 hours. These curves also show similar shape and peak temperature for various deuterium gas pressures. In Fig.7-6(b), the total amounts of deuterium from graphite are plotted as a function of square root of deuterium gas pressure during exposure. The amount of deuterium rises in proportion with the square root of deuterium gas pressure. Hence deuterium in the graphite sample would

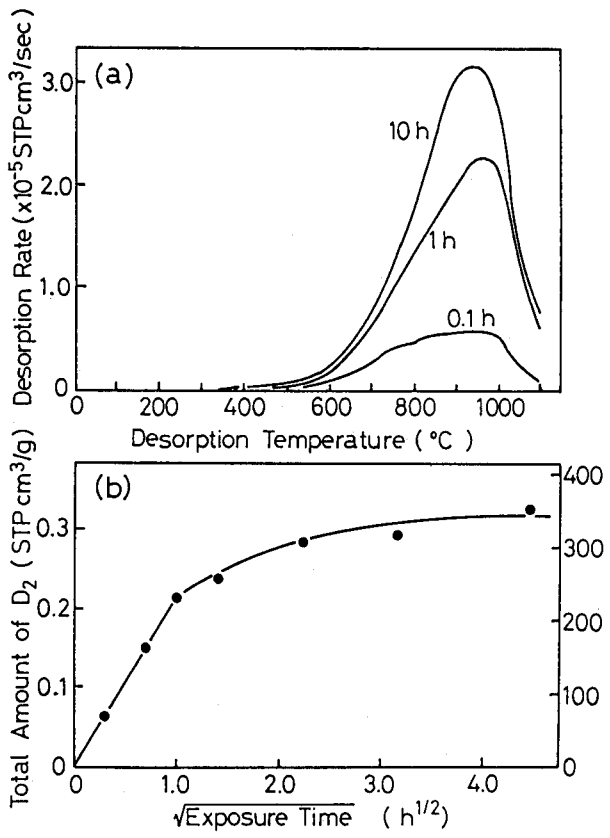

Fig. 7-5 Thermal desorption of D_2 from graphite exposed to D_2 for various times (700 ℃, 60 kPa).
(a) thermal desorption curves for various times
(b) total amount of D_2 released from graphite

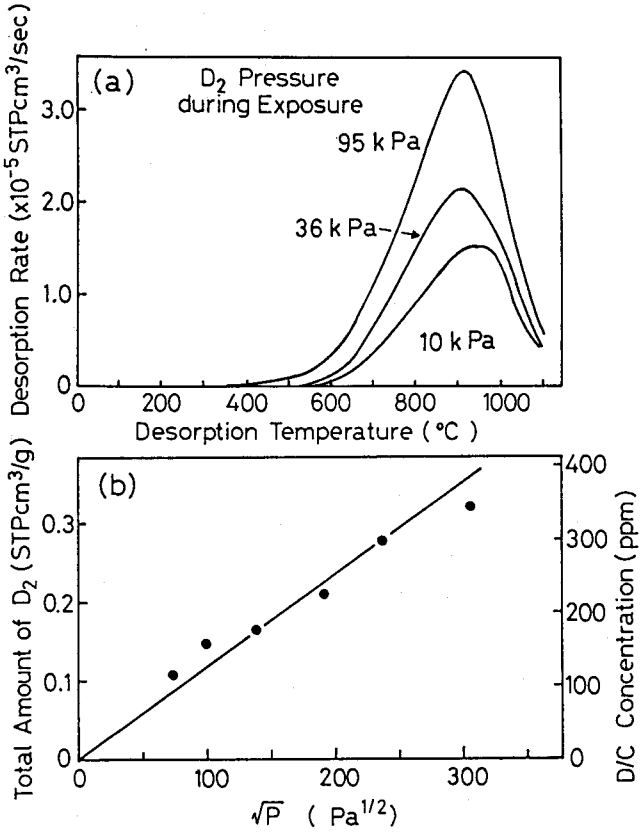

Fig. 7-6 Thermal desorption of D_2 from graphite exposed to D_2 under various D_2 gas pressures (700 ℃, 5 h).
(a) thermal desorption curves for various pressures
(b) total amount of D_2 released from graphite

exist as the solution in the form of deuterium atom.

Figure 7-7(a) gives deuterium desorption curves for the graphite exposed at various temperatures for 5 hours under the deuterium gas pressure of 60 kPa. Both shape and peak temperature (apparently seen in Fig.7-7) considerably change with the exposure temperature. Apparent peak temperatures of thermal desorption curves are listed in Table 7-1. As shown in the table, the peak temperature increases with exposure temperature. In Fig.7-7(b), the total amounts of deuterium from graphite are plotted as a function of exposure temperature. This figure shows that a significant amount of absorption of deuterium occurs above 400 ℃. The total amount of released deuterium increases with the exposure temperature up to 700 ℃ and then tends to decrease above this temperature. This behavior can be explained by the

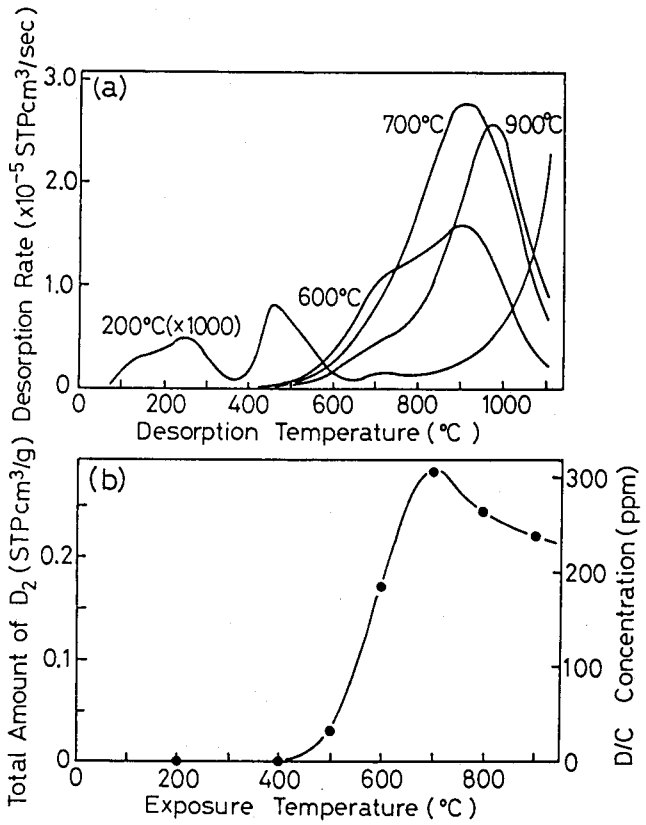

Fig. 7-7 Thermal desorption of D_2 from graphite exposed to D_2 at various temperatures (60 kPa, 5 h).
(a) thermal desorption curves for various temperatures
(b) total amount of D_2 released from graphite

Table 7-1 Peak temperatures of thermal desorption of D_2 from graphite exposed to deuterium at various temperatures.

Exposure temperature (℃)	Peak temperature (℃)
200	250, 460
400	440, 710
600	890
700	920
800	950
900	980

deuterium diffusion process into the graphite filler grains as mentioned below. Since it is necessary to have much longer saturation time at lower exposure temperatures, the amount of deuterium uptake during the same exposure time will decrease with decreasing temperature. From eq.(1), the solubility of D_2 in graphite will decrease with increasing temperature. Then, the amount of deuterium uptake should decrease with increasing temperature above 700 ℃ after which the deuterium is almost saturated in the graphite filler grains.

Figure 7-8 shows the methane desorption curves for the graphite exposed at various temperatures. The ion current (desorption rate) of deutero-methane is three orders of magnitude smaller than that of deuterium desorption. This may not complicate the desorption mechanism.

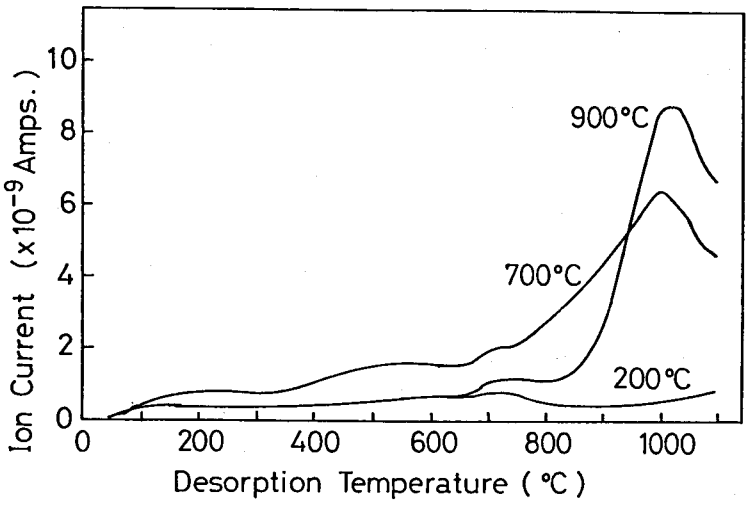

Fig. 7-8 Thermal desorption curves of CD_4 from graphite exposed to D_2 at various temperatures (60 kPa, 5 h).

3.3 Desorption mechanism

The graphite sample which was exposed at 700 ℃ under a pressure of 60 kPa for 5 h was used for analyzing the desorption mechanism, since it could be considered as a nearly saturated sample by the deuterium gas charge (Fig.7-5). Figure 7-9 gives deuterium desorption rate in logarithmic scale, which is redrawn of Fig.7-7, as a function of desorption temperature. The deuterium desorption curve on graphite exposed to D_2 gas at 700 ℃ appears to consist of three peaks. Namely, this thermal desorption curve can be

explained by the overlap of peaks Ⅰ, Ⅱ and Ⅲ with each maximum at approximately 140 ℃, 480 ℃ and 930 ℃, respectively. Röhrig et al.[8] have also reported three peaks in thermal desorption curves on graphite exposed to a hydrogen gas atmosphere at 900 ℃. These peak temperatures are similar to the present results, although the peak heights differ. Peak Ⅰ may be caused by the release of physically or chemically adsorbed deuterium onto the graphite surface. In this study, peaks Ⅱ and Ⅲ have been considered in detail. The change in the amount of deuterium with the exposure pressure has been discussed separately on peaks Ⅱ and Ⅲ. In Figs.7-10(a) and (b), the amount of released deuterium is plotted for the graphite samples exposed to deuterium gas of various pressures at 700 ℃ for 5 h. From these figures, the deuterium amount for peak Ⅱ appears to be proportional to the deuterium gas pressure during exposure, and that for peak Ⅲ appears to be proportional to the square root of the deuterium gas pressure. In peak Ⅱ, therefore, deuterium in the graphite probably exists as

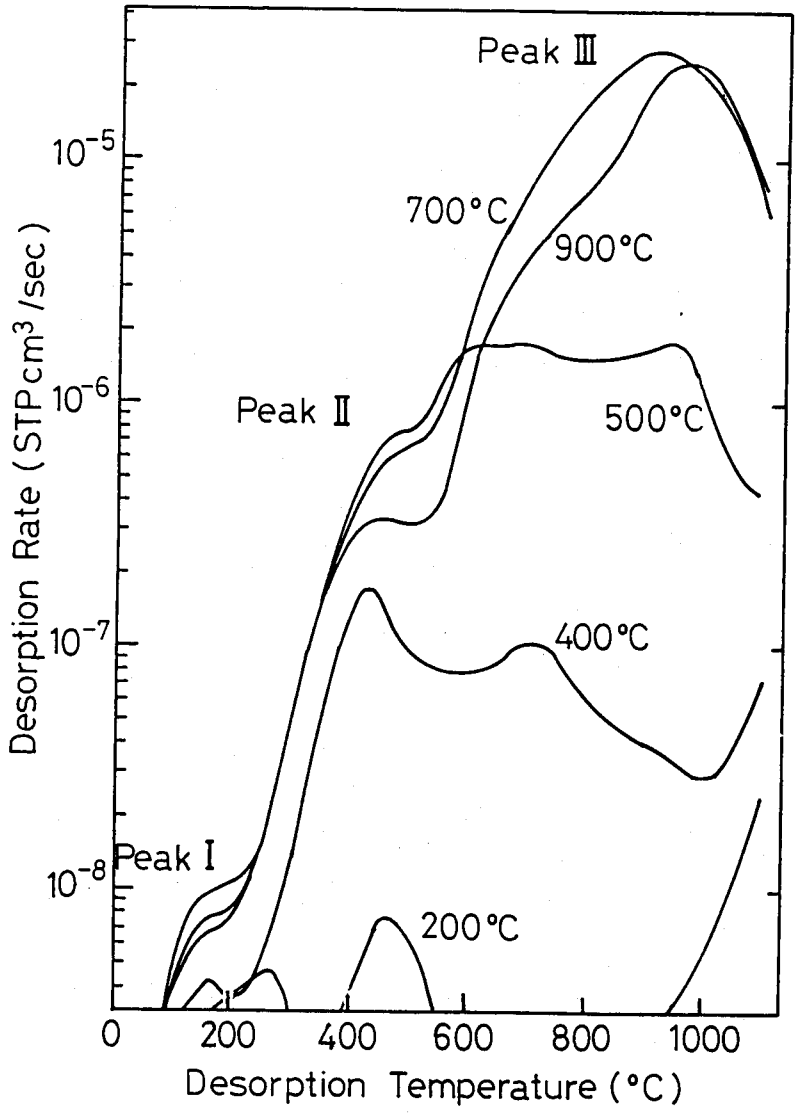

Fig. 7-9 Thermal desorption curves of deuterium for graphite exposed to D_2 at various temperatures (60 kPa, 5 h).

deuterium molecules. On the other hand, the deuterium corresponding to peak Ⅲ probably exists in the form of deuterium atoms.

Causey et al. [3] have reported that the retention of deuterium in POCO AXF-5Q graphite at 1200 ℃ did not increase as the pressure was increased from 0.66 to 66.0 Pa. Saturated concentration was determined to be 16 ppm. In the case of the present work, the influence of the pressure on deuterium retention could be observed. This may be attributed to the very high content of dissolved deuterium (compared to Causey et al.) due to the considerably high exposure pressures. Causey et al. [3] deduced that deuterium would be trapped at high energy sites in the carbon grains, however, according to this study, it is likely that deuterium is dissolved in some different sites.

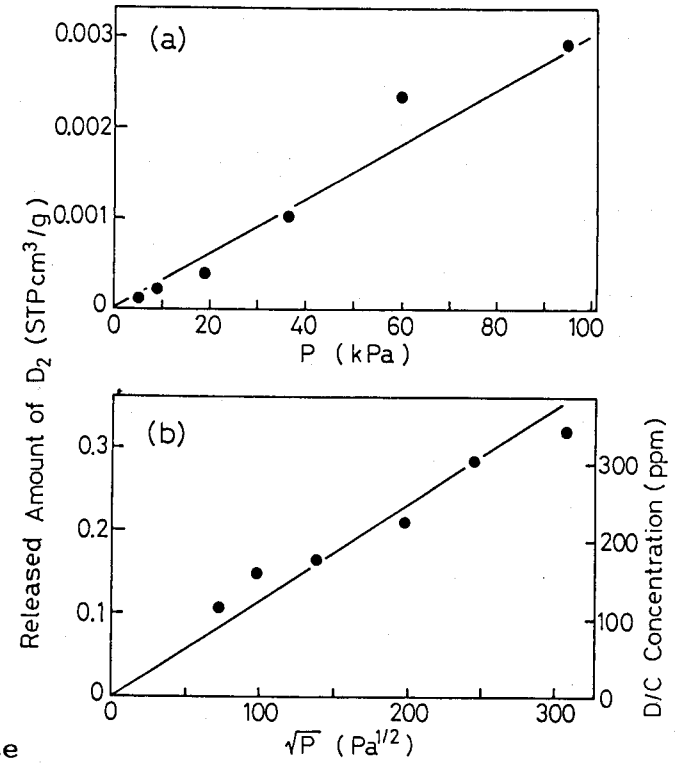

Fig. 7-10 Influence of D_2 gas pressure on the amount of deuterium released from graphite (700 ℃, 5 h).
(a) : peak Ⅱ , (b) : peak Ⅲ

The following five processes can be listed for the possible rate-determining step of deuterium desorption from graphite.

1) detrapping process (first-ordered reaction)
2) recombination process (second-ordered reaction)
3) diffusion process
   i) diffusion in a plane sheet (one-dimensional : 1 mm)
   ii) diffusion in a sphere (graphite filler grain : ～ 5 μm)

4) detrapping and diffusion process

5) diffusion and recombination process

To determine the desorption mechanism of deuterium from the graphite samples, thermal desorption measurements on a thinner graphite sample with a thickness of 0.45 mm were performed, and the result is shown in Table 7-2 with the result for a thick (1.0 mm) graphite sample. Desorption behavior was similar to that in the thick graphite sample, however, only the maximum temperature of peak Ⅱ shifted from 480 to 435 ℃. This suggests that peak Ⅱ resulted from one-dimensional diffusion in the plane sheet, since the process 1) and 3ii) will not shift the peak temperatures and process 2) will make the peak shift toward opposite temperature side. It can be concluded that peak Ⅱ may be attributed to pore diffusion.

Table 7-2 Peak temperatures of thermal desorption tests on graphite samples with different thickness.

Thickness (mm)	Peak Ⅱ (℃)	Peak Ⅲ (℃)
0.45	435	925
1.0	480	920

The desorption mechanisms for peak Ⅲ have been discussed as the following. The three cycle heating test, which is the repetitional heating to desired temperatures, was performed at a heating rate of 20 ℃/min. A result of the test is shown in Fig.7-11. The peak temperatures shift

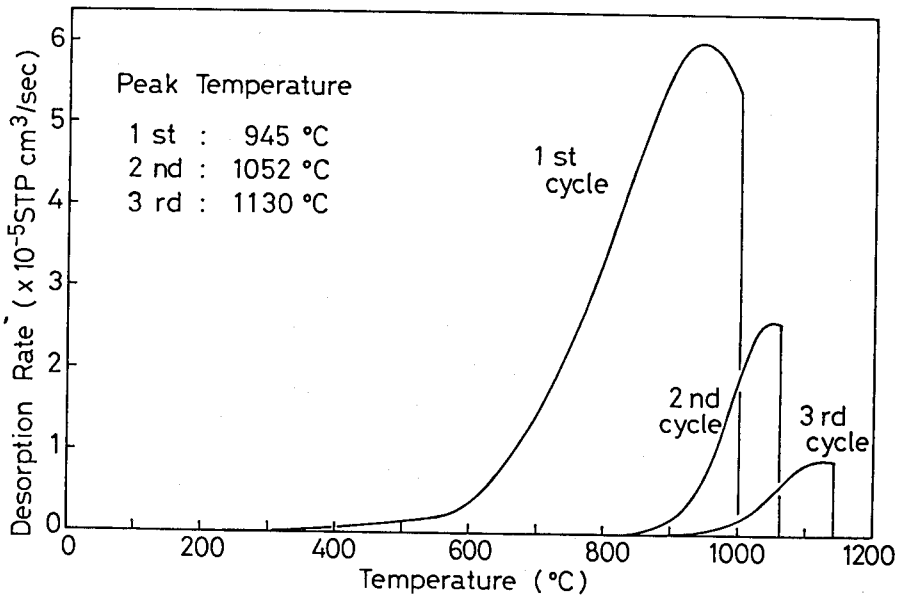

Fig. 7-11 Thermal desorption curves of deuterium in the 3 cycle desorption test (700 ℃, 60 kPa, 5 h, heating rate 20 ℃/min).

toward higher temperature in keeping with the repetition of heating. According to the result, processes 1) and 3 i) may not be the rate-determining step of deuterium thermal desorption. To determine the release mechanism from the graphite sample, step heating tests at 300 - 900 ℃ were performed on the graphite samples exposed to D_2 gas at 700 ℃ under a pressure of 60 kPa for 5 h. Isothermal desorption curves in the step heating tests (solid curves) and calculated curves for process 2) (dashed curves) are shown in Fig.7-12. Since the estimation which assumed the recombination process differs from the desorption curves, process 2) should be excluded from the candidates of rate-determining step. Desorption curves derived from process 1) should indicate exponential decrease (Fig.9-5(a)), therefore process 1) should not be the rate-determining step. If the rate-determining step is attributed to the process 3 i), the temperature of peak Ⅲ for thermal desorption from a thinner graphite sample will shift to lower temperature. However, according to Table 7-2, the peak temperature did not shift from that for a graphite sample with thickness of 0.45 mm. Since thermal desorption curves calculated for process 4) usually show the "tailing" toward higher temperature [10,11], this estimation can not be consistent with the actual measurements.

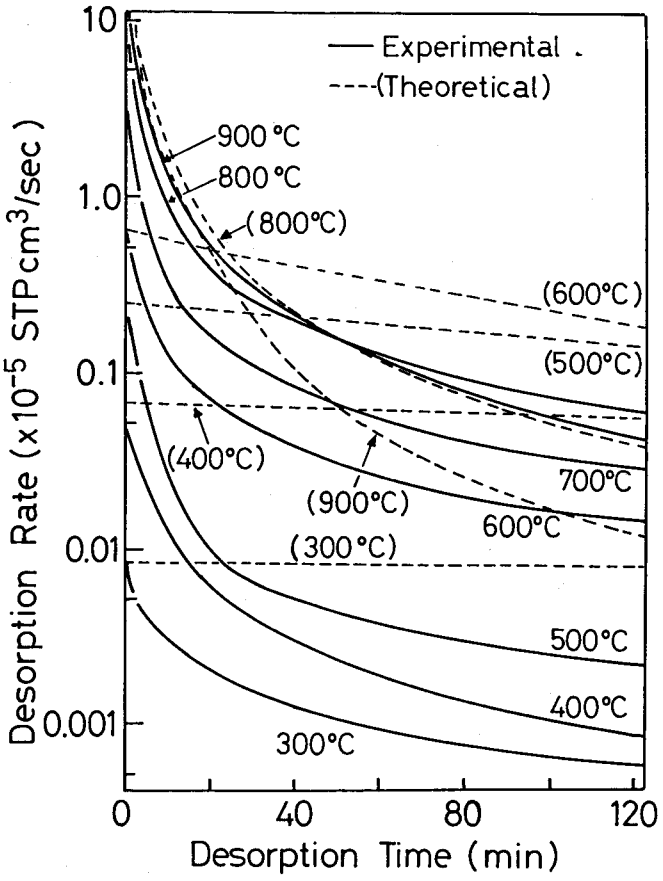

Fig. 7-12 Isothermal desorption rate of D_2 in step heating tests and analysis for recombination-controlled process.

Process 5) means the recombination process succeeding the diffusional transportation. Recombination process will suppress the migration toward the surfaces especially at the initial stage of desorption, then the step desorption curve will show gentler slope compared with that for the process 3ii). For the above reasons, process 3ii) is probably the most plausible process of rate-determining step for deuterium release from graphite.

Röhrig et al. [8] have proposed that the bulk diffusion process in the graphite filler grains would dominate the tritium release from the reactor graphite irradiated by neutrons, and estimated the activation energy to be about 60 kcal/mol. In the present study, the deuterium desorption provided by peak Ⅲ should be controlled by the same process as discussed above. To determine the diffusion coefficient in the graphite filler grains, it is necessary to determine the dimensions of filler grains. From the optical micrograph displayed in Fig.7-13, this sample has spherical filler grains with diameter of about 5 μm. The number fraction of diameter distribution of filler grains was determined from several micrographs. Using this number fraction, the volumetric fraction of diameter distribution was estimated to

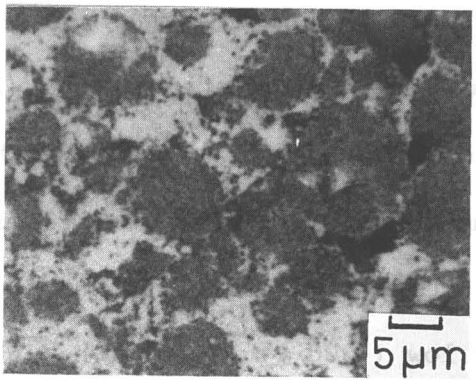

Fig. 7-13 Optical surface micrograph of ISOGRAPH-88.

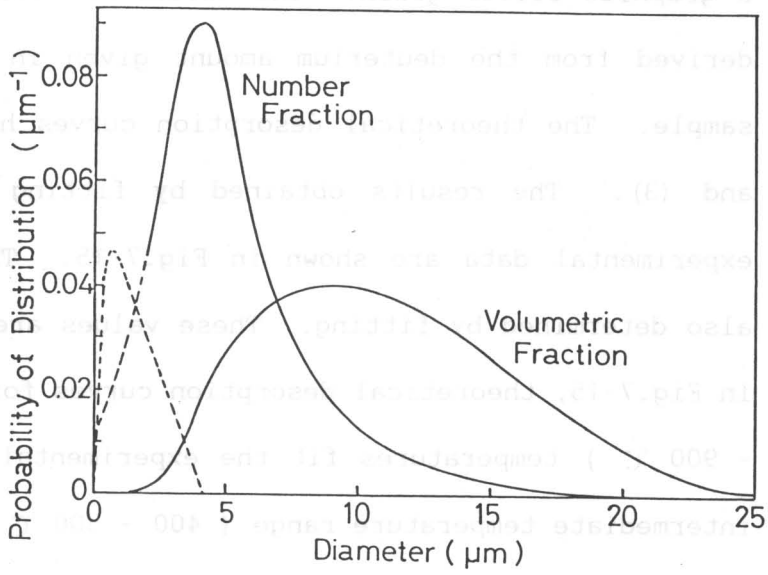

Fig. 7-14 Number fraction and volumetric fraction of diameter distribution of filler grains.

be shown in Fig.7-14. Since it is difficult to determine the diameter of small filler grains and impregnant, these volumetric fraction was assumed as the dashed curve illustrated in Fig.7-14, based on the comparisons of the sum of the filler volume with the sample volume. The radius of the graphite filler grains were divided into 17 groups of 0.025 - 15 μm and used for calculation.

Theoretically, the desorption rate, R (STPcm^3/sec), at each constant temperature can be given by the following equations [12] (cf. Appendix) : for the pore diffusion (peak Ⅱ),

$$R_{Ⅱ}(t) = 4.06 \times 10^{-4}\left[-\frac{d}{dt}\left(\frac{8}{\pi^2}\sum_{n=1}^{\infty}\frac{1}{(2n-1)^2}\exp\left(-\frac{(2n-1)^2\pi^2}{l^2}D_{Ⅱ}t\right)\right)\right] \quad , \quad (2)$$

for the bulk diffusion (peak Ⅲ),

$$R_{Ⅲ}(t) = 4.92 \times 10^{-2}\left[-\frac{d}{dt}\left(\frac{6}{\pi^2}\sum_{g=1}^{17}\left(f_g\sum_{n=1}^{\infty}\frac{1}{n^2}\exp\left(-\frac{n^2\pi^2}{r_g{}^2}D_{Ⅲ}t\right)\right)\right)\right] \quad , \quad (3)$$

where l (cm) is the thickness of the graphite sheet, D (cm^2/sec) is the diffusion coefficient of deuterium in graphite, t (sec) is the desorption time, f_g is the volumetric fraction of each radius, and r_g is the radius of a graphite filler grain. The values of 4.06×10^{-4} and 4.92×10^{-2} were derived from the deuterium amount given in Fig.7-10 and the mass of the sample. The theoretical desorption curves have been calculated by eqs.(2) and (3). The results obtained by fitting of theoretical curves to the experimental data are shown in Fig.7-15. The diffusion coefficients were also determined by fitting. These values are listed in Table 7-3. As seen in Fig.7-15, theoretical desorption curves for low (300 ℃) and high (600 - 900 ℃) temperatures fit the experimental data reasonably well. In the intermediate temperature range (400 - 500 ℃), the curves for peaks Ⅱ and Ⅲ overlap as shown in Fig.7-9. Deuterium desorption in this temperature range is affected by both pore and bulk diffusion release. As a result, the

pore diffusion coefficient, D_{II} (cm²/sec), and the bulk diffusion coefficient, D_{III} (cm²/sec) are expressed by

$$D_{II} = 1800 \times \exp\left(-\frac{29\ (\text{kcal/mol})}{R\,T}\right) \quad (300 - 500\ ℃), \quad (4)$$

$$D_{III} = 1.69 \times \exp\left(-\frac{60\ (\text{kcal/mol})}{R\,T}\right) \quad (500 - 900\ ℃). \quad (5)$$

The reported values of bulk diffusion coefficient of hydrogen isotopes in graphite are given in Table 7-4 and Fig.7-16. As shown in Table 7-4, the activation energies for diffusion are markedly larger compared with those for metals [16] (Ni: 9-10 kcal/mol, Fe: 10.7 kcal/mol, Cu: 9 kcal/mol) And the diffusion coefficients of tritium in graphite are also rather small. Diffusion coefficients of deuterium obtained in the present

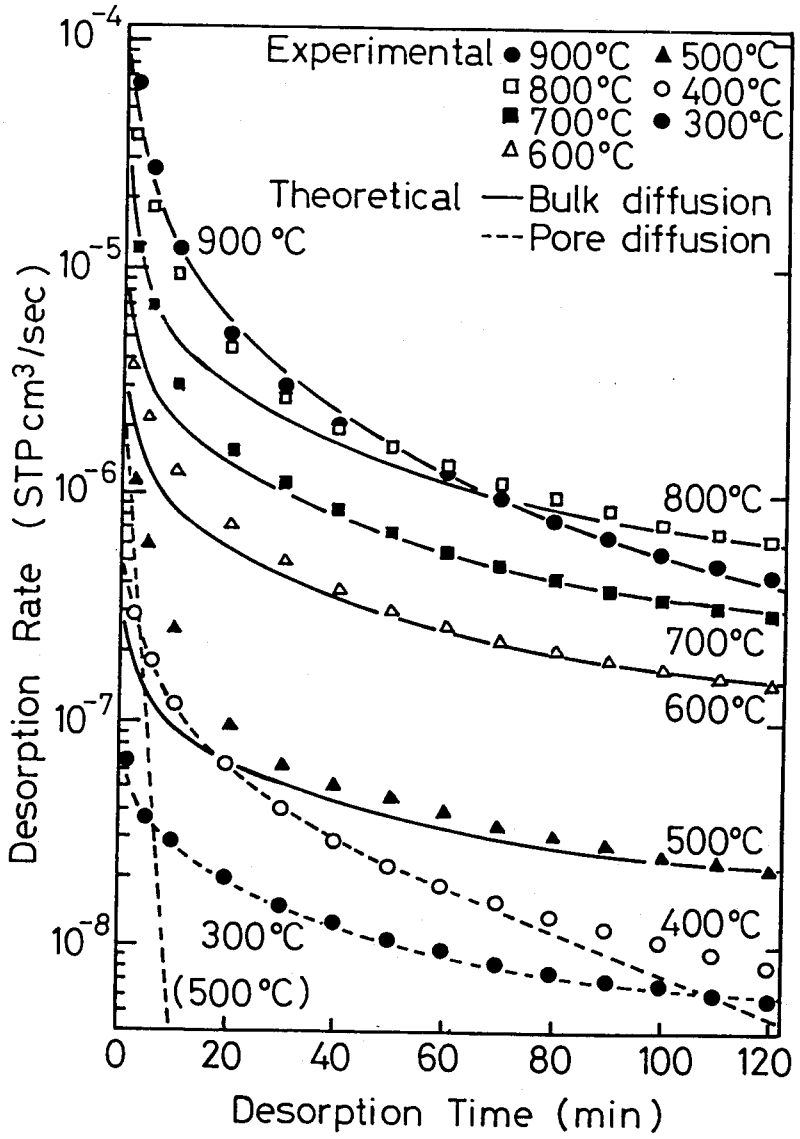

Fig. 7-15 Desorption curves obtained by fitting the theoretical curves to the experimental data.

Table 7-3 Diffusion coefficients of deuterium in graphite obtained by curve fitting.

Temperature (℃)	Diffusion coefficients (cm²/sec)	
	Pore diffusion (peak Ⅱ)	Bulk diffusion (peak Ⅲ)
300	1.6×10^{-8}	-
400	6.8×10^{-7}	-
500	1.1×10^{-5}	1.5×10^{-17}
600	-	8.0×10^{-16}
700	-	1.0×10^{-14}
800	-	2.0×10^{-13}
900	-	1.6×10^{-11}

Table 7-4 Comparison of the values of D_0 and activation energy E.

Species	Sample	D_0 (cm^2/sec)	E (kcal/mol)	Temperature (℃)	ref.
T_2	pyrolytic	2.78×10^{-8}	25.1	700-1000	[13]
T_2	pyrolytic	4.4×10^{-6}	32.0	800-1200	[9]
T_2	artifitial	1.04×10^{-8}	32.5	650-1000	[14]
T_2	natural	3.77×10^{-4}	51.4	650-1000	[14]
T_2	pyrolytic	2.48×10^{-3}	59.5	700-1000	[13]
T_2	pyrolytic	8.23×10^{-3}	62.3	700-1000	[13]
T_2	reactor grade	2.4×10^{-2}	64	700-1400	[8]
T_2	natural	8.59×10^{-2}	65.6	650-900	[14]
T_2	reactor grade	8.28×10^{-3}	87.0	700-1000	[15]
T_2	pyrolytic	3.3×10^{-2}	98.4	1155-1450	[9]
D_2	isotropic	1.69	60	500-900	present work

work are much larger than those for tritium reported by several authors, though the activation energy for diffusion is correspond well (Table 7-4 and Fig.7-16). It is said that the essential diffusion coefficient seems to be larger than reported values [2,14], since these data were determined almost for tritium diffusion mainly produced by $^3He(n,p)^3H$ or $^6Li(n,\alpha)^3H$ reaction. Namely, neutron irradiation produces

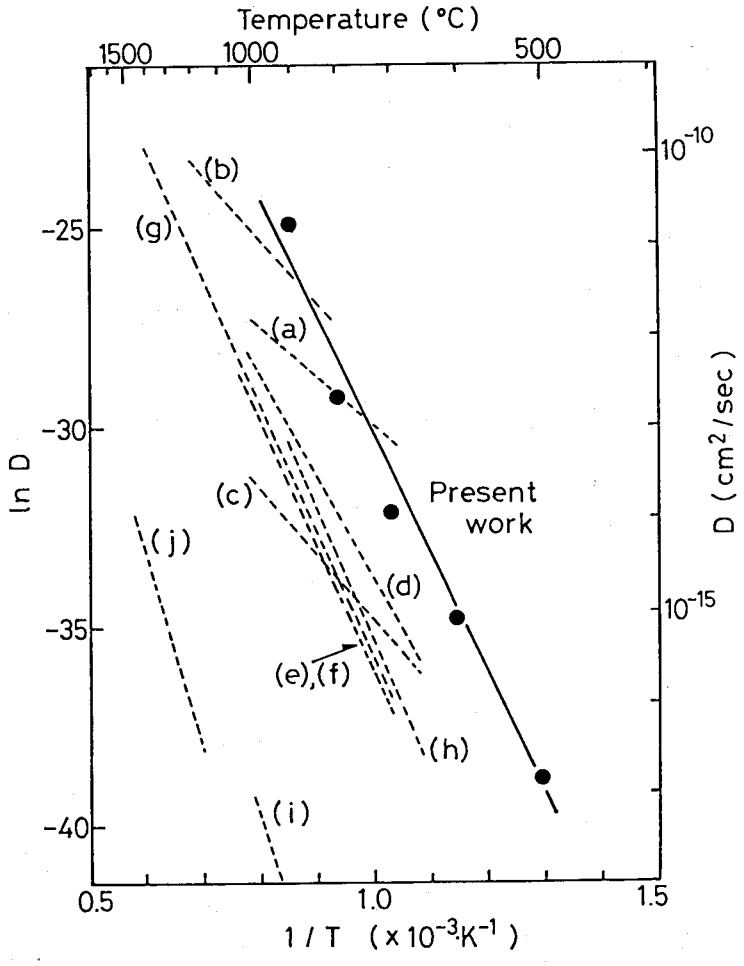

Fig. 7-16 Diffusion coefficients of deuterium in various types of graphite as a function of temperature.
(a), (e), (f): Saeki [13], (b), (j): Causey et al. [9]
(c), (d), (h): Saeki [14], (g) : Röhrig et al. [8]
(i) : Malka et al. [15]

many defects as the diffusion barrier and it will cause a low diffusion coefficient and a high activation energy. Moreover, the concentration of tritium in graphite would be much lower compared with the deuterium amount studied here. Then, the diffusion coefficient of tritium in graphite will be rather small, if a certain amount of traps with a high binding energy exists in a graphite sample. And the diffusion of deuterium in graphite should be faster than the tritium diffusion due to the isotope effects. Hence the diffusion coefficient obtained in the present study should be reasonable.

The thermal desorption curves of deuterium at a heating rate of 10 ℃/min were calculated from eqs.(2), (3), (4) and (5) with temperature extrapolation by means of a computation code for diffusional release (Fig.9-4). The result is given in Fig.7-17. As shown here, the experimental and the theoretical desorption curves correspond well. From the above results, it can be safely assumed that peaks Ⅱ and Ⅲ are attributed to pore diffusion and bulk diffusion, respectively.

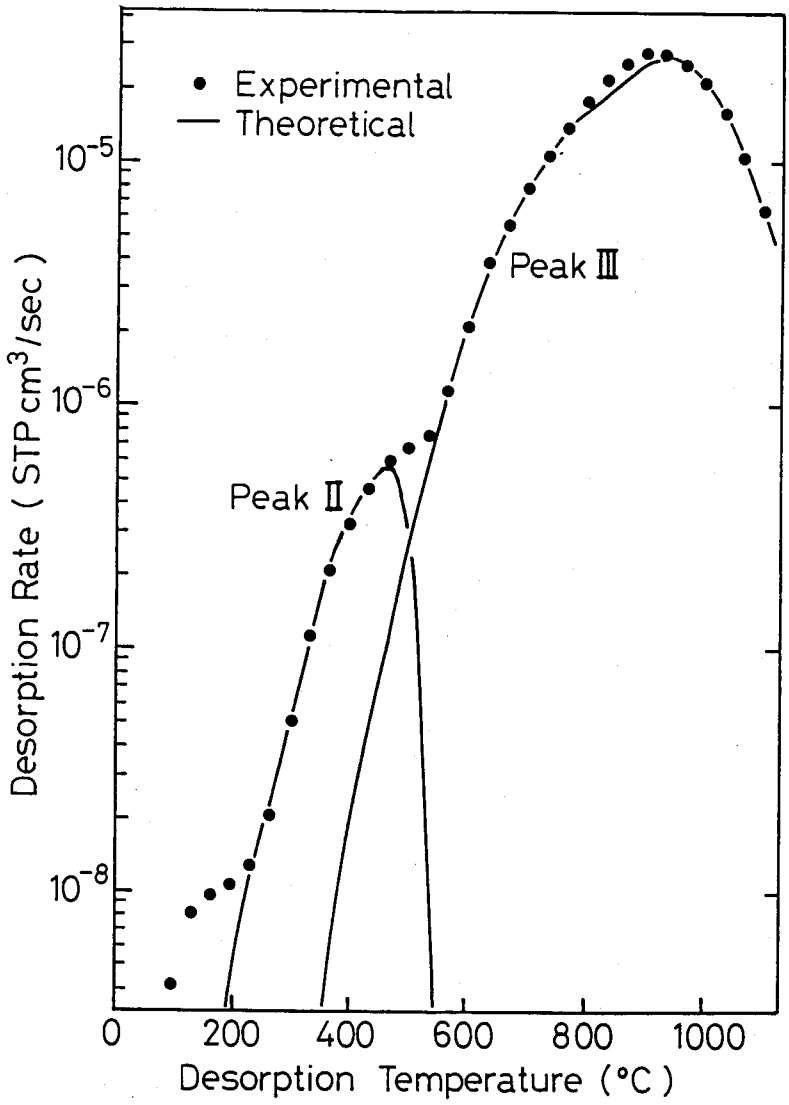

Fig. 7-17 Thermal desorption curve derived from diffusion analysis.

3.4 Deuterium retention in graphite at elevated temperatures

According to the results obtained in section 3.3, thermal desorption of deuterium could be explained well by the diffusion model. This model may be applicable to the deuterium uptaking behavior of graphite in a D_2 gas atmosphere. By using the diffusion data and eq.(1), deuterium uptaking behavior for various exposure times was estimated as a function of exposure temperature. As shown in Fig.7-18, a shorter exposure time causes the maximum temperature of deuterium retention to shift toward higher temperature. From this figure, the maximum temperature of deuterium retention with a 5-h exposure time should be approximately 850 ℃, whereas the experimental results show the maximum temperature to be 700 ℃ (Fig.7-7). This discrepancy may be caused by the difference between the inward migration rate and the outward migration rate.

Further study will be required on graphite with different grain sizes to assess more concretely the reliability of this diffusion model.

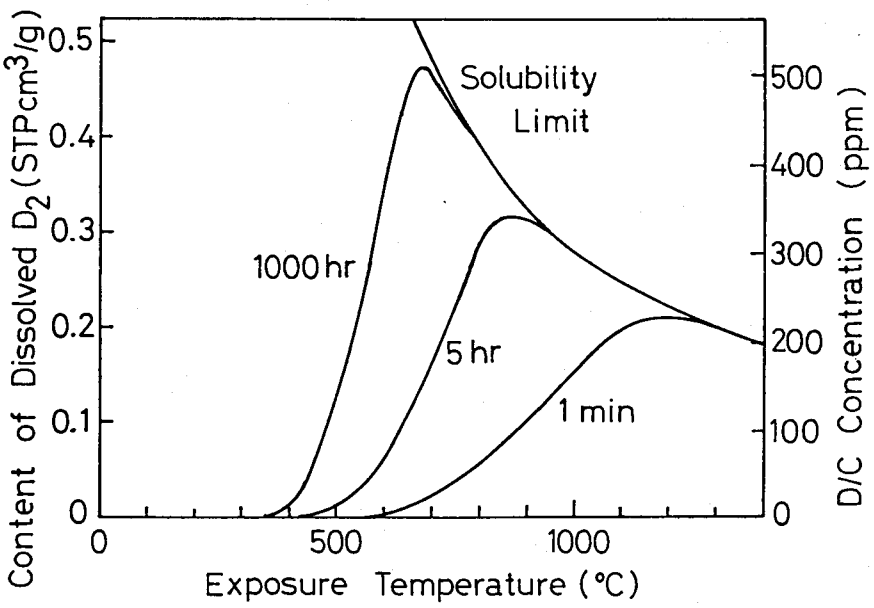

Fig. 7-18 Predicted deuterium retention curves for graphite exposed at various temperatures under D_2 gas pressure of 60 kPa.

4. Concluding remarks

The absorption and desorption of deuterium on graphite were studied on

isotropic graphite exposed to a deuterium gas atmosphere at elevated temperatures. Thermal desorption measurements were performed mainly at a constant heating rate of 10 ℃/min in a vacuum. The results obtained in the present study are summarized as follows:

(1) The solubility of deuterium appears to be proportional to the square root of D_2 gas pressure, and the influence of temperature on the solubility can be expressed by:

$$S\ (STPcm^3/g) = 1.9 \times 10^{-4}\ P^{1/2}\ (Pa)\ \exp(\ 4.5\ (kcal/mol)/RT\ ).$$

(850-1050 ℃, 2.5-13 kPa)

(2) The CD_4 desorption from graphite is relatively small.

(3) Deuterium desorption curves on graphite exposed to D_2 gas above 700 ℃ appear to have three peaks at approximately 140 ℃ (peak Ⅰ), 480 ℃ (peak Ⅱ) and 930 ℃ (peak Ⅲ).

(4) Deuterium in the graphite for peak Ⅱ may exists in the form of deuterium molecule, and as for peak Ⅲ, it may exist as deuterium atoms.

(5) Peaks Ⅱ and Ⅲ may attributed to pore and bulk diffusion, respectively. These diffusion coefficients can be expressed by the equations :

$$D_{Ⅱ}\ (cm^2/sec) = 1800 \exp[\ -29\ (kcal/mol)/RT\ ] \qquad (\ 300\text{-}500\ ℃\ ),$$

$$D_{Ⅲ}\ (cm^2/sec) = 1.69 \exp[\ -60\ (kcal/mol)/RT\ ] \qquad (\ 500\text{-}900\ ℃\ ).$$

(6) The deuterium uptaking behavior can be also explained by the diffusion model. A shorter exposure time causes the maximum temperature of deuterium retention to shift toward higher temperature.

References

[1] K.L.Wilson and W.L.Hsu, J.Nucl.Mater. 145-147 (1987) 121.

[2] R.A.Causey and K.L.Wilson, J.Nucl.Mater. 138 (1986) 57.

[3] R.A.Causey, M.I.Baskes and K.L.Wilson, J.Vac.Sci.Technol.A 4 (1986)

1189.

[4] R.A.Causey and K.L.Wilson, in: "Workshop on Tritium Technology", Tokyo, 1986.

[5] V.Philipps, E.Vietzke, M.Erdweg and K.Flaskamp, J.Nucl.Mater. 145-147 (1987) 292.

[6] K.Nakayama, S.Fukuda, T.Hino and T.Yamashina, J.Nucl.Mater. 145-147 (1987) 301.

[7] K.Ashida, K.Ichimura, M.Matsuyama and K.Watanabe, J.Nucl.Mater. 148 (1987) 217.

[8] H.D.Röhrig, P.G.Fischer and R.Hecker, J.Am.Ceram.Soc. 59 (1976) 316.

[9] R.A.Causey, T.S.Elleman and K.Verghese, Carbon 17 (1979) 323.

[10] S.E.Donnelly and D.G.Armour, Vacuum 27 (1976) 21.

[11] S.E.Donnelly and D.C.Ingram, Vacuum 28 (1977) 69.

[12] J.Crank, "The Mathematics of Diffusion, 2nd Edition" (Oxford University Press, Oxford, 1975) p.48, 91.

[13] M.Saeki, J.Nucl.Mater. 131 (1985) 32.

[14] M.Saeki, Int.J.Appl.Radiat.Isot. 34 (1983) 739.

[15] V.Malka, H.D.Röhrig and R.Hecker, in: "Proc. Tritium Technol. in Fusion, Fission and Isotopic Appl., A.N.S. National Topical Meetings", Ohio, 1980, p.102.

[16] Y.Iijima and K.Hirano, Bull.Jpn.Inst.Metals 14 (1975) 599 (in Japanese).

Ⅷ Conclusions

Problems still remain to apply the graphite to the first walls in a fusion device , though the graphite is the suitable candidate to the first walls and is frequently employed in fusion experimental reactors. In this thesis, (1) surface erosion of graphite by ion irradiation, (2) thermal desorption of D_2 and He from ion irradiated graphite and (3) Absorption and desorption of D_2 on graphite were discussed in Chapters Ⅲ -Ⅶ. The results are listed as follows:

(1) Surface erosion of graphite by ion irradiation (Chapters Ⅲ and Ⅳ)

Surface deformation of graphite by D_2^+ ion irradiation was quite different among the four samples studied in the present work, and it might be attributed to the structure of the sample. The changes in surface might be explained by an initial volume change due to stress accumulation (below 5×10^{18} ions/cm^2) and subsequent uniform sputtering erosion (above 1×10^{19} ions/cm^2). The difference of surface topography for isotropic graphite samples after D_2^+ ion irradiation may be attributed to the orientation of filler grains. The significant surface deformation was observed on the grain surfaces with prism plane orientation, while the surface with basal plane orientation showed little changes in surface features. Glassy carbon with microscopical isotropy did not suffer the significant surface deformation.

The distinctive features of the surface after He^+ ion irradiation were domed and/or conical upliftings with the step expansion in the irradiated area. These upliftings might be assisted by the bubble growth of helium gas during irradiation. PAPYEX was subjected to the heavy damage with many exfoliations due to the release of helium gas bubbles accumulated between

the lamella. On the other hand, glassy carbon showed little change in surface features without surface upliftings.

(2) Thermal desorption of D_2 and He from ion irradiated graphite (Chapters Ⅴ and Ⅵ)

Thermal desorption behavior of deuterium from graphite was complicated with multiple desorption peaks and the CD_4 desorption since there would exist strong chemical interactions between deuterium ions and carbon atoms. Deuterium desorption could be explained by the recombination-controlled desorption and diffusional release for each peak in thermal desorption curves. And the deutero-methane desorption were attributable to detrapping-controlled desorption.

Thermal desorption of helium took place at lower temperatures (100 - 500 ℃) as compared with deuterium desorption. The release mechanism of helium from graphite may be attributed to the diffusion-controlled process for lower irradiation doses (below 5×10^{16} ions/cm^2). And at higher irradiation doses (above 5×10^{17} ions/cm^2), it may be controlled by the detrapping process due to the development of dislocation loops with increasing irradiation dose.

(3) Absorption and desorption of D_2 on graphite (Chapter Ⅶ)

The dissolution process of deuterium into graphite was found to be exothermic process with an activation energy of 4.5 kcal/mol. Deuterium dissolved in graphite was considered to exist almost as deuterium atoms. Thermal desorption behavior from graphite exposed to deuterium gas atmosphere could be expressed by both pore (～480 ℃) and bulk (～930 ℃) diffusion.

The hydrogen and helium recycling behavior will be estimative under a

real fusion reactor environment and various conditions based on the data obtained in this work. However, it may be necessary to determine the influence of the characters of graphite samples (e.g. degree of graphitization), since that should be effective to the recycling behavior.

(4) Fusion application of graphite

There are many criteria for the ideal material for first walls in a fusion reactor as mentioned in Chapter I (Table 1-1). Graphite is considered as the eminent candidate for the first walls (plasma facing material) at the present state because of excellent heat resistivity and mechanical strength at high temperatures, though the metal components may be suitable for the first walls under a different design of a fusion reactor. The problems to apply the graphite for a fusion reactor material are gradually relieved and solved in recent years. However, various graphites have different properties such as outgassing rate, hydrogen solubility, hydrogen diffusivity and erosion durability. To take an instance, erosion durability of graphite samples obtained in the present work is given in Table 8-1. As shown in the table, erosion durability is quite varied with each sample. Glassy carbon (GC-30) appears to have good erosion durability among these samples, however this seems to be inferior to other graphites on thermal shock resistivity and processibility. High thermal shock resistivity is also one of the important criteria for first walls in a fusion reactor, though it was not discussed in this thesis. Therefore, comprehensive studies must be important to

Table 8-1 Erosion durability obtained in the present work.

	isotropic			
	ISOGRAPH-88	POCO DFP-3-2	PAPYEX	GC-30
D_2^+	△	△	△	○
He^+	△	△	×	○

(○ : good, △ : medium, × : bad)

choose the most suitable graphite materials.

Since there are various types of graphite with different properties, this suggests that it will be possible to newly develop the graphite with highly excellent properties based on the data of fundamental characters (mechanical strength, outgassing rate, chemical sputtering, hydrogen solubility, etc.). For instance, graphite surfaces with basal plane orientation or microscopical isotropy, showed high resistance to the irradiation damage by D_2^+ and He^+ ions, and therefore it may be useful for the design of the ideal graphite material.

To apply the composite material is also an approach to develop the excellent material. As one of the recent composite materials, C-C composites have significant mechanical strength and thermal shock resistivity, so that these materials are receiving much attention. It is necessary to have extensive studies on the various properties of graphite materials and new products from this time on.

Appendix ; Mechanisms and the estimation of thermal desorption of deuterium and helium from graphite

It has two purposes to analyze the thermal desorption behavior of gas atoms from a material, that is,

1) to know the release mechanisms of gas atoms from the material,

2) to predict the releasing behavior under various conditions.

The migration and desorption of gas atoms (e.g. hydrogen and helium) have been widely studied theoretically by numerous authors [1-20]. Especially in four papers [13,18-20], hydrogen recycling on first walls in a fusion reactor was discussed. The methods to evaluate the kinetic parameters of desorption process, which were applied in Chapters V, VI and VII, are described in the following.

The scheme of the simplified release processes of gas atoms is shown in Fig.9-1. The principal processes of releasing behavior are (a) detrapping (or dissociation), (b) diffusion and (c) recombination at surfaces, and the desorption of gas atoms is controlled by these processes individually or cooperatively. Desorption mechanisms will be complicated if the following

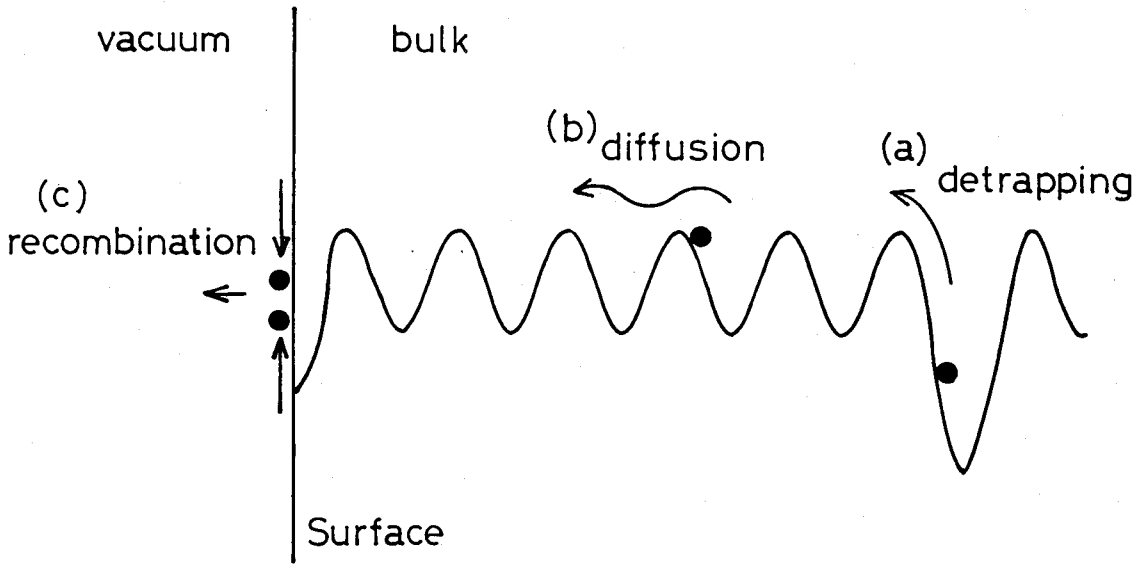

Fig. 9-1 Simplified mechanisms of gas releasing behavior.

conditions are there in the substance.

To be accompanied with ;

1) many kinds of trapping site with different binding energies,

2) many paths of diffusion (e.g. bulk diffusion and short circuit diffusion),

3) influence of retrapping.

The mechanisms will be slightly simpler in the case of helium desorption, since the recombination process can be excluded to consider the release mechanisms.

In this appendant chapter, processes (a), (b) and (c) have been considered in detail. Processes (a) and (c) can be expressed by Polanyi-Wigner equation, and process (b) can be expressed by Fick's 2nd law. They become,

detrapping :

$$-\frac{dn(t)}{dt} = \nu_1 \, n(t) \, \exp\left(-\frac{E}{RT}\right) , \qquad \text{----- (1)}$$

recombination :

$$-\frac{dn(t)}{dt} = \nu_2 \, \{ n(t) \}^2 \, \exp\left(-\frac{E}{RT}\right) , \qquad \text{----- (2)}$$

diffusion :

$$\frac{\partial C}{\partial t} = \mathrm{div} \, (D \, \mathrm{grad} C) , \qquad \text{----- (3)}$$

where n(t) (atoms) is the number of gas atoms within the sample, T (K) is the absolute temperature of the sample, ν (sec^{-1}) is the preexponential factor for desorption at zero coverage, E (kcal/mol) is the activation energy for each process, D (cm^2/sec) is the diffusion coefficient, R (kcal/mol · K) is the gas constant and C ($atoms/cm^3$) is the concentration of gas atoms within the sample. Thermal desorption behaviors can be analyzed by using these equations.

Falconer et al.[17] have proposed the eight analysis techniques to determine kinetic parameters of thermal desorption. These techniques can be divided into two groups which are heating rate variation methods and peak shape analysis methods on the temperature-programmed desorption curves. Heating patterns for the temperature-programmed desorption tests are usually adopted as 1) linear ramp heating ($T = T_0+\beta t$), 2) hyperbolic heating ($1/T = 1/T_0-\alpha t$) [21] and 3) step heating ($T = T_1$ $(t>0)$). Falconer et al.[17] was applied pattern 1) to analyze the temperature-programmed desorption. In the following sections, three methods for desorption analysis have been described.

1. Curve fitting method

This method is regression analysis to determine kinetic parameters that yield computer-generated curves which most closely approximate experimental curves obtained by linear ramp heating. This technique is essentially a trial-and-error method since the two distinct parameters (ν and E for detrapping, νn_0 and E for recombination, D_0 and E for diffusion) must be determined from one experimental curve. Hence, the accuracy of kinetic parameters determined by curve fitting may be low if the experimental desorption curve does not have high precision. It will be better to confirm the kinetic parameters, which were obtained by heating rate variation or step heating, with this curve fitting method rather than to directly determine the kinetic parameters.

(1) detrapping

Substituting the heating pattern, $T = T_0+\beta t$, eq.(1) becomes

$$-\frac{dn}{dt} = n_0 \exp\left(-\frac{E}{RT}\right) \exp\left\{-\frac{\nu}{\beta}\int_{T_0}^{T} \exp\left(-\frac{E}{RT}\right) dT\right\}, \quad \text{----- (4)}$$

where β (℃/sec) is the heating rate and T_0 is the starting temperature of a thermal desorption test. The thermal desorption curve derived from eq.(4) is shown in Fig.9-2(a) as a typical pattern of detrapping-controlled desorption. The detrapping-controlled desorption curve has a steeper slope for the higher temperature side of the curve and shows the narrowest peak among those for other desorption curves with the same activation energy.

(2) recombination

Desorption rate of recombination-controlled process can be derived from eq.(2) by substituting the equation, $T = T_0 + \beta t$, and it becomes

$$-\frac{dn}{dt} = n_0 \frac{\nu n_0 \exp\left(-\frac{E}{RT}\right)}{\left\{\frac{\nu n_0}{\beta}\int_{T_0}^{T} \exp\left(-\frac{E}{RT}\right) dT + 1\right\}^2} \qquad \text{----- (5)}$$

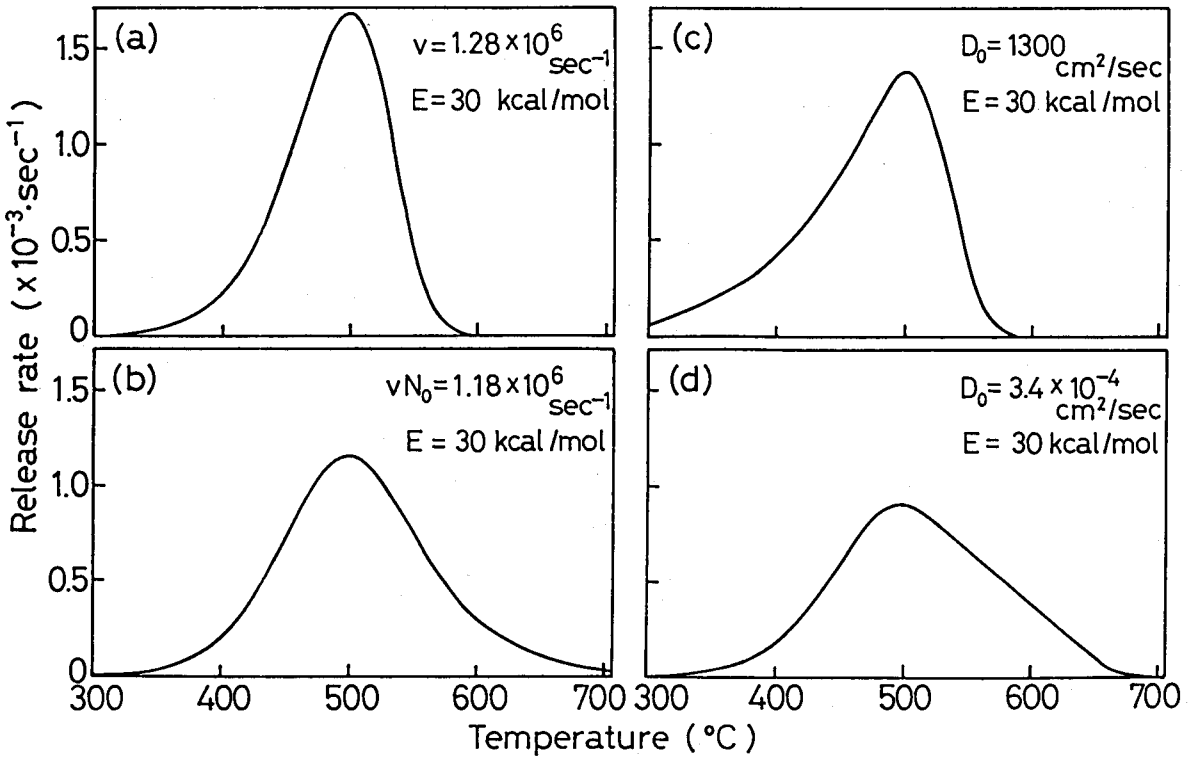

Fig. 9-2 Typical thermal desorption curves controlled by various mechanisms (Heating rate : 10 ℃/min).

(a) detrapping
(b) recombination
(c) diffusion (initial distribution of gas atoms is uniform, a = 1 mm)
(d) diffusion (with initial distribution of gas atoms given in Fig.6-9)

Since the parameters of the recombination-controlled desorption are νn_0 and E, the initial concentration, n_0, can be recognized to be effective in the desorption behavior. Figure 9-2(b) shows the typical pattern of the desorption curve controlled by recombination process. The desorption curve is almost symmetric (slightly broader for the higher temperature side in the strict sense) and relatively broad shape as compared with other desorption curves with the same activation energy.

(3) diffusion

Diffusion-controlled desorption depends on the sample dimension in contrast with the detrapping process and the recombination process. It is necessary to estimate the dimensions of the sample when the release mechanisms are analyzed. Firstly, diffusion in a plane sheet and a sphere is discussed where the initial distribution of gas atoms is uniform. Fick's 2nd law can be solved under following boundary conditions,

for a plane sheet :

$$\begin{cases} C = C_0 & -a/2 \leq x \leq a/2 \ , \quad t = 0 \\ C = 0 & x = \pm\ a/2 \ , \quad t > 0 \ , \end{cases}$$

for a sphere :

$$\begin{cases} C = C_0 & r \leq r_1 \ , \quad t = 0 \\ C = 0 & r = r_1 \ , \quad t > 0 \ , \end{cases}$$

where a (cm) is the thickness of the sample and r_1 (cm) is the radius of the sample. And it becomes

for a plane sheet :

$$N(t) = \frac{8}{\pi^2} \sum_{n=0}^{\infty} \frac{1}{(2n+1)^2} \exp\left(- \frac{(2n+1)^2 \pi^2}{a^2} Dt \right) , \qquad \text{----- (6)}$$

for a sphere :

$$N(t) = \frac{6}{\pi^2} \sum_{n=1}^{\infty} \frac{1}{n^2} \exp\left(- \frac{n^2 \cdot \pi^2}{r_1^{\,2}} Dt \right) , \qquad \text{----- (7)}$$

where N(t) is the fractional mean concentration of gas atoms within the sample (i.e. $N(t) = \int C(\vec{r},t)\, d\vec{r}/C_0V$, V: sample volume) [21]. Release rate ($-dN(t)/dt$) from a substance can be calculated from the change in concentration within unit time. However, when the diffusion coefficients are variable with time, the change in concentration can not be evaluated by solving the eq.(6) or (7). Thereupon, assuming that the linear ramp heating can be approximated to be a stepwise heating pattern as shown in Fig.9-3, the change of release rate with time was calculated for a sphere system in accordance with the flow chart, which is newly devised in the present study,

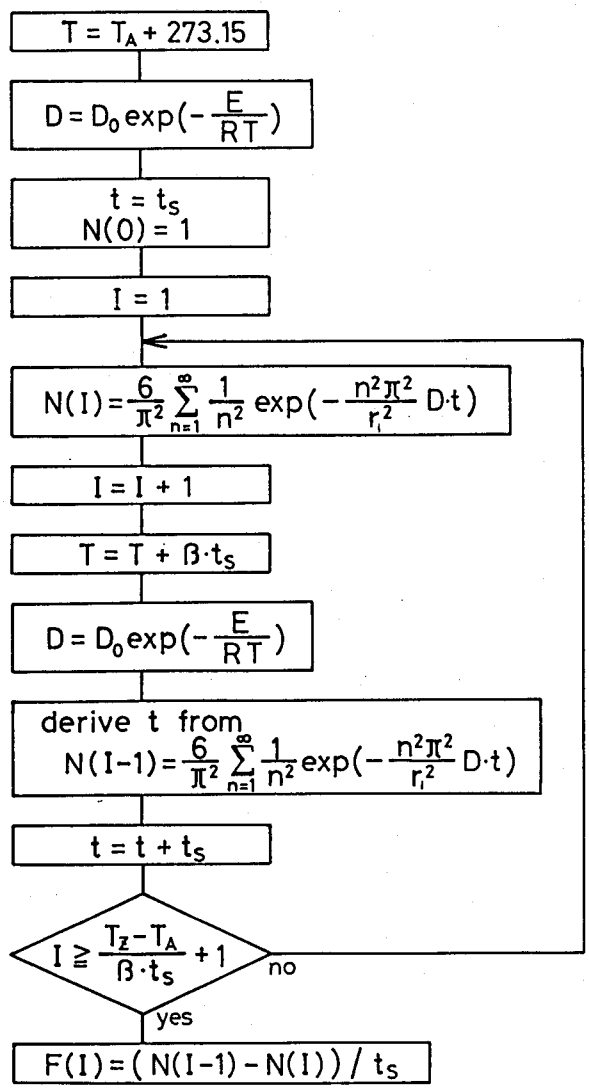

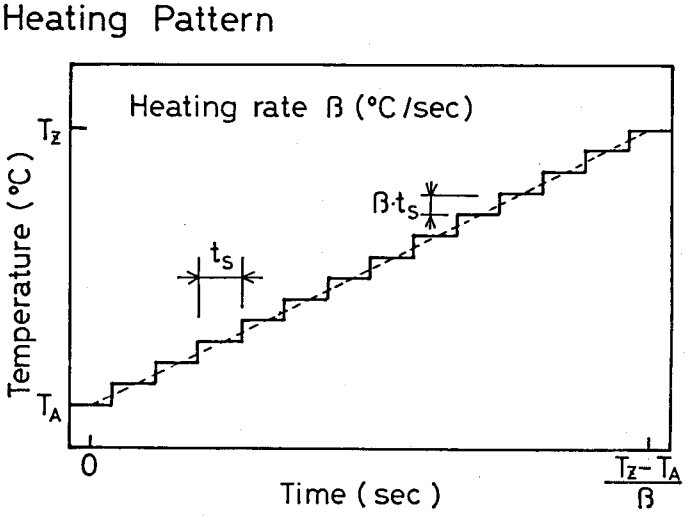

Nomenclatures

N(I) : fractional concentration within sample
D : diffusion coefficient (cm^2/sec)
D_0 : preexponential factor for diffusion (cm^2/sec)
E : activation energy for diffusion (cal/mol)
F(I) : fractional release rate (sec^{-1})
r_i : radius of filler grain (cm)
R : gas constant (cal/mol · K)
t : elapsed time (sec)
t_s : time interval for step heating (sec)
T : absolute temperature of sample (K)
T_A : starting temperature of desorption test (℃)
T_Z : ending temperature of desorption test (℃)
β : heating rate (℃/sec)

Fig. 9-3 Computational method for simulating the diffusional release during ramp heating (initial distribution is uniform.).

given in the figure. A result of this calculation is displayed in Fig.9-2(c) for a condition of a step height of 5 ℃ per 30 seconds. The desorption curve shows rather gentle slope for the lower temperature side and much steep slope for the higher side.

The initial concentration distribution will affect the thermal desorption behavior because of the dependency of the sample dimensions in contrast with the detrapping and recombination processes. In the case of the ion implantation, implanted atoms will distribute widely around the projected range as shown in Fig.6-9, release rate can not be derived analytically from the Fick's 2nd law. In such a case, release rate of gas atoms is usually evaluated from a series of difference equations based on the Fick's 1st law for each subdivided domain (Fig.9-4). The release rate from a sample can be expressed by the sum of the fluxes from the 1st domain and the Nth domain toward outside. A typical desorption curve is shown in Fig.9-2(d) for the sample with initial concentration distribution given in Fig.6-9. Thermal desorption rate for this diffusion process decreases straightly with increasing temperature for the higher temperature side of the desorption curve, and it shows much gentler slope as compared with the diffusion-controlled process with uniform concentration distribution. As mentioned above, release mechanisms can be roughly presumed from the thermal desorption curves obtained by linear ramp heating.

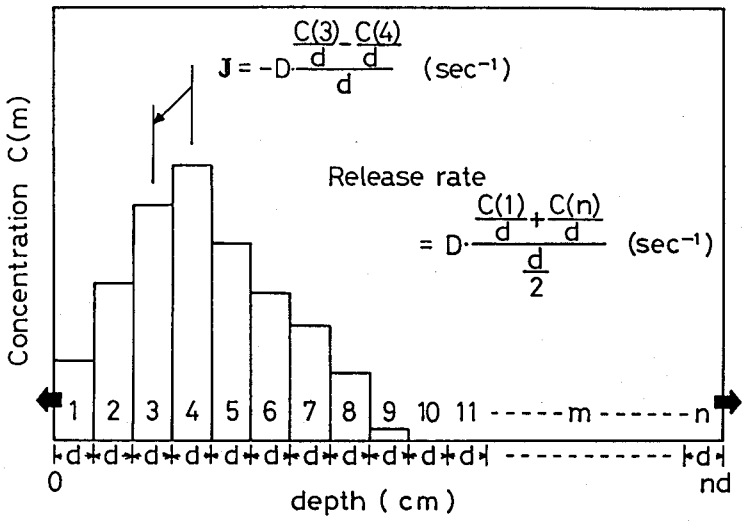

Fig. 9-4 Computational method for simulating the diffusional release with finite-difference equations.

2. Heating rate variation method

The heating rate variation technique utilizes the fact that with increased heating rate, peaks shift to higher temperatures and have larger amplitudes. These behaviors are special to the activation processes, while the peak temperature will not shift for the bursts of gas bubbles due to the increase of internal pressure which only depends on the temperature.

(1) detrapping

The temperature having maximum desorption rate (T_m) can be derived from the condition, $-d^2n/dt^2 = 0$, and the relation of T_m and kinetic parameters is solved to be

$$\frac{E}{RT_m^2} = \frac{\nu}{\beta} \exp\left(-\frac{E}{RT_m}\right) . \qquad \text{----- (8)}$$

It becomes

$$\ln\left(\frac{T_m^2}{\beta}\right) = \frac{E}{RT_m} + \ln\left(\frac{E}{R\nu}\right) . \qquad \text{----- (9)}$$

The points experimentally obtained as a plot of $\ln(T_m^2/\beta)$ versus $1/T_m$ for several desorption curves should represent the linear correlation [21]. Consequently, the activation energy, E, and the preexponential factor, ν, can be obtained from the slope and the intercept of the straight line, respectively.

(2) recombination

The relation of T_m and kinetic parameters can be expressed by

$$\frac{E}{RT_m^2} = \frac{n_0\nu}{\beta} \exp\left(-\frac{E}{RT_m}\right) . \qquad \text{----- (10)}$$

It becomes

$$\ln\left(\frac{T_m^2}{\beta}\right) = \frac{E}{RT_m} + \ln\left(\frac{E}{Rn_0\nu}\right) . \qquad \text{----- (11)}$$

In the same way, the activation energy, E, and the preexponential factor,

νn_0, can be obtained from the slope and the intercept of the straight line regressed on the plot of ln (T_m^2/β) versus $1/T_m$.

(3) diffusion

Since the peak shift for diffusion-controlled process will be difficult to be analyzed theoretically, it may be necessary to evaluate the peak shift by means of the curve fitting method for various activation energies, E, and preexponential factors, D_0.

The heating rate variation method has been described in this section. For every process, the degree of peak shift in heating rate variation tests is larger for smaller activation energies and is smaller for larger activation energies.

3. Step heating (isothermal desorption) method

Releasing behavior obtained in the step heating tests can be simply analyzed since the parameters which depend on temperature are constant during desorption. And the information to define the release mechanisms can be also received from the change of desorption rates for each temperature. However, it is preferable to use other methods together if the thermal desorption curve obtained in linear ramp heating consists of multiple peaks, because the step desorption curve (decay curve) is difficult to separate into the curves for elemental processes.

(1) detrapping

Step desorption rate for detrapping-controlled process can be easily obtained from eq.(1) at a constant temperature, it yields

$$-\frac{dn}{dt} = n_0 \nu \exp\left(-\frac{E}{RT}\right) \cdot \exp\left\{-\nu t \exp\left(-\frac{E}{RT}\right)\right\} \quad . \quad \text{----- (12)}$$

Equation (12) indicates that the step desorption rate is a simple exponential function of elapsed time, t. The step desorption curves for various temperatures are shown in Fig.9-5(a) at the same kinetic parameters as Fig.9-2(a). These desorption curves will be straight lines for a logarithmic vertical axis, and the parameters E and ν can be evaluated from the temperature dependency of the slopes or the intercepts of the lines.

(2) recombination

Equation (2) can be solved for a constant temperature, and it becomes

$$-\frac{dn}{dt} = n_0 \frac{\nu n_0 \exp\left(-\frac{E}{RT}\right)}{\left\{\nu n_0 t \exp\left(-\frac{E}{RT}\right) + 1\right\}^2} \quad . \quad \text{----- (13)}$$

Typical step desorption curves of recombination-controlled process are shown in Fig.9-5(b). This figure exhibits that the changes of desorption rates become straight lines for lower temperatures and become steep curves for higher temperature. The activation energy, E, and preexponential factor, νn_0, can be obtained from the temperature dependency of the initial desorption rates (t=0) of these curves.

(3) diffusion

Step desorption rate for diffusion-controlled process can be calculated from eq.(6) or (7) at a constant temperature, that is

for a plane sheet :

$$-\frac{dN(t)}{dt} = -n_0 \frac{8}{\pi^2} \cdot \frac{d}{dt} \sum_{n=0}^{\infty} \frac{1}{(2n+1)^2} \exp\left(-\frac{(2n+1)^2 \pi^2}{a^2} Dt\right) \quad \text{----- (14)}$$

for a sphere :

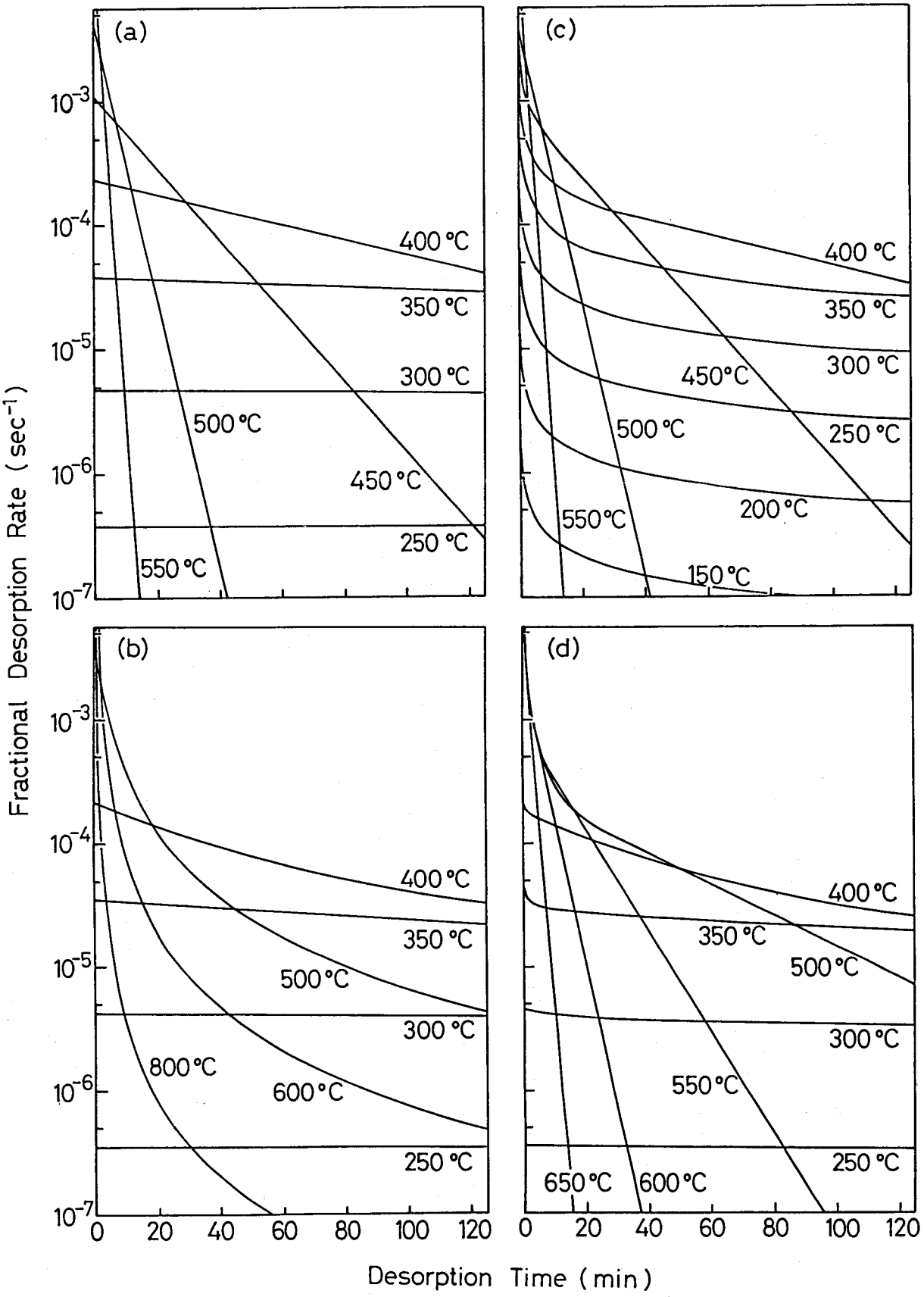

Fig. 9-5 Typical step desorption curves controlled by various mechanisms.
(a) detrapping (b) recombination
(c) diffusion (initial distribution of gas atoms is uniform, a = 1 mm)
(d) diffusion (with initial distribution of gas atoms given in Fig.6-9)

$$-\frac{dN(t)}{dt} = -n_0 \frac{6}{\pi^2} \frac{d}{dt} \sum_{n=1}^{\infty} \frac{1}{n^2} \exp\left(-\frac{n^2\pi^2}{r_1^2} Dt\right) \quad . \quad \text{----- (15)}$$

Based on the eq.(14), step desorption curves were calculated for the substance with a thickness of 1 mm and displayed in Fig.9-5(c). Since the eq.(14) can be approximated to the equation, $-dN(t)/dt=a\sqrt{D\cdot t}$, for lower temperatures, these desorption curves are parallel with one another and the release rates will increase one order of magnitude for every two orders' increase of a diffusion coefficient. For higher temperatures, eqs.(14) and (15) can be approximated to the first member of the equations because of the large diffusion coefficient. Namely, step desorption rates for diffusion-controlled process will obey a exponential function at higher temperatures. Diffusion coefficients can be directly determined from the slope of exponential desorption curve or the changes of curve shapes at transition temperatures from a parabolic function to an exponential function. If the initial concentration, N_0, is already known, diffusion coefficients can be also evaluated from the amplitude of desorption rate for lower temperatures. The activation energy for diffusion, E, will be obtained with Arrhenius plots of diffusion coefficients determined by curve fitting.

Figure 9-5(d) shows typical step desorption curves from a material with initial concentration distribution given in Fig.6-9. These curves resemble to the recombination-controlled desorption for lower temperatures (250, 300 and 350 ℃) and are similar to the diffusion-controlled desorption with uniform concentration distribution (Fig.9-5(c)) for higher temperatures.

References

[1] P.A.Redhead, Vacuum 12 (1962) 203.

[2] G.Carter, Vacuum 12 (1962) 245.

[3] R.Kelly, Acta Metallurgica 12 (1964) 123.

[4] R.Kelly, Nucl.Instrum.Meth. 38 (1965) 181.

[5] R.Kelly and H.Matzke, J.Nucl.Mater. 20 (1966) 171.

[6] R.Kelly, Phys.Stat.Sol. 21 (1967) 451.

[7] G.Farrell and G.Carter, Vacuum 17 (1967) 15.

[8] R.Kelly and Č.Jech, J.Nucl.Mater. 30 (1969) 122.

[9] B.K.Reiermann, M.G.Frohberg and H.G.Feller, "Ergebnisse der Hochvakuumtechnik und Physik dünner Schichten Band Ⅱ" (M.Auwärter ed., Wissenschaftliche Verlagsgesellschaft MbH, Stuttgart, W.Germany, 1971) p.423 (in German).

[10] S.E.Donnelly and D.G.Armour, Vacuum 27 (1977) 21.

[11] S.E.Donnelly and D.C.Ingram, Vacuum 28 (1978) 69.

[12] S.E.Donnelly, D.C.Ingram, R.P.Webb and D.G.Armour, Vacuum 29 (1979) 303.

[13] J.L.Cecchi, J.Vac.Sci.Technol. 16 (1979) 58.

[14] L.M.Caspers and A.van Veen, Phys.Stat.Sol.(a) 68 (1981) 339.

[15] A.A.van Gorkum and E.V.Kornelsen, Vacuum 31 (1981) 89.

[16] A.D.LeClair, Diffusion and Defect Data 33 (1983) 1.

[17] J.L.Falconer and J.A.Schwarz, Catal.Rev.-Sci.Eng. 25 (1983) 141.

[18] S.Yamaguchi, Oyo Buturi 52 (1983) 220 (in Japanese).

[19] B.L.Doyle and D.K.Brice, Radiation Effects 89 (1985) 21.

[20] T.Tanabe, Sinkuu 29 (1986) 353 (in Japanese).

[21] I.Yasumori, "Kaimen To Colloid" (Chemical Society of Japan ed., Maruzen, Tokyo, 1977) p.119 (in Japanese).

[22] J.Crank, "Mathematics of Diffusion, 2nd Ed." (Oxford University Press, Oxford, 1975) p.48, 91.

Acknowledgements

The author wishes to express the sincere and heart-felt appreciation to Professor Dr.M.Miyake of Osaka University for precious guidance, adequate discussions and sincere encouragement.

The author is much indebted to Prof.T.Sekiya, Prof.K.Sumita, Prof.T.Okada, and Prof.T.Yamamoto for their valuable discussions and suggestions.

The author is also indebted to Dr.M.Katsura, Dr.P.Son and Mr.S.Yamanaka for their valuable guidance and advice.

The author would like to thank Dr.M.Nunogaki for his kind offices in operating the ion accelerator and fruitful discussions. Thanks are due to Mr.S.Tokura, Mr.T.Yamauchi, Mr.M.Shinno, Mr.Y.Fujisawa, Mr.A.Yoshida, Mr.H.Suezawa and the members of Miyake laboratory for their help with the experiments.

The author wishes to thank Prof.Y.Tsuji, Prof.Y.Honda, Prof.B.Kyou, Prof.K.Katsurayama, Prof.C.Yamanaka and all the staffs of Nuclear Reactor Engineering Department of Kinki University for their warm encouragement.

List of Papers by the Author

(1) H.Atsumi, S.Yamanaka, P.Son and M.Miyake,
" Thermal Desorption of Deuterium and Helium from Ion Irradiated Graphite."
Journal of Nuclear Materials 133/134 (1985) 268-271.

(2) H.Atsumi, S.Tokura, S.Yamanaka, M.Nunogaki and M.Miyake,
" Surface Erosion of Isotropic Graphite by the 20 keV Deuterium Ion Irradiation."
Technology Reports of the Osaka University 36 (1986) 41-46.

(3) H.Atsumi, S.Tokura, S.Yamanaka, M.Nunogaki and M.Miyake,
" Surface Erosion of Graphite by D^+ Irradiation."
Journal of Nuclear Materials 141-143 (1986) 113-118.

(4) H.Atsumi, S.Tokura, T.Yamauchi, S.Yamanaka and M.Miyake,
" Thermal Desorption of Helium from Graphite Irradiated by He^+ Ions."
Journal of Nuclear Materials 141-143 (1986) 258-261.

(5) H.Atsumi, S.Tokura and M.Miyake,
" Thermal Desorption Measurement of Deuterium from Graphite Exposed to D_2 Gas Atmosphere at Elevated Temperatures."
Technology Reports of the Osaka University 37 (1987) 255-261.

(6) H.Atsumi, S.Tokura and M.Miyake,
" Absorption and Desorption of Deuterium on Graphite at Elevated Temperatures."
Journal of Nuclear Materials 155-157 (1988) 241-245.

(7) S.Tokura, H.Atsumi, T.Yamauchi, M.Shinno, S.Yamanaka and M.Miyake,
" Thermal Desorption Behavior of He Implanted into Graphite."
Journal of Nuclear Materials 155-157 (1988) 246-250.

List of Lectures by the Author

A. International Conference

(1) " Thermal Desorption of Deuterium and Helium from Ion Irradiated Graphite." 1st International Conference on Fusion Reactor Materials (ICFRM-1), Tokyo, Japan, December 1984.

(2) " Thermal Desorption of Helium from Graphite Irradiated by He^+ Ions." 2nd International Conference on Fusion Reactor Materials (ICFRM-2), Chicago, U.S.A., April 1986.

(3) " Surface Erosion of Graphite by D^+ Irradiation." 2nd International Conference on Fusion Reactor Materials (ICFRM-2), Chicago, U.S.A., April 1986.

(4) " Absorption and Desorption of Deuterium on Graphite at Elevated Temperatures." 3rd International Conference on Fusion Reactor Materials (ICFRM-3), Karlsruhe, F.R.G., October 1987.

B. Domestic Meetings

(1) " Releasing Behavior of Hydrogen Isotope from Graphite." 1984 Annual Meeting of the Atomic Energy Society of Japan, Higashi-Osaka, March 1984.

(2) " Releasing Behavior of Hydrogen Isotope from Graphite (Ⅱ)." 1984 Fall Meeting of the Atomic Energy Society of Japan, Tokai-mura, October 1984.

(3) " Releasing Behavior of Hydrogen Isotope from Graphite (Ⅲ)." 1985 Annual Meeting of the Atomic Energy Society of Japan, Tokyo, March 1985.

(4) " Releasing Behavior of Hydrogen Isotope from Graphite (Ⅳ)." 1985 Fall Meeting of the Atomic Energy Society of Japan, Sendai, October 1985.

(5) " Graphite Surface Erosion by D^+ Ion Irradiation." 1986 Annual Meeting of the Atomic Energy Society of Japan, Uji, March 1986.

(6) " Graphite Surface Erosion by He^+ Ion Irradiation." 1986 Fall Meeting of the Atomic Energy Society of Japan, Fukuoka, October 1986.